DEFORMATIONAL PROCESSES AFFECTING UNLITHIFIED SEDIMENTS AT ACTIVE MARGINS: A FIELD STUDY AND A STRUCTURAL MODEL

by

Mark Thomas Brandon

A dissertation submitted in partial fulfillment
of the requirements for the degree of

Doctor of Philosophy

University of Washington

1984

Approved by Darrel S Cowan

Program Authorized
to Offer Degree Geological Sciences

Date June 20, 1984

In presenting this dissertation in partial fulfillment of the requirements for the Doctoral degree at the University of Washington, I agree that the Library shall make its copies freely available for inspection. I further agree that extensive copying of this dissertation is allowable only for scholarly purposes, consistent with "fair use" as prescribed in the U.S. Copyright Law. Requests for copying or reproduction of this dissertation may be reffered to University Microfilms, 300 North Zeeb Road, Ann Arbor, Michigan 48106, to whom the author has granted "the right to reproduce and sell (a) copies of the manuscript in microform and/or (b) printed copies of the manuscript made from microform."

Signature Mark T. Bearden

Date 20 June 1984

University of Washington

Abstract

Deformational processes affecting unlithified sediments at active margins: a field study and a structural model

By Mark Thomas Brandon

Chairperson of Supervisory Committee: Professor Darrel S. Cowan
Department of
Geological Sciences

Part I of this study focuses on the origin of chaotic melanges in the Pacific Rim Complex (PRC), which is exposed in a narrow fault-bounded slice along the west coast of Vancouver Island. The complex is composed of a chaotic sequence of Lower Cretaceous melanges, which depositionally overlie an older igneous basement. Previous interpretations have considered the Complex to be a late Mesozoic accretionary wedge constructed against the west-side of the Wrangellia terrane. A number of factors argue against this interpretation: (1) the PRC melanges are depositionally underlain by an older arc-related basement, and not by oceanic crust, (2) exotic blocks are submarine slide blocks, mostly derived from the underlying basement, and (3) the melanges show no evidence of major thrust imbrication, which is a common feature of well documented ancient accretionary complexes. The heterogeneous structural style of melanges is more compatible with an origin by down-slope mass-movement processes, such as submarine slides, rock falls, debris flow and in-situ liquefaction. Indirect evidence suggests that extensive mass-movement was due to frequent large earthquakes and strong ground motion at a seismically active plate boundary.

Part II of this study utilizes the concepts of critical state soil mechanics in an analysis of the deformational behavior of unlithified sediments at a subduction-zone setting. The goal of this analysis is to identify those factors affecting the development of specific structural styles. The initial consolidation state of the deforming sediment has the most influence on the development of specific structural styles: highly overconsolidated sediments tend to develop widely spaced, discrete faults, whereas normally consolidated sediments probably develop thick shear zones characterized by scaly fabrics. Furthermore, it is concluded that the general structural style is not significantly affected by the presence of large load-induced excess pore pressures, or by the expected variations in subduction-zone loading conditions. While this analysis does not clearly indicate what causes discrete faults to form within subduction-zone sediments, two geologic process appear to promote their occurrence: (1) the internal generation of excess fluid pressure due to devolatization reactions, and (2) lithification and cementation.

TABLE OF CONTENTS

LIST OF FIGURES

LIST OF TABLES

ACKNOWLEDGMENTS

With the completion of this project there are many people to thank. First and foremost, I thank Darrel Cowan, my adviser, who has provided inspiration and assistance through my graduate years at UW. My sincere appreciation goes to the other members of my committee--Jody Bourgeois, Bill Bruner, Peter Misch and Joe Vance; their comments and criticisms have substantially improved this dissertation. I am grateful for the comraderie provided by my fellow graduate students. In particular, I would like to thank Margi Rusmore who worked to the south of my area; the results of her work have helped to place the Pacific Rim Complex into a more regional context. Furthermore, I am deeply indebted to Susan Monsen who, through thick and thin, has provided me with moral, financial, geological and clerical support.

Jan Muller of the Geological Survey of Canada graciously related his knowledge of Pacific Rim geology and also provided maps and some thin sections. Paul Brandon, Bev Brashen, Jill Karsten, Carol Levine, Amy Ng, and Kathyrn Willis all provided able assistance in the field. Shell Canada freely provided aeromagnetic maps and drilling samples from the offshore area to the west of the Pacific Rim. Colin Cool and Tracy Tingle supplied whole rock geochemical analyses. John Hedges provided the analyses for organic carbon. Emile Pessagno, Jr. and Erle Kauffman kindly identified fossils for me. I gratefully acknowledge funding support from Sigma Xi, the Geological Society of America, the Department of Geological Sciences Corporation Fund and the National Science Foundation (grant to Cowan).

PART I

THE ORIGIN OF THE PACIFIC RIM COMPLEX, A MESOZOIC MELANGE ALONG THE WESTERN MARGIN OF VANCOUVER ISLAND

INTRODUCTION FOR PART I

The Pacific Rim Complex is exposed in a narrow, fault-bounded slice along the west coast of Vancouver Island (Figure 1). The unit consists of a chaotic assemblage of Lower Cretaceous mudstone, sandstone and chert, which overlies an older volcanic arc complex. This paper focuses on the depositional and early deformational history of the Pacific Rim Complex, with an emphasis on the processes responsible for melange formation. The Complex contains some of the best preserved and exposed Mesozoic melanges[1] in western North America. Pleistocene glaciation and frequent Pacific storms have resulted in extensive tracts of fresh coastal outcrop. Fabrics and structures in the melange are generally not affected by younger superimposed deformation, and therefore can be interpreted with more confidence than is possible in many other melange terranes. Furthermore, the Complex contains a variety of melanges that appear to reflect a spectrum of deformation processes.

The origin of the Pacific Rim melanges also has important tectonic implications. Previous workers (Page, 1974; Muller, 1973, 1977) have argued that the Complex represents a tectonic assemblage formed within a Late Mesozoic subduction complex. They have suggested, along with Dickinson (1976), that the Pacific Rim was coextensive with other coeval subduction complexes along the western margin of North America (e.g., Franciscan Complex of California, Chugach terrane of southern Alaska, etc.). Several large allochthonous terranes presently lie to the east of these subduction complexes. If this interpretation is correct, these terranes must have been sutured to North America prior to the proposed Late Jurassic inception

[1] In this paper, melange is used as a non-genetic term to describe chaotically disrupted sedimentary rocks, commonly containing exotic blocks in a finer grained matrix. See Silver and Beutner, 1980, for a more extended discussion.

Figure 1. Generalized geologic map of Vancouver Island and surrounding area, modified from Roddick, et al. (1979) to include more recent work on southern Vancouver Island (Muller, 1977b; Rusmore, 1982) and the San Juan Islands (Brandon, et al., 1983). Quaternary sediments are not shown.

Lower Eocene and younger rocks. North of the Leech River fault: Upper Eocene and younger sedimentary rocks of the Carmanah Group, equivalent to strata of the offshore Tofino Basin. South of the Leech River fault: Lower Eocene basalts and younger sedimentary rocks.

Nanaimo Group. Upper Cretaceous marine sedimentary rocks.

Leech River Complex. Jurassic-Cretaceous rocks that were regionally metamorphosed during the early Tertiary (Fairchild and Cowan, 1982).

Coast Plutonic Complex. Late Cretaceous and early Tertiary plutonic rocks; also includes minor pendants and screens of older rocks.

Pacific Rim Complex, together with other Jurassic-Lower Cretaceous units (on Vancouver Island: Pandora Peak unit and rocks of Gonzales Bay; and in the San Juan Islands: Constitution formation, Lopez Complex and Decatur terrane). Generally consists of volcaniclastic sandstone and mudstone with subordinant ribbon chert and basalt; locally includes older basement rocks.

Wrangellia terrane. Lower Cretaceous and older rocks that underlie most of Vancouver Island.

Paleozoic rocks of the San Juan Islands (see Brandon, et al., 1983).

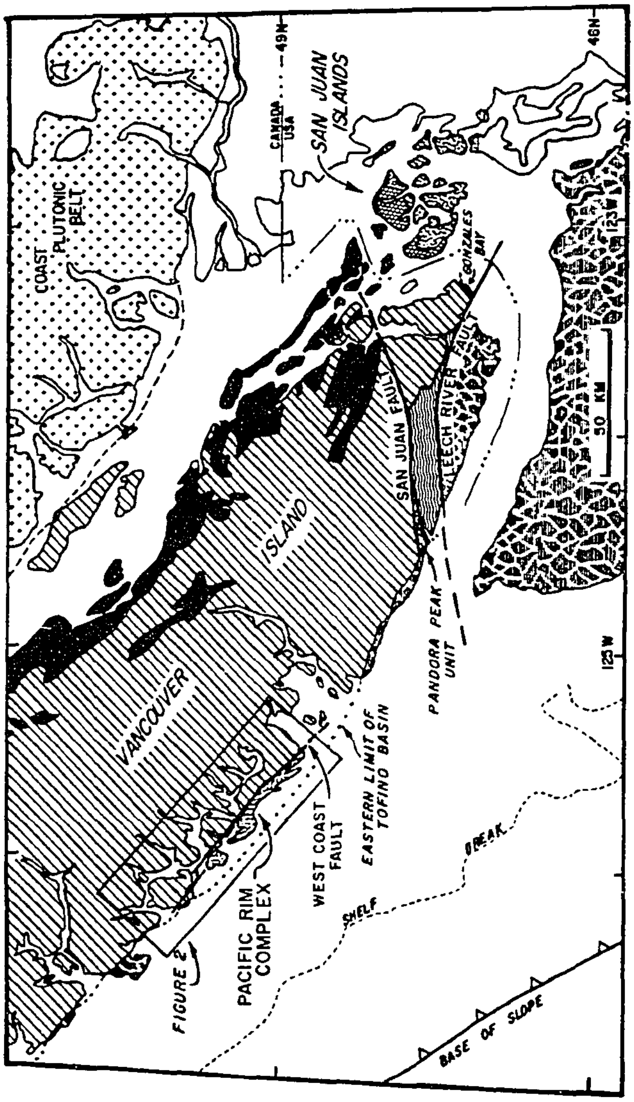
COAST PLUTONIC BELT
SAN JUAN ISLANDS
CANADA
USA
49N
GONZALES BAY
SAN JUAN FAULT
LEECH RIVER FAULT
50 KM
VANCOUVER
ISLAND
PANDORA PEAK UNIT
EASTERN LIMIT OF TOFINO BASIN
WEST COAST FAULT
PACIFIC RIM COMPLEX
FIGURE 2
SHELF
BREAK
BASE OF SLOPE

of subduction. Most notable of these older terranes is the Wrangellia terrane (Irving and Yole, 1972; Jones, et al., 1977), which underlies most of Vancouver Island (Figure 1).

There are several reasons to question this interpretation. The Pacific Rim Complex is presently only 5 - 10 km wide in map view and lies fairly close to the modern subduction zone, 100 km to the southwest (Figure 1). If the Pacific Rim Complex represents a major accretionary complex, either not much sediment was accreted, or large portions of this complex are missing. Elsewhere along the west coast of Vancouver Island, Pacific Rim rocks are generally absent, and instead older rocks of the Wrangellia terrane underlie the present continental margin. These relationships suggest that the tectonic history of the Vancouver Island margin is more complicated than previously appreciated.

A very different view of the tectonic evolution of this margin has emerged as the result of further field work in the Pacific Rim area and new fossil ages and radiometric dates. The Pacific Rim Complex represents a displaced fragment within a large transform fault system which truncated the west side of Vancouver Island during Late Cretaceous and early Tertiary time (Brandon and Cowan, 1983). This transform system has removed more westerly portions of the Wrangellia terrane and the Pacific Rim Complex, and has displaced them northward to southern Alaska (see Cowan, 1982). The Pacific Rim Complex has also been displaced with respect to Vancouver Island, but probably not more than 100 km. Similarities in stratigraphy and metamorphism indicate the Complex was probably originally coextensive with other Mesozoic rocks located around the southern end of Vancouver Island and in the San Juan Islands (Figure 1--Pandora Peak unit, rocks of Gonzales Bay and the Constitution formation).

Therefore, the Pacific Rim Complex represents only a small portion of a once more extensive Mesozoic active-margin complex. The original tectonic setting of the Pacific Rim Complex is uncertain, but geologic relationships indicate that it does not represent an ancient accretionary wedge, that is, an imbricated complex of sediments and oceanic volcanic rocks formed by offscraping and accretion at an active subduction zone (Karig, 1983). Three lines of evidence have prompted this conclusion: (1) the Lower Cretaceous melange units depositionally overlie a regionally extensive Upper Triassic -Jurassic volcanic arc complex and are not associated with normal oceanic crust; (2) chaotic disruption of the Lower Cretaceous melanges is not due to fault zone deformation but instead represents a variety of mass-movement processes, and (3) undisrupted portions of the melange matrix contain in-situ macrofossils indicating some of the sedimentary materials were originally deposited in relatively shallow depths and do not represent deeper water, trench-fill turbidites. These factors suggest that the melanges accumulated in a slope basin setting within a morphologically complex active margin. If this margin included a coeval accretionary wedge, it was probably located seaward of the Pacific Rim Complex, and has since been removed by younger transcurrent faulting.

STRATIGRAPHIC FRAMEWORK

The Pacific Rim Complex can be divided into six major rock units. Based on geologic relationships exposed on the Ucluth Peninsula at the south end of the area (Figures 2 and 3), four of these units can be confidently placed into a general stratigraphic sequence, summarized in Figure 4. Age data for these units are shown in Figure 5.

The presence of a stratigraphic sequence is perhaps unexpected within a chaotic melange terrane, and therefore represents an important conclusion of my fieldwork. Previous workers (Muller, 1973, 1977; Page, 1974) noted the prevalence of fault contacts within the Pacific Rim Complex and argued that these faults formed during subduction underthrusting. However, most of the faults are high-angle and appear to have only modest displacements. Furthermore, they commonly offset early Tertiary dikes and are more likely related to younger transcurrent faulting.

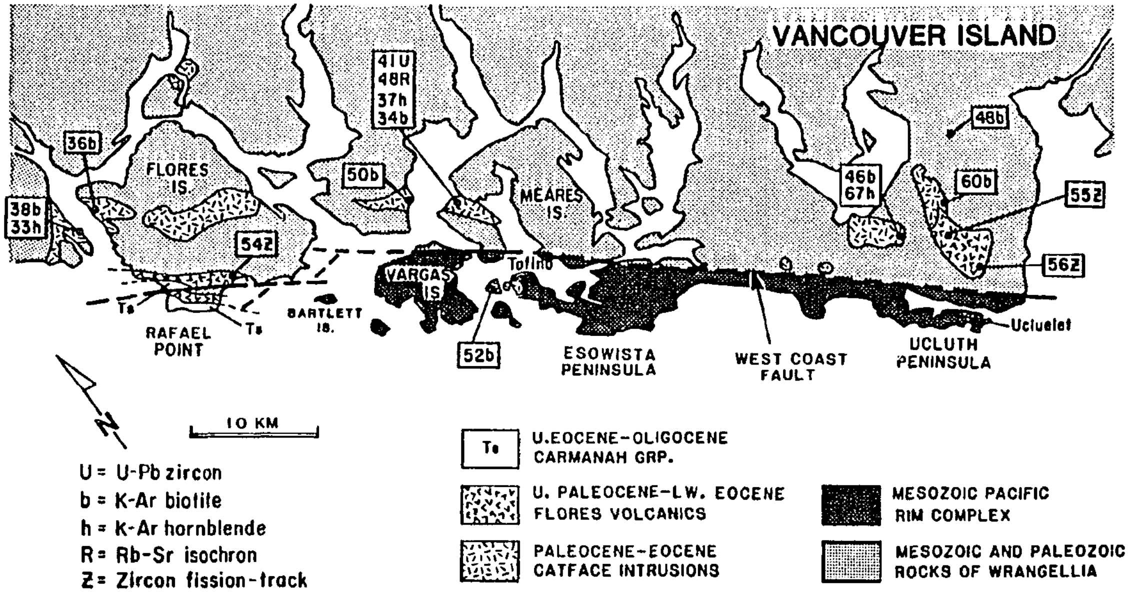

Figure 2. Geologic map of the Pacific Rim area, modified from Muller (1977b) to include my work. Radiometric dates are shown for early Tertiary volcanic and plutonic rocks. K-Ar dates are from Carson (1973), and Muller, et al. (1981) and have been recalculated using new decay constants (Harland, et al., 1982). Dates for the pluton on Meares Island are from C. Isachsen (1983). Zircon fission track ages for the Flores volcanics (informal name) were determined by J. A. Vance, University of Washington.

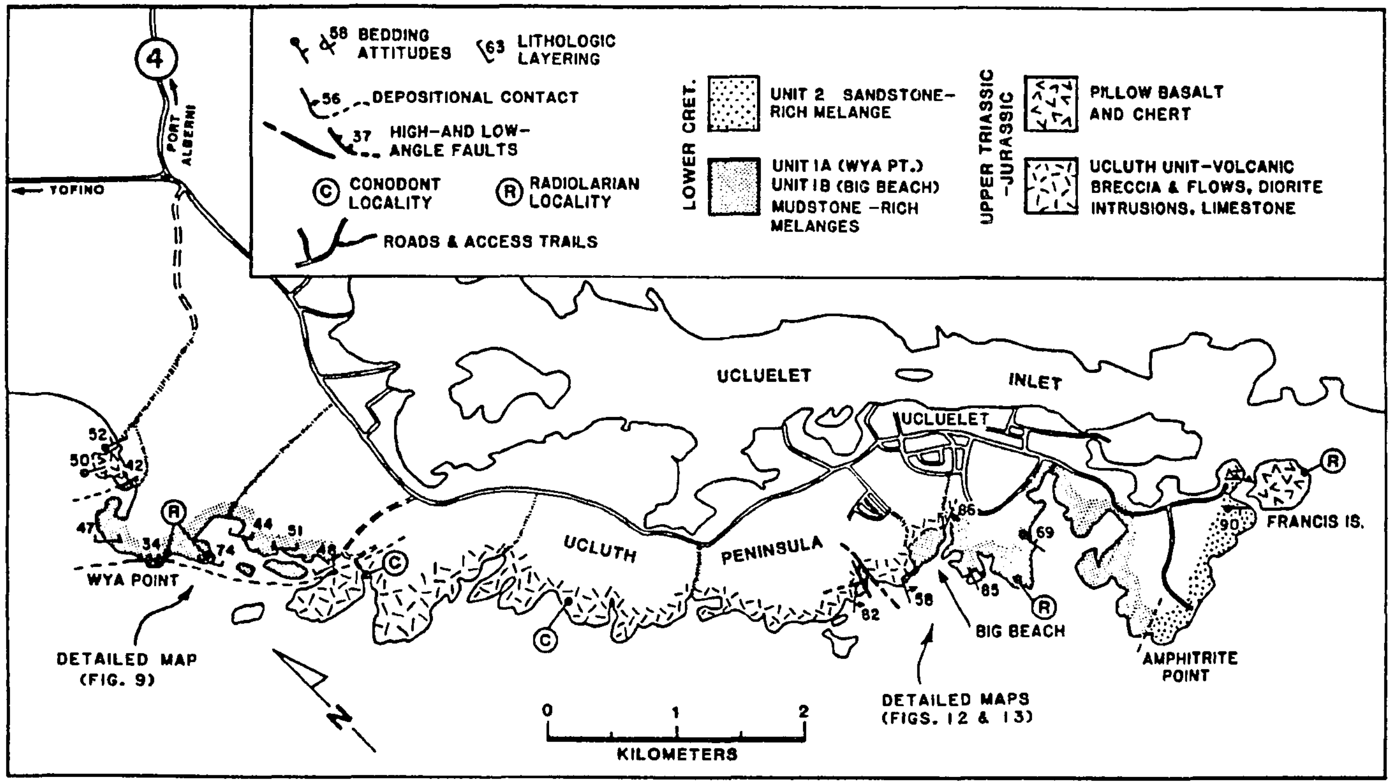

Figure 3. Geologic map of the Ucluth Peninsula showing the relationship between the Ucluth Volcanics and the overlying melange units.

	GENERALIZED STRATIGRAPHY OF PACIFIC RIM COMPLEX	
LOWER CRETACEOUS VAL.-LOWER HAUT. --- ? ---	**UNIT 2** Sandstone-rich turbidite unit (sand/mud > 9), commonly with thick to massive sandstone beds. Highly contorted and folded; primary sedimentary structures are variably obscured by liquefaction.	
	---------------------GRADATIONAL CONTACT---------------------	
	UNIT 1A Mudstone, radiolarian chert and lenses of featureless sandstone. Bedding is planar, but displays extensive layer-parallel disruption. The unit also contains large exotic blocks derived from the underlying Ucluth Volcanics. —LATERALLY RELATED—	**UNIT 1B** Laminated mudstone, pebbly mudstone, turbidite sandstone and channelized conglomerate; also rare interbedded sequences of radiolarian chert. Laminated mudstone contains *Buchia* coquina and large, in-situ fossil bivalves. Bedded lithologies are highly contorted and folded with minor layer-parallel extension.
	UNCONFORMITY	
UPPER TRIASSIC - ?JURASSIC	**UCLUTH VOLCANICS** Fragmental volcanic rocks, amygdaloidal flows, and interbedded Upper Triassic limestone. Intruded by Upper Triassic(?) diorite dikes and stocks. Might also contain minor pillow lava with interbedded chert of Early Jurassic age.	

Figure 4. Generalized stratigraphic framework of the Pacific Rim Complex.

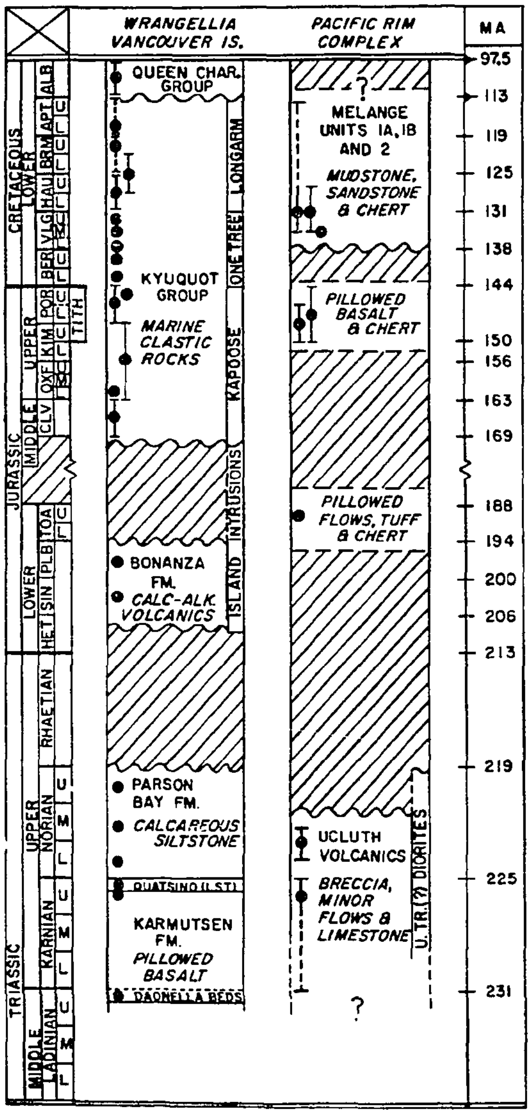

Figure 5. Stratigraphic comparison of the Pacific Rim Complex with Mesozoic units of the Wrangellia terrane, Vancouver Island. Fossil control for Wrangellia units summarized from Muller, et al. (1974, 1981) and other sources cited there. The radiometric time scale shown on the right is from Harland, et al. (1982).

Perhaps the most compelling evidence for a stratigraphic interpretation is the presence of a regionally extensive basement unit which underlies the Pacific Rim melanges. This previously unrecognized unit, which is herein named the Ucluth Volcanics, consists of calc-alkaline basalts with subordinate diorite intrusions and interbedded Upper Triassic limestone. The melange units overlie the Ucluth Volcanics, and consist of two basal mudstone-rich melanges, Units 1A and 1B, grading upward into a stratigraphically higher sandstone-rich melange, Unit 2. The basal melange units can locally be found in demonstrable depositional contact with the underlying volcanics. Elsewhere they contain large diorite blocks, clearly derived from the Ucluth Volcanics.

Two other rock units, both of which, consist of pillow lava and chert, have yielded Early and Late Jurassic ages (Figure 5). The Upper Jurassic unit occurs as exotic blocks within mudstone-rich melange. The Lower Jurassic unit might represent a younger portion of the Ucluth Volcanics. These two units constitute a small part of the Pacific Rim Complex, and thus their origin, and their relationship to the rest of the Complex is not well understood.

These six units are described below, with special emphasis on features that might help to define how and where the Lower Cretaceous melange units were formed.

TRIASSIC AND JURASSIC VOLCANIC UNITS

UCLUTH VOLCANICS

The Ucluth Volcanics represent a newly designated formation within the Pacific Rim Complex. This formation is named after the Ucluth Peninsula where it is well exposed in the core of an east-west trending anticline (Figure 3). Exposures on the west coast of the Peninsula are designated as the type area of the formation.

Lithology. The unit consists dominantly of green, aphanitic volcanic rocks, typically occurring as unstratified breccia with granule- to cobble-sized clasts, or less commonly as massive flow rocks. Locally the volcanics contain large (1-4 mm) dark green amygdales and sparse (<10%) plagioclase microphenocrysts. Pillowed flows and chert are rare, although they are present at locality within the type area (at the end of the third access trail from the southeast shown in Figure 3). A minor amount of thinly laminated varegated tuff is also present, and may represent waterlain tuff.

Irregular dikes and small stocks of diorite are ubiquitous throughout the unit and exhibit a range of textures from aphanitic to fine-grained allotriomorphic. In thin section, the diorite is composed mostly of plagioclase with minor quartz, biotite and hornblende. These intrusions are commonly difficult to distinguish from the surrounding volcanic rocks because of their fine grain-size, similar color and irregular intrusive contacts.

Younger Tertiary dikes are also present throughout the Pacific Rim area, and can be easily confused with the older dikes, which are restricted to the Ucluth Volcanics. The Tertiary dikes are distinguished by their more tabular form, fresher appearance and intermediate composition. They also weather to a distinctive orangish color which contrasts with the surrounding green volcanics.

In contrast, the volcanic rocks and intrusions in the Ucluth unit display a patchy development of epidote-bearing alteration assemblages, presumably due to hydrothermal circulation. Locally, the volcanic rocks are converted to fine-grained amphibolite, apparently due to contact metamorphism by the intrusion of nearby diorite stocks. In thin section, these alteration assemblages are overprinted by minor amounts of prehnite, calcite and lawsonite, displaying static textures.

Irregular pods and lenses of light gray limestone are scattered throughout the unit and range up to 40 m in largest dimension. Bedding is locally apparent especially where the limestone contains significant amounts of volcanic tuff. More typically, the limestone is fine-grained, massive and unfossiliferous, although rare fragments of crinoids and gastropods are present. In one locality, bedded tuffaceous limestone contains small unidentifiable ammonoids (southern conodont locality in Figure 3). Intercalation of limestone and volcanic rock is common and indicates that the limestone bodies are part of the Ucluth unit, and are not exotic blocks.

Age. Limestone from two localities have yielded Upper Triassic conodonts (Figure 3) with ages of (1) Karnian (probably late Karnian) and (2) latest early Norian to earliest middle Norian (M. Orchard, pers. comm., 1983 - Appendix A[2]). The limestone at these particular localities is clearly interbedded with volcanic rock and thereby provides some indication of the age range of the unit as a whole. In the case of the Norian locality, the dated limestone is cut by a small diorite dike indicating a Late Triassic or younger age for the diorite intrusions. The total age range of the unit is not known, but since Lower Cretaceous mudstone of Unit 1B unconformably overlies the unit, it can be no younger than Jurassic.

---

2 Appendix A contains a compilation of all published and unpublished fossil data for the Pacific Rim Complex.

Distribution. The Ucluth Volcanics are also exposed in the northern part of the Pacific Rim Complex (northwest side of Vargas Island and Bartlett Island, Figure 2). Exposures in these areas are similar to the type area, but contain a greater proportion of unstratified medium-grained green tuff, which is also intruded by diorite dikes. Other isolated exposures of the unit occur on some of the small islets between Meares Island and Tofino.

Pillow lava, ribbon chert and green tuff are exposed on the west side of Vargas Island and on the small islands northwest of Vargas (Figure 2). These rocks bear some similarities to the Ucluth unit, but the diorite dikes and limestone are notably absent. Furthermore, the chert has yielded Lower Jurassic radiolaria. These rocks are tentatively excluded from the Ucluth Volcanics, but further work may show that they are stratigraphically related (see **PILLOW LAVA AND CHERT** below).

Geochemistry and Tectonic Setting. Samples of five volcanic rocks and two dike rocks were analyzed for major and trace elements using a Kevex Energy Dispersive XRF at the University of California at Davis. Two of these samples were analyzed again on a Baird Induction-Coupled Plasma Spectrometer (ICP) operating at the University of Washington. Thompson and Walsh (1983) describe the ICP technique and its application to rock analysis. Major elements were analyzed using an internal standard with the lithium metaborate technique; a hydrofluoric - perchloric solution was used for minor and trace elements. Solutions are used for standards, so that the ICP technique is not dependent on rock standards. An analysis of BCR-1, a USGS rock standard, done on the University of Washington ICP compares quite well with published values (Table 1). Spectra for the XRF analyses were processed using standard Kevex programs. ICP analyses were used together with 10 interlaboratory rock standards (Abbey, 1977) to determine working curves for the XRF analyses. The two techniques have yielded reasonably consistent results.

Table 1. Major and trace element data for selected volcanic rocks.

	UCLUTH VOLCANICS		UPPER JURASSIC(?) BASALTS		KARMUTSEN	USGS STANDARD BCR-1	
WT. %	VOLCANIC FLOW*	FINE-GRAINED DIORITE†	PILLOW BASALT§	SHEET FLOW**	AVERAGE OF 75 SAMPLES††	ICP ANALYSIS	PUBLISHED VALUES§§
SiO_2	53.55	49.91	53.86	48.76	47.58	55.01	54.85
Al_2O_3	16.37	18.02	16.84	13.44	14.81	13.80	13.68
Fe_2O_3 (total)	10.26	9.98	7.75	12.46	12.69	13.09	13.54
MgO	5.50	5.40	5.88	7.21	6.79	3.64	3.49
CaO	3.43	6.29	7.0	9.88	10.85	6.95	6.98
Na_2O	5.50	5.28	6.09	4.01	2.45	3.35	3.29
K_2O	1.87	1.89	0.0	0.25	0.24	1.56	1.68
MnO	0.16	0.12	0.13	0.16	0.19	0.15	0.19
P_2O_5	0.30	0.35	0.22	0.23	---	0.35	0.33
TiO_2	0.92	0.81	1.05	1.96	1.76	2.15	2.22
TOTAL	97.86	98.05	98.87	98.36	97.36	100.05	100.25
(WT. ppm)							
Zr	97	58	81	111		185	185
Nb	6	7	9	7		12	14
Sr	220	280	330	145		280	330
Y	23	18	17	36		30	37?
Ba	1230	805	130	93		600	680
Sc	28	18	31	36		27	34
Co	42	41	53	46		41	37
Cr	37	3	325	115		14	16
V	235	240	240	365		385	410
La	8	8	5	3		21	25
Zn	91	49	64	86		115	120
Cu	85	145	35	57		22	19

NOTE: Unless noted otherwise, the analyses were done on a Baird ICP at University of Washington (C. Cool, Analyst). Relative error for SiO_2: <2%; other major elements: <5%; trace elements: <10%. Detection limits are <2 ppm.

* 811013-2 NW side of Ucluth Peninsula. † 811016-5 NW side of Ucluth Peninsula.

§ 81728-2 NE side of Stubbs Island. ** 80922-6 At West Coast fault, E of Uclulet Inlet.

†† From Muller, et al. (1981). H_2O = 2.57% giving a total of 99.93%. P_2O_5 was not reported.

§§ From Abbey, 1977.

The ICP analyses are representative of the suite and are listed in Table 1. Silica content typically ranges from 47.9 to 53.4%, indicating that the volcanics and associated dikes are basaltic. However, one volcanic sample is probably an andesite, with silica of 59.6%. Metasomatic alteration has undoubtedly affected many of the major elements; most notable are the high NaO and low CaO contents. However, K_2O and Al_2O_3 are consistently high for all of the samples, especially when compared with basalts from modern ocean-floor settings (Table 2-1 in Hekinian, 1982; Hawkins, 1980) and from ancient ophiolites (Table 7 and Figure 29 in Coleman, 1977).

Immobile trace elements also indicate that the Ucluth Volcanics are distinct from ocean-floor tholeiites. The Y/Nb ratio is greater than 2.6 for all of the samples, which rules out an alkalic association (Pearce and Cann, 1973). The calc-alkaline character of these rocks is quite clearly demonstrated by the lack of any increase in TiO_2 with increasing Zr (Figure 6); almost all samples plot within the calc-alkaline basalt field using a TiO_2-Zr discriminant diagram (Pearce and Cann, 1973; Garcia, 1978). Calc-alkaline basalts are typical of modern volcanic arcs such as Japan, Java and Lesser Antilles (Pearce and Cann, 1973). The prevalence of fragmental volcanic rocks in the Ucluth Volcanics is also a common feature of modern volcanic arcs and is not typical of ocean-floor and oceanic-island volcanic settings (Garcia, 1978).

Origin and Regional Correlation. Muller (1977) and Page (1974) suggested that the volcanic rocks of the Pacific Rim Complex were derived either (1) from subducting oceanic crust or (2) from Triassic volcanic rocks of the Karmutsen Formation which underlies much of Vancouver Island to the east. Their second interpretation was attractive because limestones within the Pacific Rim could have been derived from the Quatsino Limestone which overlies the Karmutsen (Figure 5). Neither of these interpretations appears to be correct. The data presented here indicate that the Ucluth Volcanics, which comprise the bulk of the volcanic rocks of the Complex, formed within a calc-

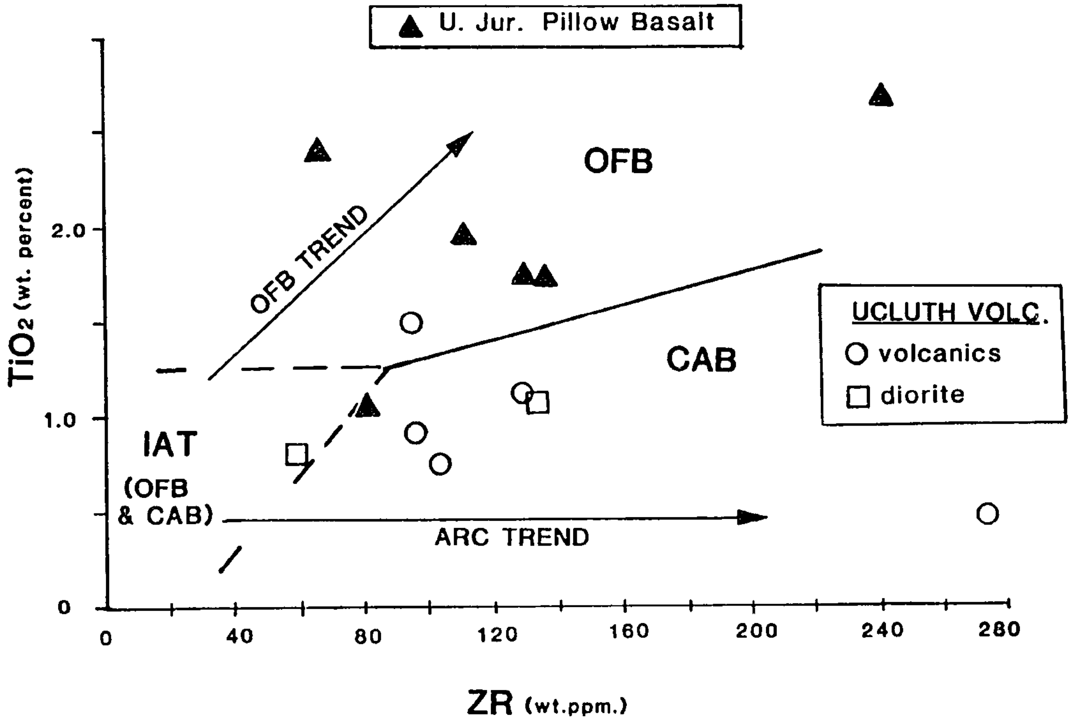

Figure 6. TiO_2-Zr relationships for the Ucluth Volcanics and Upper Jurassic basalts. Discriminant fields are from Garcia (1978) and Pearce and Cann (1978): OFB = ocean-floor basalt, CAB = calc-alkaline basalt, IAT = island arc tholeiite. Trends for ocean-floor basalts and island arc volcanics are from Garcia (1978). Relative errors for TiO_2 and Zr are less than 15% and 20% respectively.

alkaline volcanic arc. The Karmutsen is characterized by a monotonous sequence of low potassium tholeiitic basalt (compare geochemistry in Table 1), dominated by pillowed flows with subordinate pillow breccia and tuff (Muller, et al., 1981). Furthermore, the Karnian-Norian age of the Ucluth Volcanics is in part younger than the Karmutsen and Quatsino (Figure 5). The coeval Norian unit on Vancouver Island, the Parson Bay Formation, consists of calcareous clastic sediments and is devoid of volcanic rocks (Muller, et al., 1981).

In short, the Ucluth Volcanics represent a displaced Triassic arc. The absence of terrigeneous sedimentary rocks suggests that the arc might have originated in an intra-oceanic setting. Upper Triassic andesitic and dacitic volcanogenic rocks are exposed in the San Juan Islands (Haro Formation--Vance, 1975; Johnson, 1978) and, though compositionally different than the Ucluth Volcanics, may represent another piece of this arc terrane.

PILLOW LAVA AND CHERT

The Pacific Rim Complex contains a small amount of pillowed volcanics with interbedded chert. Based on age and lithology, this pillow lava - chert association can be divided into two units (Figure 4): (1) Lower Jurassic pillowed flows with tuff breccia and ribbon chert, and (2) Upper Jurassic pillow basalt with ribbon chert. These rocks are important because at least some of the pillowed volcanics appear to be ocean-floor basalts.

Age and Distribution. The only confirmed outcrop of the Lower Jurassic unit is on the west side of Vargas Island (Figure 7) where ribbon chert has yielded later Toarcian radiolaria (E. A. Pessagno, writ. comm., 1983). Undated pillow lava, tuff and chert also crop out on many of the small islands between Flores and Vargas islands and may represent more of the Lower Jurassic unit. As suggested above, the Lower Jurassic unit might be a younger part of the Ucluth Volcanics. The Ucluth unit is exposed nearby on Vargas Island and on some of the small islands between Flores and Vargas islands. Both units contain a

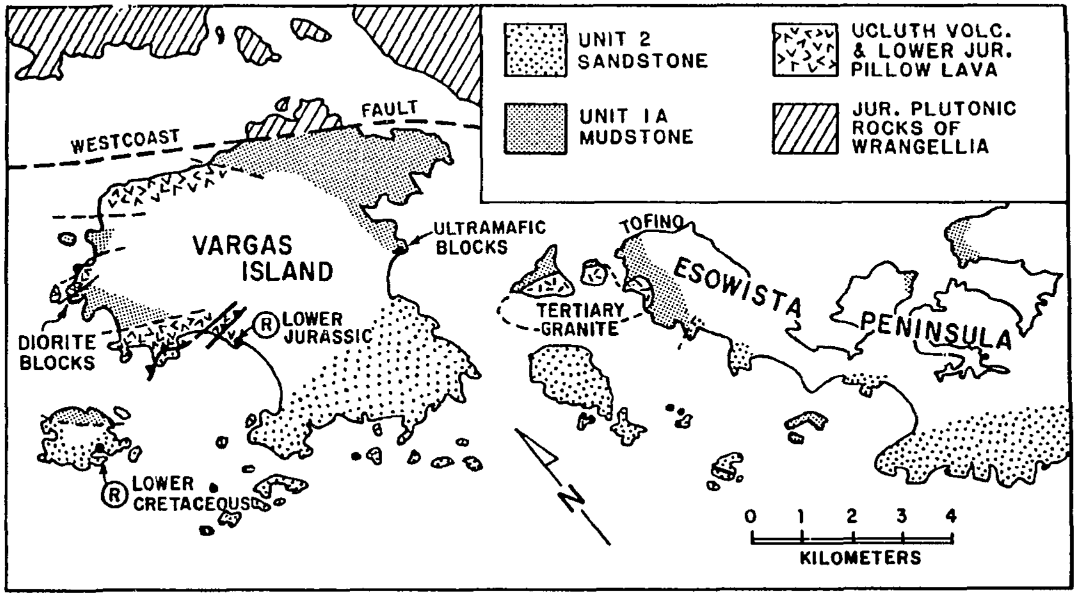

Figure 7. Geologic map of the Esowista Peninsula - Vargas Island area, located at the north end of the map area. Sandstone-rich melange of Unit 2 is extensively exposed in this area and appears to overlie older units; contact relationships, however, are not exposed. Other features include: rare ultramafic blocks in Unit 1A melange on eastern Vargas Island and Lower Jurassic pillow lava and chert on western Vargas Island.

large amount of fragmental volcanic rocks, but limestone and diorite dikes are notably absent in the Lower Jurassic unit. Lithological variations might be expected, given the age difference of the two units; however, further study of the Lower Jurassic unit is need before its relationship with the Ucluth unit can be resolved.

The Upper Jurassic unit is more widespread, but has been confidently dated in only one location (Francis Island--Figure 3; collected by J. Muller and E. A. Pessagno). Dated ribbon chert in this area is closely associated with pillow basalt and minor sandstone, and has yielded late Kimmeridgian/early Tithonian to late Tithonian radiolaria (Muller and Pessagno, writ. comm., 1983). Muller and Pessagno (writ. comm., 1983; also Muller, 1976) also dated two other Upper Jurassic chert localities from the southeast side of Ucluelet Inlet (east of Francis Island). Based on my reconnaissance mapping, these samples were probably from other outcrops of chert interbedded with pillow basalt. All three localities have yielded similar ages (Figure 4) and together indicate a late Kimmeridgian/early Tithonian age.

The Upper Jurassic unit is closely associated with mudstone-rich melange and appears to be a large exotic blocks within the melange. At Wya Point (Figure 3) and on southwest Meares Island, large blocks of pillow basalt and chert can be seen in unfaulted contact with mudstone of the surrounding melange. These two localities are undated, but they are inferred to be Late Jurassic in age and therefore older than the surrounding melange matrix, which is Early Cretaceous in age. The presence of these basalt-chert blocks is not unusual since other types of exotic blocks are also present in the melange; most of the other blocks, however, are derived from the Ucluth Volcanics. In contrast, the source terrane for the Upper Jurassic basalt-chert blocks is not presently exposed in the Pacific Rim area.

Minor amounts of chlorite, calcite, and pumpellyite (?) are present in the Upper Jurassic basalts. Lawsonite and prehnite were not observed. However, the ribbon chert interbedded with these basalts contain lawsonite, prehnite and calcite which is the assemblage characteristic of the surrounding melange matrix (see below).

Volcanic Geochemistry. Six basalt samples from the Upper Jurassic unit were analyzed for major and trace elements. Five samples were run on the U. C. Davis XRF and two of these were replicated on the University of Washington ICP (see **UCLUTH VOLCANICS** for a discussion of geochemical techniques and procedures). The sixth sample was collected by M. Dungan and R. Page and is reported in Vance, et al. (1980, see their appendix). Samples were not collected from the Lower Jurassic unit, so the geochemistry and composition of those rocks are not known.

The ICP results are listed in Table 1 and are representative of the other analyses from the Upper Jurassic unit. Silica contents indicate basaltic compositions (48.7 - 53.6%). In contrast to the Ucluth Volcanics, the Upper Jurassic basalts are characterized by higher TiO_2 and lower K_2O and Al_2O_3. Immobile trace elements indicate that these basalts are most similar to modern ocean floor basalts. Y/Nb ratios are all greater than 1.8, precluding an alkalic association (Pearce and Cann, 1973). TiO_2 increases with increasing Zr (Figure 6), and follows an ocean floor basalt trend as described by Garcia (1978). All samples with Zr greater than 90 ppm plot exclusively within the ocean floor basalt field (Pearce and Cann, 1973; Garcia, 1978) (samples with Zr less than 90 are not diagnostic because they plot in a composite field). Unpublished rare-earth element analyses for samples of Upper Jurassic basalt collected by Dungan and Page (pers. comm., 1983) display typical mid-ocean-floor basalt patterns, and support the TiO_2-Zr relationships presented here. The petrography of the Upper Jurassic basalts is also consistent with an ocean-floor eruptive setting. They typically display a glomeroporphyritic texture, with plagioclase and clinopyroxene microphenocrysts set in an altered groundmass, and closely resemble plagioclase-pyroxene basalts described from modern ocean-floor settings (Hekinian, 1982, p. 30).

Chert Depositional Setting. Basalt geochemistry is not very useful in distinguishing between different ocean floor eruptive settings, such as mid-ocean ridge and marginal basin (Hawkins, 1980). However, ribbon cherts in the Jurassic units provide additional evidence of the paleotectonic setting. Traditionally, ribbon cherts have been interpreted to be the lithified equivalents of open-ocean siliceous ooze. In a recent review, Jenkyns and Winterer (1982) have pointed out that on-land exposures of Mesozoic radiolarian ribbon cherts are quite different from Mesozoic and Tertiary cherts recovered from the ocean basins. They argue that ribbon cherts represent unusual pelagic sediments which were probably restricted to small Mesozoic ocean basins with very high rates of radiolarian productivity. In the modern oceans, high rates of biogenic siliceous sedimentation are usually confined to marginal basins where oceanographic conditions favor the upwelling of nutrient-rich bottom water. Jenkyns and Winterer (1982) suggest that marginal seas similar to the Japan Sea or Gulf of California represent modern tectonic analogues for Mesozoic basins where ribbon chert was deposited.

The petrography and geochemistry of the Jurassic ribbon cherts support this interpretation, and also indicate proximity to a felsic volcanic arc. For instance, the Upper Jurassic ribbon cherts commonly contain intervals of silty and sandy chert. In thin section, this detrital component consists of silt-sized to medium-sized grains of volcanic feldspar and quartz, locally present in thin graded laminae. These features indicate that redepositional processes were probably responsible for the intermixing of detrital grains and radiolaria.

The geochemistry of chert and other pelagic sediments is particularly useful in identifying the relative contributions of different sediment types, such as biogenic, hydrothermal, and detrital components. This approach has been used with modern pelagic sediments

(Dymond, 1981; Heath and Dymond, 1977) and more recently has been successfully applied to Mesozoic cherts (Karl, 1983). Six radiolarian ribbon cherts--4 from the Upper Jurassic unit and 2 from the Lower Jurassic unit--were analyzed using the ICP at University of Washington (Brandon, unpublished data). The mixing model of Dymond (1981) was used to determine the relative amounts of different sediment types in the chert. The main results are summarized below (these data will be present in detail elsewhere).

These cherts are composed almost entirely of two components: a dominant biogenic component (65-90 wt.%), and a subordinate detrital component (10-35 wt.%). Despite their close association with pillow lava, the cherts contain relatively little metalliferous hydrothermal sediment (<2 wt%). Hydrothermal sediments are typically in abundance around volcanically active ridges in the modern oceans. For instance, pelagic sediments in the vicinity of the East Pacific Rise typically contain a hydrothermal component of about 80% (Dymond, 1981). A possible explanation is that the hydrothermal component was diluted by high rates of biogenic sedimentation. High biogenic rates are also indicated by the low-barium contents of the chert, and by the absence of a significant dissolution residue component (see Dymond, 1981). These factors are quite compatible with the highly productive, small ocean basins that Jenkyns and Winterer (1981) envision as the typical depositional setting for Mesozoic ribbon chert. In fact, their estimates of accumulation rates for typical Mesozoic ribbon chert are much higher than the accumulation rates of hydrothermal sediments at the East Pacific Rise (Dymond, 1981), which supports the dilution interpretation suggested above

The geochemical data also confirms the presence of a volcanic detrital component. Potassium content in the chert increases linearly with increasing detrital component, indicating a felsic volcanic source with average K_2O content of 3 - 3.5%. Detrital accumulation rates must have been similar to the biogenic rates in order to maintain a significant detrital component. If the small-basin interpretation is correct, the volcanic detrital component suggests an intra-arc or back-arc basin setting, perhaps similar to the modern Japan Sea (as described by Karig and Moore, 1975).

Origin and Correlation. The evidence given above suggests that the Jurassic units formed in a small ocean basin, in proximity to an eroding volcanic arc. The presence of ocean-floor basalts in the Upper Jurassic unit indicates active spreading during the Late Jurassic. The Lower Jurassic pillowed flows may have formed in a similar setting, or alternatively may represent arc volcanics related to the Ucluth unit.

Presently, the Upper Jurassic unit occurs as large exotic blocks within mudstone-rich melange. The source of these blocks is nowhere exposed in the Pacific Rim area. Late Jurassic ophiolitic rocks are present in the San Juan Islands (Brown, et al., 1979; Vance, et al., 1980) and may represent part of a once more extensive source terrane for the Upper Jurassic blocks in the Pacific Rim Complex. Vance, et al. (1980) have also suggested that the San Juan ophiolitic rocks formed within small ocean basins marginal to a Late Jurassic arc.

LOWER CRETACEOUS MELANGE UNITS

The Pacific Rim melanges comprise almost all of the sedimentary rocks of the complex. Where best exposed on the Ucluth Peninsula (Figure 3), these melanges preserve a crude stratigraphic succession consisting of two basal mudstone-rich melanges, Units 1A and 1B, grading upward into a sandstone-rich melange, Unit 2 (Figure 4). Units 1A and 1B occur on opposite sides of the large east-west trending anticline on the Peninsula, and unconformably overlie the Ucluth Volcanics, exposed in the core of the anticline. These two units are nowhere exposed together; however, similarities in age and stratigraphic position, together with the prevalence of black mudstone in each, indicate that they are probably laterally equivalent. There are differences in lithology and style of disruption. Unit 1A contains a greater proportion of chert and is characterized by a planar fabric, whereas Unit 1B is more highly contorted and contains graded turbidite sandstone, conglomerate and pebbly mudstone.

Sandstone in all three of these melange units contain minor amounts of prehnite, lawsonite and calcite. This assemblage is also locally present in chert of these melanges. The significance of this very low temperature-high pressure metamorphic assemblage is discussed below in another section.

UNIT 1A--MUDSTONE-RICH MELANGE

Lithology, age, and distribution. Unit 1A is best exposed at Wya Point on the north side of the anticline (Figure 3). In this area, the melange is at least 400 m thick, not including the large block of pillow basalt on the north side of the Point. The unit consists of fragments and lenses of chert, sandstone and minor green basaltic tuff, organized in a planar fabric and surrounded by black mudstone matrix (Figures 8 and 9). Unit 1A has yielded three Early Cretaceous radiolarian chert localities (late Valanginian to late Aptian--

Figure 8. Photographs of various structures in Unit 1A melange. Figure 8a shows a typical example of the planar fabric of the melange, defined by tabular layers of sandstone (ss) and ribbon chert (ch), and also by oriented fragments of chert and sandstone. The surrounding matrix consists of black mudstone. Figure 8b is a close-up of part of the view shown in Figure 8a (upper right corner). The ellipsoidal and spheroidal fragments consist mostly of chert (rock hammer shown for scale). Figures 8c and 8d are typical of some of the irregular pods of sandstone present in the melange. The tail-like feature in Figure 8c represents an injection of sand into the surrounding mudstone (note the knife and Brunton compass shown for scale).


CH

Figure 8. (continued)

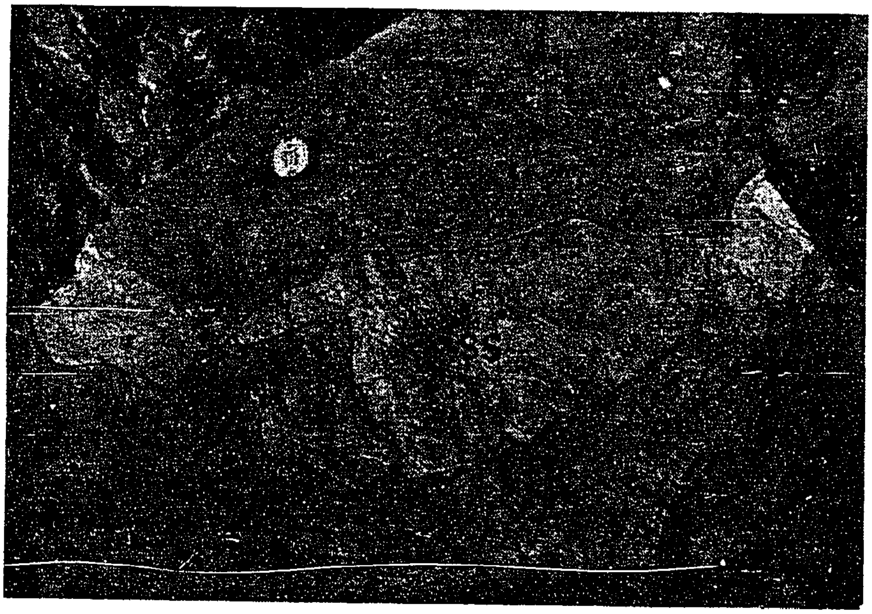

Figure 9. Detailed map of melange fabric in Unit 1A. The oblique photo was used as a base map; photo and map face to the south. The contact of Unit 1A with the underlying Ucluth Volcanics probably lies within 50 m of the right (east) side of the map. The prominent chert lens in the center of the map has yielded Lower Cretaceous radiolaria. The large diorite block shown on the left side of the map is 45 m long and 6 m wide.

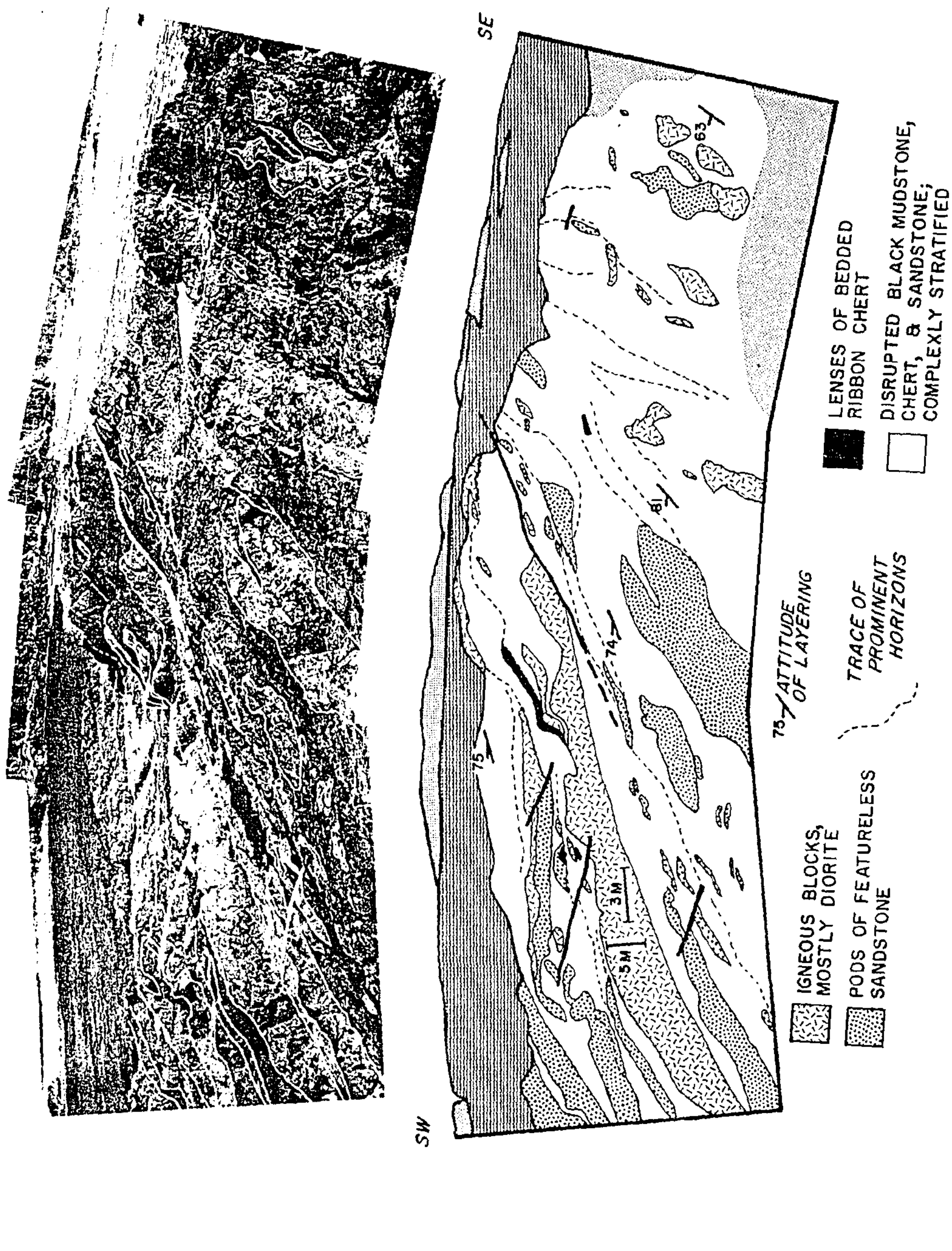
SE
SW
63
81
74
75
3M
5M
LENSES OF BEDDED RIBBON CHERT
DISRUPTED BLACK MUDSTONE, CHERT, & SANDSTONE; COMPLEXLY STRATIFIED
75 ATTITUDE OF LAYERING
TRACE OF PROMINENT HORIZONS
IGNEOUS BLOCKS, MOSTLY DIORITE
PODS OF FEATURELESS SANDSTONE

Pessagno, writ. comm., 1983). These dated cherts are clearly interbedded with the matrix of the melange, and therefore indicate an Early Cretaceous age for the matrix as well. The melange also contains numerous exotic blocks of igneous rock, which were mostly derived from the underlying Ucluth Volcanics (Figures 9 and 10).

The Unit 1A melange probably rests depositionally on the Ucluth Volcanics, a relationship that can be demonstrated for Unit 1B. This contact, however, is only locally exposed at Wya Point (Figure 3) where it is faulted and difficult to interpret. A depositional contact cannot be proven, but is supported by: (1) the presence in the melange of blocks derived from the Ucluth Volcanics, (2) a younger-over-older relationship with Lower Cretaceous melange on Upper Triassic volcanics, and (3) the concordance of the melange fabric with the underlying contact.

Internal Structure. Despite the pervasive disruption, the melange still retains a well-layered, planar fabric. The chert and sandstone tend to have oblate and spheroidal shapes (Figures 8 and 9), but range considerably in size and aspect ratio. The oblate fragments define a very consistent foliation, called a fragment foliation (a term coined by D. S. Cowan, pers. comm., 1984). This structure resembles boudinage; however, instead of the "sausage-like" shapes typical of boudinage (Ramsey, 1967); these sandstone and chert layers are disrupted into pancake-shaped fragments, as if the layers have been extended in all directions parallel to layering (cf. Cowan, 1982b). It should be noted that, instead of layer-parallel extension, these boudin-like structures may have formed by a non-extensional process involving lateral flowage and thickening: this point is discussed in more detail in another section below. Thicker lenses of sandstone and chert (> 1m) are concordant with the fragment foliation and tend to be less deformed and more laterally persistent (Figure 8a). In areas without thick lenses, the melange still maintains a layered appearance defined by subtle variations, on the scale of 1 to 2 m, in the relative proportion of chert and sandstone in the mudstone. This

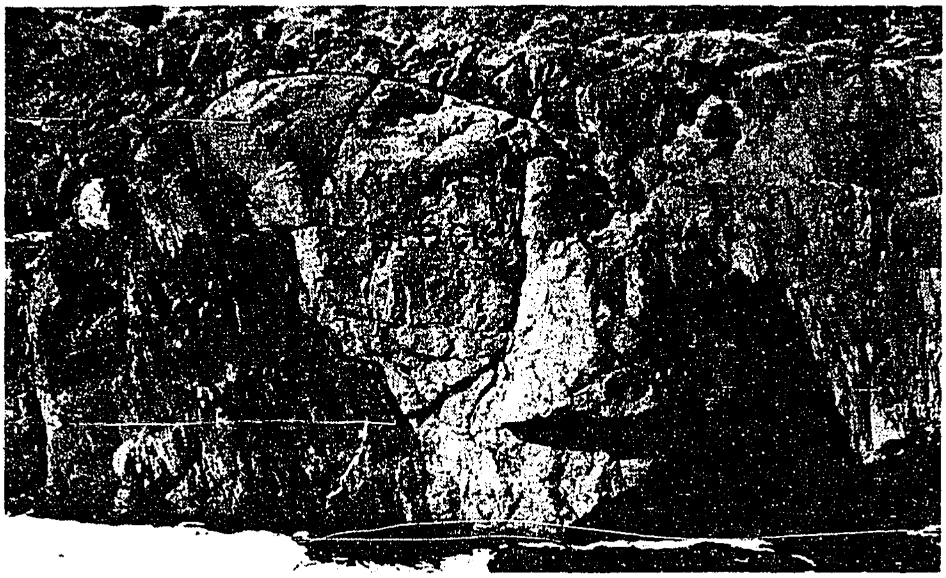

Figure 10. Photograph of a large diorite block in Unit 1A melange. The block is about 4.5 m thick and extends for more than 35 m along strike. Contacts with the surrounding melange are irregular and unfaulted.

planar fabric is very consistent, not only at a local scale but also at map scale. As shown in the stereonet in Figure 11, the fabric at Wya Point dips moderately northeast and is concordant to the contact of Unit 1A with the underlying Ucluth Volcanics (Figure 3)

The extreme mobility of sandstone, chert and tuff indicate that deformation occurred prior to lithification and while the sediments were still quite soft. Green tuff is present in thin wispy layers, and sandstone bodies commonly display irregular podiform shapes (Figures 8 and 9). Locally these pods are associated with small sandstone dikelets injected into the surrounding mudstone (Figure 8c). Internally, the lenses and pods consist of homogeneous medium- to fine-grained sandstone. The mobility of the sand during deformation has apparently obliterated any primary sedimentary structures. The same is apparently true for the chert. Fragments and small balls of chert contain no observable bedding features. Thicker lenses, however, still preserve well-bedded and undeformed radiolarian ribbon chert.

Because of the homogeneous nature of the mudstone matrix, it is difficult to determine how much deformation has occurred within the matrix. However, the mudstone does not contain a scaly or slickensided foliation, a feature commonly observed in many other mudstone-rich melanges (Cowan, in press). A pressure-solution cleavage is sporadically present but appears to be unrelated to melange deformation.

The intimate association of sandstone, chert, green tuff and mudstone throughout the unit indicates that these rocks are all interbedded components of the melange matrix. Thin sandy interbeds are present in the lenses of ribbon chert and attest to their association with the surrounding clastic sediments. This relationship is supported by the geochemistry of these cherts (Brandon, unpublished data), which indicates the presence of a large felsic detrital component (20-40 wt%). The geochemistry of the green tuffs (Brandon, unpublished data) suggest that they were derived from an ocean-floor

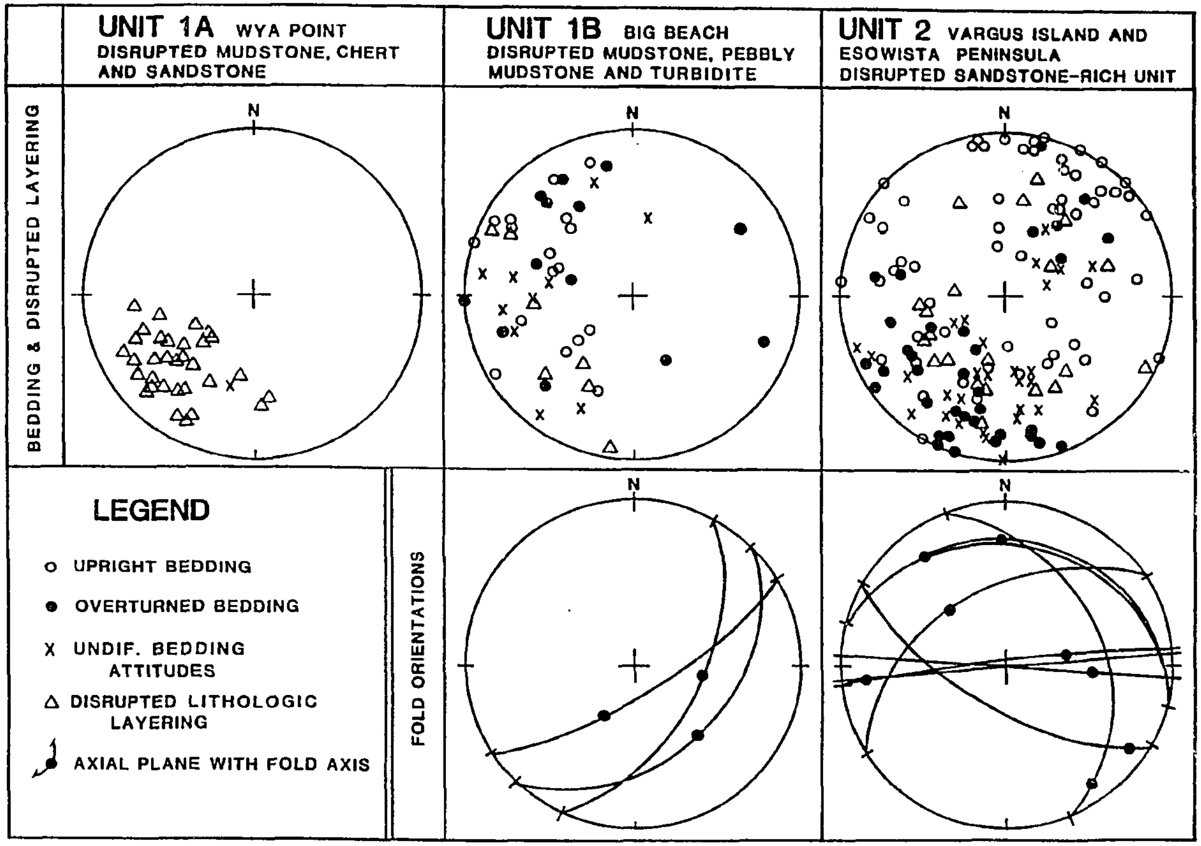

Figure 11. Stereonet plots of structural features in the melange units (equal-area projection). These stereonets show the contrast between the planar fabric of Unit 1A and the chaotic and folded fabric of Units 1B and 2.

basaltic source. They may indicate contemporaneous basaltic volcanism; alternatively, these tuffs may have been reworked from an older source, such as the Upper Jurassic basalts.

Exotic Blocks. The igneous blocks represent the only exotic elements in the melange. These blocks generally have slab-shaped profiles, with lengths about seven times their thickness, and tend to be strongly oriented, with their long dimensions parallel to the melange fabric (Figure 9). As noted above, most blocks were derived from the Ucluth Volcanics, consisting mostly of diorite, but also including minor volcanic rocks and rare limestone. The largest diorite block occurs in Unit 1A melange on the west side of Vargas Island (Figure 7) and is about 190 m thick and of unknown length. At Wya Point, diorite blocks reach a maximum size of 45 m long and 6 m thick (Figure 9). Other types of blocks, such as Upper Jurassic pillow basalt and chert discussed above are also present in minor proportions. For instance, an undated sequence of pillow basalt, about 220 m thick, is exposed on the north side of Wya Point (Figure 3) and probably represents an exotic block. On the east-side of Vargas Island (Figure 7), the melange contains several slabs of clinopyroxenite, a rock type that is not observed elsewhere in the Pacific Rim Complex.

Origin. Unit 1A probably originated as an interstratified sequence of mudstone, chert, sandstone and tuff. Melange deformation has disrupted this sequence, but it has not markedly distorted its original stratified geometry. For this reason, and others, deformation of the sedimentary components of Unit 1A is envisioned to have occurred in-situ, probably as the result of liquefaction during large earthquakes. This interpretation is discussed in more detail below.

The exotic blocks in the melange are thought to represent submarine rock falls which were locally derived from steep rocky escarpments, underlain predominantly by Ucluth Volcanics. This interpretation is compatible with the large size of the blocks--generally boulder size and larger--and their angular, elongate shapes. There is no evidence that the blocks were reworked from shallow water or subaerial settings, since the clasts are not rounded. Furthermore, Unit 1A contains no conglomerate or pebbly mudstone. In any case, a debris-flow origin does not appear to be compatible with the well-organized planar fabric present in the melange matrix.

What seems odd is that there is no obvious evidence in the surrounding melange of shear surfaces, folds or other structures that might have been associated with emplacement of these blocks. A possible explanation is that these blocks were moving fairly fast when they were emplaced onto the soft, muddy bottom, and therefore slid for some distance. Under these conditions, the moving block would impose an undrained load on the sediments, and would probably generate fluid pressures great enough to decouple the sole of the block from the underlying mud. The large aspect ratio of the blocks would prevent them from sinking into the soft muddy bottom; Naylor (1982, Figure 10a) estimates that blocks with aspect ratios greater than 6.5 can be fully supported under these conditions.

UNIT 1B-MUDSTONE-RICH MELANGE

Unit 1B is best exposed in the Big Beach area, on the south side of the Ucluth anticline (Figure 3). In comparison with Unit 1A, this melange contains a greater diversity of clastic rocks and is more highly contorted and internally folded. The unit is dominated by massive and laminated mudstone, with subordinate sandstone turbidite, channelized conglomerate, pebbly mudstone and ribbon chert. Exotic blocks of fragmental volcanic rocks are present, but are confined to pebbly mudstone.

Age. Fossils from Unit 1B indicate an Early Cretaceous age. **Buchia** are present in a number of localities in the laminated mudstone, typically in rare interbeds composed entirely of reworked shells. J. A. Jeletzky (writ. comm., 1983; also in Muller, et al., 1981) has identified these fossils as early to middle Valanginian in age. Three radiolarian localities from ribbon chert have yielded nearly identical ages (late Valanginian to early Hauterivian--Pessagno, writ. comm., 1983), thus confirming the Early Cretaceous age of the unit. A number of large bivalves are also present in laminated mudstone and in mudstone interbeds of the turbidite sequences (localities labelled as **Inoceramus**? in Figures 12 and 13). These bivalves are not age diagnostic, but they occur in growth position and therefore can be used to constrain the original depositional setting of the sediments now incorporated in the melange.

Basal Contact. Unit 1B melange rests unconformably on Ucluth Volcanics. This unconformity is exposed north of Big Beach and can be traced eastward based on isolated exposures of Ucluth Volcanics in the Big Beach area (Figure 3). Figure 12 shows a detailed map of part of this unconformity. The contact dips moderately to the south and east, and has been offset and repeated by a number of high-angle faults with both right-lateral and left-lateral separation. This situation illustrates how younger faults in the Pacific Rim area have obscured primary contact relationships, especially in areas with limited exposure. At the contact, **Buchia**-bearing mudstone rests directly above Upper Triassic limestone and volcanic rocks of the Ucluth Formation, in clear depositional contact. The mudstone above the contact at least locally appears to be a debris flow with randomly oriented **Buchia** surrounded and supported by a homogeneous mudstone matrix.

Lithology. The detailed map of the Big Beach area (Figure 13) displays typical map-scale relationships between the lithological components of the Unit 1B melange. Melange deformation has resulted in a highly disorganized assemblage. Despite the chaotic appearance, bedding features and sedimentary structures are commonly preserved at outcrop scale.

Mudstone in the melange is either massive or, more commonly, interbedded with thin silty laminae and rare sandstone interbeds. Trace fossils and other evidence of infauna are rare. Calcareous

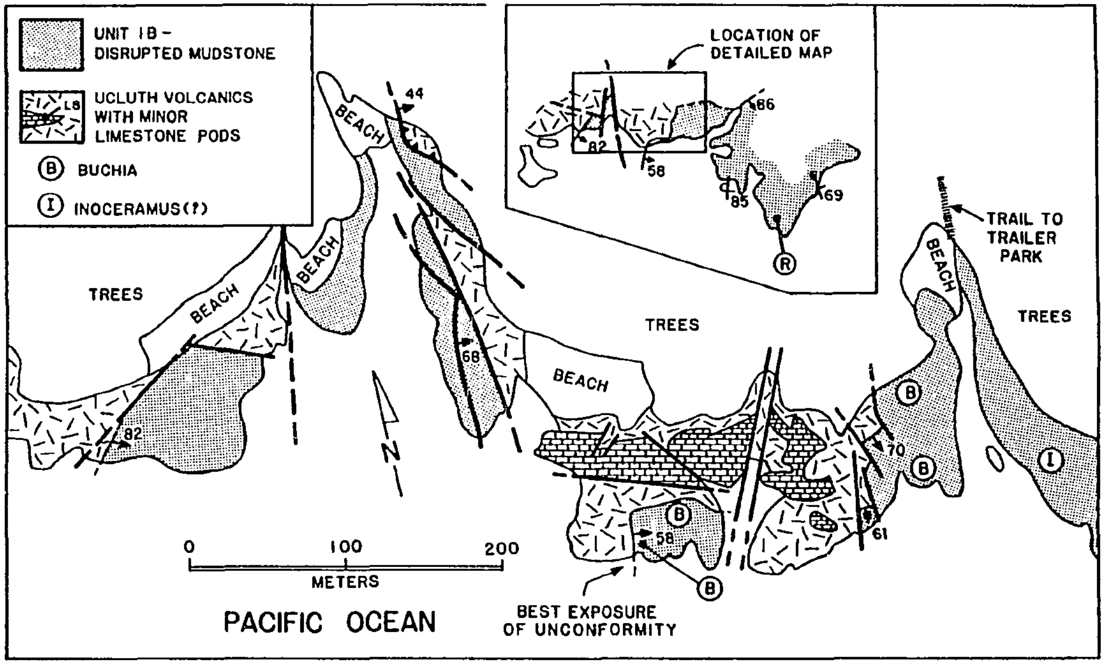

Figure 12. Outcrop map showing the basal unconformity of Unit 1B on the Ucluth Volcanics. The inset is from Figure 3 and shows the location of the detailed map. The basal contact is offset and repeated by a number of steep faults. Therefore, it might help to refer to the schematic version of the contact shown in the inset. The unconformity is fairly irregular on a small scale, suggesting that the surface had some local relief. Note that in the center of the map, Lower Cretaceous **Buchia**-bearing mudstone rests directly above the Ucluth Volcanics.

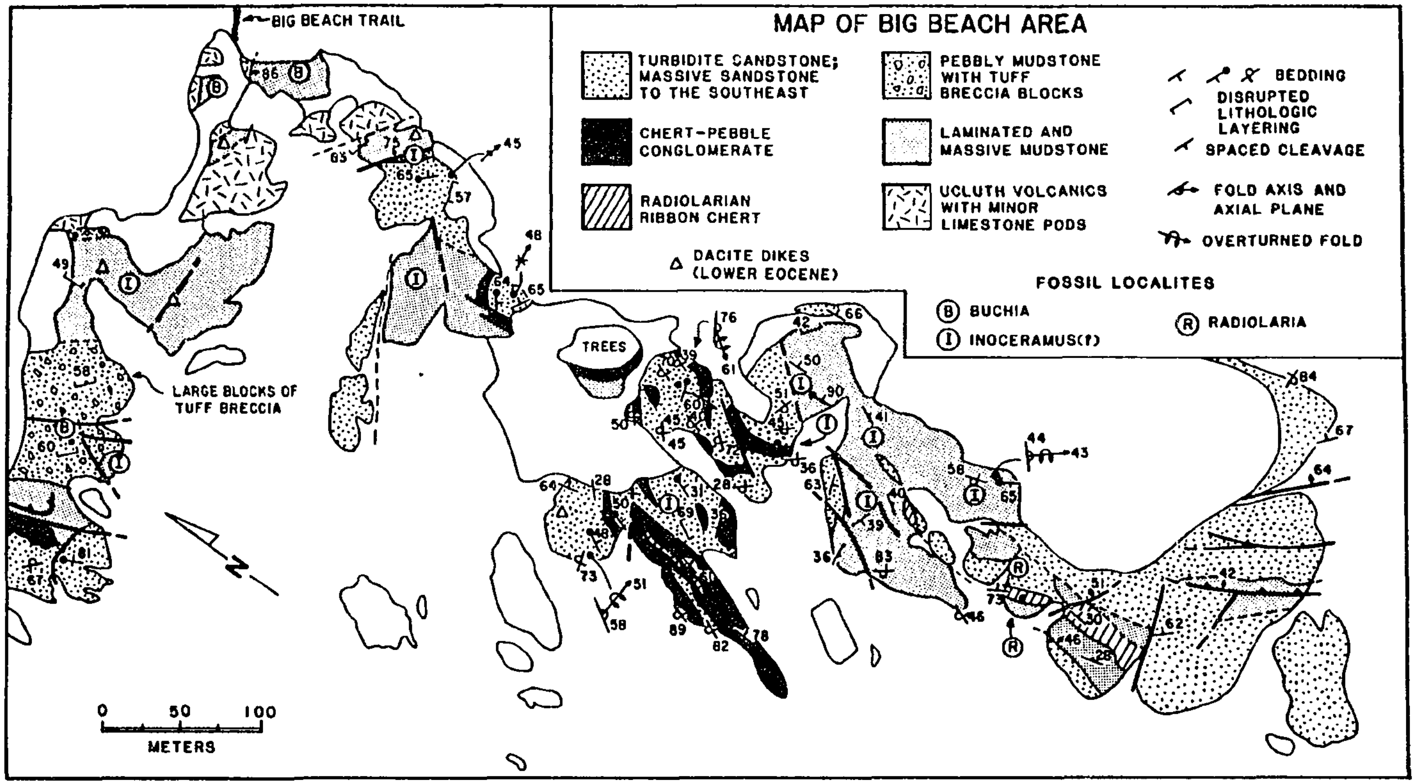

Figure 13. Detailed map of the Big Beach area showing the deformational style of Unit 1B. Melange deformation has resulted in a chaotic arrangement of upright and overturned strata. Exotic blocks are confined to pebbly mudstone. **Buchia** and radiolaria are Early Cretaceous in age. Unidentifiable bivalves, labelled **Inoceramus**(?), are common in this area and occur at localities labelled I.

concretions are also present throughout the mudstone. These features are typical of mudstone deposited under restricted oxygen conditions (Johnson, 1978).

Sequences of coarser clastic rocks are composed of sandstone turbidites with interbedded mudstone and channelized conglomerate bodies. The sandstones range in bedding thickness but are generally medium to thickly bedded with sandstone/mudstone ratios of 3 to 6, and locally greater. Thicker sequences of massive sandstone are exposed on the southeast side of the map area and probably represent amalgamated turbidite beds. Interbedded conglomerate lenses are composed of well rounded, granule- to pebble-sized clasts, consisting predominantly of radiolarian chert (green, gray and white) with minor shale, sandstone and intermediate plutonic rock. These conglomerates are clast-supported with a sandy matrix, and are typically well organized and locally graded.

Pebbly mudstone is exposed on the southwest side of the map area (Figure 13) and consists of black mudstone with well-rounded green volcanic clasts (Figure 14a). Clast size generally ranges from granule to small boulder, but larger blocks, up to about 4 m, across are locally present (Figure 14d). Clasts are all volcanic, predominantly tuff and tuff breccia with minor flow rocks. Diorite clasts were not observed, but the volcanic clasts are similar to parts of the Ucluth Volcanics. The pebbly mudstone is matrix-supported and generally lacks an organized fabric. Locally, it has a layered appearance defined by the preferred orientation of elongate clasts and variations in the relative proportions of clasts.

Chert is rare within Unit 1B, but a seven-meter-thick sequence of ribbon chert is exposed on the southwest side of the Big Beach map area (Figure 13) and is clearly interbedded with mudstone and sandstone of the melange. The sequence consists mostly of gray-green radiolarian ribbon chert with subordinate sandy ribbon chert. These cherts together with a small chert lens in massive sandstone have yielded the Early Cretaceous radiolaria described above.

Internal Structure. Rotated and overturned strata are the most visible effects of melange deformation in Unit 1B. Bedding attitudes from the Big Beach areas, plotted as S-poles on a stereonet (Figure 11), form a crude girdle pattern with a moderately plunging, east-trending axis. Despite this girdle pattern, conventional fold geometries and large-scale fold closures are not commonly observed. Locally strata are contorted into irregularly shaped folds, but more commonly, thick concordant sequences of upright or overturned strata appear to be bounded by discrete slip surfaces. Some rotation could have occurred on listric-shaped slip surfaces, but overturned strata are difficult to explain by this process alone. More likely, these slip surfaces have dismembered larger-scale overturned folds.

Several isoclinal folds are present in the southeast half of the Big Beach area, where bedding attitudes are commonly overturned. These isoclines have amplitudes of 1 - 3 m and occur as isolated folds with detached limbs. They share a similar axial planar orientation but have divergent fold axes (Figure 11). This type of fold geometry has been recognized in ancient subduction complexes (Moore and Wheeler, 1978), as well as in slumps of surficial sediments (Hansen, 1971; Woodcock, 1976), and is thought to form within broad zones of simple shear deformation. Because the isoclines at Big Beach occur as detached folds, their fold asymmetry cannot be determined. However, the average dip of the fold axial planes and overturned strata suggest a northwest sense of vergence (see Woodcock, 1976, p. 96).

Layer-parallel extension has locally affected sandstone beds in Unit 1B (Figure 14c). In contrast to Unit 1A, extension has occurred in only one direction. Furthermore, sedimentary structures are still preserved in the extended beds, indicating the sandstone was relatively rigid during deformation and was not affected by liquefaction or pronounced swelling. As can be seen in Figure 14c, some beds have extended by necking and the formation of lenticular boudins, whereas others have extended along small normal faults, resulting in discrete rotated blocks. Cowan (1982b) has described similar extensional structures present in melanges of the Franciscan Complex.

Figure 14. Photographs of pebbly mudstone and boudinaged sandstone in Unit 1B melange. Figure 14a shows a typical pebbly mudstone with large clasts of volcanic rock. The presence of rounded clasts and their lithologic similarity with parts of the Ucluth Volcanics suggests that they were derived from a subaerially exposed portion of the Ucluth unit. Figure 14b shows one of the largest clasts in the pebbly mudstone. This clast is about 4 m across and consists of volcanic tuff breccia. Figure 14c shows an example of layer-parallel extension in turbidite beds of Unit 1B (staff on right side of photo is 1.5 m long). The beds have extended mostly by shear failure along small normal faults, resulting in a series of rotated blocks.

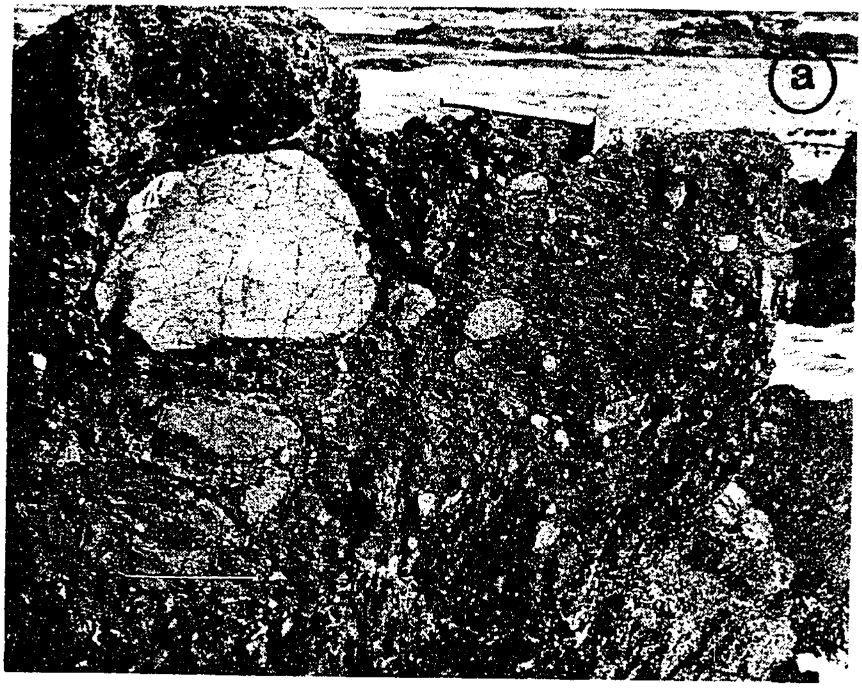
a


b
VOLCANIC
BLOCK

Figure 14. (continued)

A spaced cleavage is sporadically developed in Unit 1B, especially in the mudstone, and occurs in two orientations, dipping moderately to the southeast and to the northeast. The cleavage is axial planar to one of the isoclinal folds, but is not present in the other two, and therefore does not appear to be related to folding. The presence of insoluble residues along cleavage surfaces, and the absence of metamorphic recrystallization indicate that cleavage has formed by pressure solution (cf. White and Knipe, 1978), probably after lithification. The sporadic and semi-penetrative nature of the cleavage indicate relatively minor strains during cleavage formation. Therefore, the cleavage is envisioned to be a late-stage deformational feature which has overprinted an older melange fabric.

Original Depositional Setting of Turbidite Sequences. The initial site of deposition for the sedimentary components in this melange was apparently within a submarine-fan system. The association of sand-rich turbidite sequences with channelized conglomerates suggests an inner fan depositional setting (Mutti and Ricci-Lucchi, 1978; Walker and Mutti, 1973). Pebbly mudstone and other mudstone-rich sequences probably represent base-of-slope and interchannel deposits. The rounded clasts present in pebbly mudstone and conglomerate indicate that the Ucluth Volcanics and radiolarian chert were subaerially exposed in the source area.

Fossil evidence suggests that this postulated submarine fan was located in relatively shallow water depths. This evidence is important because the subduction accretion model (see Karig, 1983) predicts that subduction zone deformation is largely confined to deeper-water trench-fill sediments. Large reclined bivalves, up to 175 cm across occur in growth position parallel to bedding, in laminated mudstone and also in mudstone interbeds of turbidite sequences (localities labelled as **Inoceramus**? in Figures 12 and 13). E. G. Kauffman (pers. comm., 1983) has examined samples and photographs of these fossils and concluded that they represent large inoceramid-like bivalves (see Appendix A for a more complete report). While their genus and species is unknown, Kauffman suggested that they probably occupied the same habitats as some of the larger species of Cretaceous **Inoceramus** based on similarities in size, morphology and reclining form (see Jablonski and Bottjer, 1983; Kauffman, et al., 1977 and references cited there). **Inoceramus,** including some large species, are common in Lower Cretaceous strata exposed elsewhere on Vancouver Island and Queen Charlotte Islands (Longarm Formation--Muller, et al., 1974; Brown, 1968). Thiede and Dinkelman (1977) have reviewed the numerous occurrences of **Inoceramus** in Upper Mesozoic strata recovered by the Deep Sea Drilling Project. Relatively accurate estimates of original water depth can be determined for many of these occurrences. Thiede and Dinkelman (1977) concluded that **Inoceramus** was confined to upper bathyal and neritic environments (i.e., water depth of about 2000m and shallower) at continental margins and oceanic islands. Therefore, the large in-situ bivalves at Big Beach suggest similar water depths (Kauffman, pers. comm., 1983).

This fossil evidence, together with the abundance of terrigeneous-derived detritus in the sandstones and conglomerates, suggest a continental slope basin setting in relatively shallow water. This type of setting does not exclude a subduction zone interpretation for the melanges; however, it does imply that the basinal strata had to be transported into deeper water by some mass-movement process before they could become involved in the subduction- accretion process.

UNIT 2--SANDSTONE-RICH MELANGE

Lithology, age, and distribution. The sandstone-rich melange of Unit 2 appears to overlie Units 1A and 1B with a gradational contact. This relationship is, best preserved at the south end of the Ucluth Peninsula (Figure 3), where the transition from Unit 1B to Unit 2 is marked by a gradual increase in the amount of sandstone. To the north on the Esowista Peninsula (Figures 2 and 7), Unit 2 appears to overlie Unit 1A melange; contact relationships, however, are not exposed. The age of Unit 2 is not known, but based on its similarity with Unit 1B, an Early Cretaceous age is inferred (Hauterivian or younger--Figure 4).

Unit 2 is composed almost entirely of sandstone (less than 10% mudstone) and most commonly occurs in massive exposures with little evidence of internal bedding and structure. Thick- to medium- bedded turbidites are locally interbedded with the massive sandstone. Minor interbeds of clast-supported conglomerate are also present and typically consist of well-rounded clasts ranging from granule to cobble size. Most clasts are intermediate and silicic volcanic rocks, with minor calcareous sandstone, diorite and shale.

Internal Structure. The deformational style of Unit 2 is very similar to Unit 1B. Stereonets in Figure 11 show bedding and fold orientations for sandstone-rich melange exposed in the Vargas Island- Esowista Peninsula area (Figures 2 and 7). Bedding attitudes and fold orientations are highly variable; upright and overturned beds occur without any systematic pattern. Folds in Unit 2 tend to be more coherent than in Unit 1B. They have amplitudes of 1 - 3 m and are generally isoclinal or tight. In some places, overturned strata occur in coherent slab-like sequences, ranging up to 375 m thick. These sequences are similar to overturned slabs in Apennine olistostromes (Hsu, 1967). If these sequences in Unit 2 were overturned by folding, their dimensions indicate fold amplitudes greater than 500 m.

In contrast to the other melanges, extensional features are not common. Discrete slip surfaces are present, and locally can be observed to juxtapose folded and unfolded strata. In general, folding and failure in Unit 2 has occurred in a cohesive and plastic fashion, similar to Unit 1B. Locally, however, some well-bedded sandstones show evidence of liquefaction, which has variably distorted and obliterated internal sedimentary structures. The absence of sedimentary structures in massive sandstone may also be due to liquefaction after deposition, or instead may merely reflect the original depositional process.

ORIGIN OF MELANGES BY MASS-MOVEMENT DEFORMATION

EVIDENCE FOR MASS-MOVEMENT DEFORMATION

Previous workers (Muller, 1973, 1977; Page,1974) suggested that the Pacific Rim melanges formed within a subduction complex, assembled by accretion of abyssal sediments and ocean-floor basalts from the down-going plate, and by tectonic erosion of older rocks from an overriding plate represented by the Wrangellia terrane of Vancouver Island. The following results of my study argue against a subduction-zone interpretation:

(1) The melanges are underlain depositionally by an older basement composed of arc volcanic rocks and not by oceanic crust. Furthermore, rounded cobbles in pebbly mudstones were derived from this basement and indicate that it probably was subaerially exposed prior to Early Cretaceous melange formation.

(2) Exotic blocks do not represent fault slices, but instead appear to have been introduced into the melange by submarine rock falls and by muddy debris flows.

(3) The Complex does not display any significant evidence of thrust imbrication, fault-zone deformation or older-over-younger relationships, all features that characterize well-documented ancient subduction complexes (see Leggett, et al., 1982; Moore and Karig, 1980; Moore and Allwardt, 1980).

(4) The large bivalves in Unit 1B indicate that at least some of the sediments in the melange were initially deposited at relatively shallow depths, and therefore do not represent trench-fill turbidites.

(5) Ribbon cherts in the Pacific Rim Complex are unlike abyssal siliceous oozes and cherts from the modern ocean basins. Furthermore, Lower Cretaceous ribbon chert in the melange is clearly interbedded with mudstone and sandstone, indicating a continental-margin setting.

My interpretation is that chaotic deformation occurred during surficial mass movement of unconsolidated sediments. The Pacific Rim melanges have a number of features similar to other well-established sequences of mass-movement deposits (Woodcock, 1979; Helwig, 1970; Hoedmaker, 1973), which include: (1) diversity of structural styles, (2) variability in form and geometry of folds, (3) development of isoclinal folds and boudinage without associated cleavage or cataclasis, and (4) chaotic arrangement of upright and overturned strata. This deformational style is quite unlike that produced during conventional folding and thrust faulting, even in areas where on-land thrust systems have overridden and imbricated unconsolidated foreland basin sequences (e.g., Figure 6 in Price, 1981). Admittedly, there is no consensus as to how unconsolidated sediments deform within subduction zones (Cowan, in press; Bachman, 1978; Cloos, 1982; Byrne, in press; Karig, 1983; also Part 2 below). However, a less chaotic structural style should be expected within more deeply seated deformational settings, because the deforming mass is confined on all sides and therefore must deform in a relatively coherent fashion. The structural variability that appears to typify mass-movement deformation reflects, in part, the relatively unconfined, near-surface deformational environment. In this setting, deformation is probably more highly influenced by local variations in slope angle and physical properties of the deforming sediments (for discussion, see Helwig, 1970). Another factor that also contributed to this structural variability is that a section of mass-movement deposits is accumulated by sequential emplacement of different mass-movement deposits, each of which has moved and/or flowed independently of the other.

CAUSE OF MASS-MOVEMENT DEFORMATION

If this mass-movement interpretation is correct, it seems surprising that such a large body of sediment could be so pervasively affected. Almost all outcrops of the sedimentary rocks of the Complex show some degree of soft-sediment deformation! This suggests a very unstable source area, of the mass-movement deposits, and yet the presence of sandstone beds in all of the melanges indicates that this unstable source area was also a basinal setting with rather gentle slopes.

Failure and mass movement can occur on gentle submarine slopes (see review by Schwarz, 1982), but only in rather special situations, such as: (1) deltaic regions where rapid accumulation of muddy sediments creates high pore pressures (for example, Mississippi delta--Coleman and Prior, 1982); (2) regions underlain by sensitive clays, and (3) areas affected by frequent earthquakes. Indirect evidence indicates that muds in the Pacific Rim were deposited slowly, especially in comparison with the average rate of 1 m/yr for the Mississippi delta (Coleman and Prior, 1982). The large in-situ bivalves in mudstone of Unit 1B were adults, probably about 10-30 years old (Kauffman, pers. comm., 1983). Accumulation rates must have been relatively slow for these epifaunal bivalves to survive. The ubiquitous presence of radiolarian chert in mudstone of Unit 1A also indicates slow accumulation rates; Jenkyns and Winterer (1982) report a range of 50-500 cm/kyr for modern and ancient siliceous sediments.

The second situation is also unlikely. Sensitive clays are most typically developed in glacial sediments (Skempton, 1970; Torrance, 1983). The development of weak bonds between clay particles allows these clays to maintain an unstable, and highly porous structure. Physical disturbances or changes in pore water chemistry can cause this structure to collapse with a very large reduction in strength. Highly sensitive clays appear to be uncommon in submarine environments (Keller, et al., 1979; Kraft, et al., 1979; Busch and Keller, 1981); however, the presence of organic material appears to increase the sensitivity of some marine muds (Torrance, 1983; Busch and Keller, 1981). Analyses of mudstones from the Pacific Rim melange indicate relatively low organic carbon contents (< 0.92% by dry wt.--Brandon, unpublished data), ruling out this possibility.

The third situation provides the most likely explanation for pervasive mass-movement. Earthquakes are commonly cited as a cause for submarine slope failure (Field, et al., 1982; see Schwarz, 1982 for extensive bibliography). These failures are largely due to high transient pore pressures which develop during long periods of ground shaking (Seed, 1968, 1976; Seed and Idriss, 1971). The actual type of ground failure depends on the type of sediment and the gradient of the slope. Slope failures usually occur as coherent slides, or as flow-slides typically composed of sand (Seed, 1968; Andresen and Bjerrum, 1967). In level-ground settings, sands are commonly affected by in-situ liquefaction (e.g., Nigata earthquake-- Seed, 1976) and occasionally form clastic dikes (Figure 29 in Seed, 1968).

While there is no direct evidence of earthquake-induced failure in the Pacific Rim melanges, the obliteration of primary sedimentary structures in sandstones and the development of sedimentary injection features (e.g., Figure 8c) are indicative of liquefaction and localized high pore pressures (discussed by Lowe, 1975). Liquefaction occurs when the effective pressure[3] within a sediment drops to zero due to an increase in pore pressure (see Castro, 1975 and Seed, 1976 for more extensive discussion of definition). Under these conditions, a non-cohesive granular aggregate cannot support any shear stress, and therefore behaves like a liquid.

A variety of situations can cause liquefaction, but only earthquakes appear to be capable of affecting large volumes of sediment. Seed (1968) has shown that during large earthquakes (with magnitudes approximately greater than 7.5), liquefaction occurs in sediments as deep as 15 m below the surface. High pore-pressures and local liquefaction can also result from the rapid imposition of a static load, such as the deposition of a thick bed of sand (Lowe, 1975, 1976; static liquefaction of Allen, 1982). However, for sediments beneath this load, effective pressure cannot decrease by more that half of its initial value (Schofield and Wroth, 1968; sensitive clays are probably an exception to this generalization). As a result, near-zero effective pressures are restricted to a thin zone beneath the load where effective pressures were already low. Liquefaction could also occur

[3] Pressure refers to mean stress; effective pressure is the total pressure minus the pore fluid pressure (Lambe and Whitman, 1978).

in areas where biogenic decomposition or metamorphic devolatilization create high fluid pressures (Hedberg, 1974; Rieke and Chilingarian, 1974). These processes are unlikely in the Pacific Rim melanges because of the low organic content of the mudstones, and the presence of an igneous basement directly beneath the melanges. With these other possibilities excluded, liquefaction and sedimentary injection features in the melanges are best explained by high transient pore pressures generated during seismic groundshaking. Before discussing the deformational fabric of the melange, it is important to consider why earthquakes have such a pronounced effect on saturated sediments.

FACTORS CONTROLLING LIQUEFACTION FAILURE

Experimental studies have demonstrated that cyclic oscillation of a load in a fashion simulating seismic ground motion can cause high pore pressures to develop, especially in comparison with those developed during normal static loading (Seed, 1976; Wood, 1982; Sangrey, et al., 1978, Castro, 1975; Carter, et al., 1982). During undrained cyclic loading, excess pore pressures are generated in a wide variety of sediments and under a range of consolidation conditions (e.g., Castro and Poulos, 1977; Wood, 1982). However, normally consolidated[4] sediments with low elastic compressibilities--such as, loose sands) develop the highest pore pressures and are the most prone to liquefaction.

Figure 15 (from Sangrey, et al., 1978; and Egan and Sangrey, 1978) shows the response of a variety of normally consolidated sediments to undrained cyclic loading. Sands have lower elastic compressibilities than clays and, as shown, tend to be more strongly affected. Cyclic shear stresses must exceed a certain critical level, which Sangrey, et al. (1978) call the critical level of repeat loading, before a sediment will develop high pore

4 As used here, the term normally consolidated also includes underconsolidated sediments. Sediments with high excess pore pressures are underconsolidated with respect to total stress conditions, but they would probably be considered normally consolidated with respect to effective stress conditions.

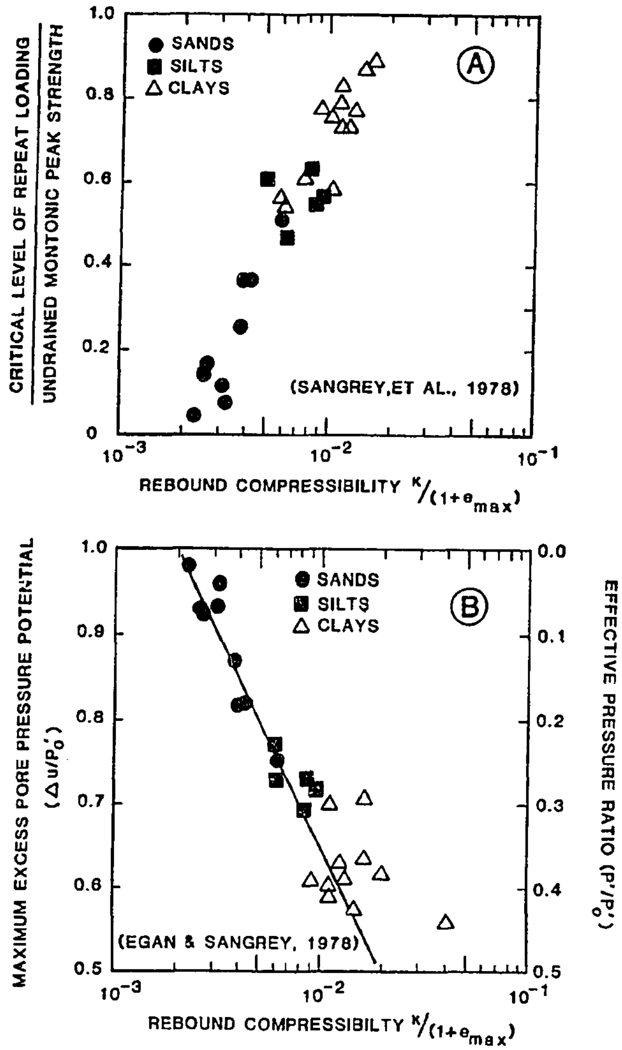

Figure 15. The effect of elastic compressibility on the behavior of saturated sediment during undrained cyclic loading (from Sangrey, et al., 1978 and Egan and Sangrey, 1978). Rebound compressibility is a function of the elastic rebound index (κ) and maximum void ratio for the sediment (e_{max} = liquid limit for clays and minimum relative density for sands).

pressures necessary for liquefaction. In Figure 15a, this critical level is expressed as a ratio with respect to the normal undrained strength of the sediment. As shown, the onset of liquefaction deformation can be induced in sands by relatively low cyclic shear stresses, only 20% of their normal undrained strength, whereas clays require much larger cyclic shear stresses to cause the same behavior.

Figure 15b shows the maximum pore-pressure potential during cyclic loading, expressed as a ratio of the maximum change in pore pressure (Δu) over the initial effective pressure (P'_o). The resulting change in effective pressure (P') is shown on the right scale. Pore-pressure potential clearly increases with decreasing elastic compressibility. Sands are more prone to liquefaction because they have maximum pore-pressure potentials approaching one. As discussed above, during undrained static loading of normally consolidated sediments, the effective pressure typically does not decrease by more than half of its initial value (i.e., $P'/P'_o > 0.5$; Schofield and Wroth, 1968). Figure 15a shows that cyclic deformation causes a much larger reduction in effective pressure for all normally consolidated sediments including clays.

While these experimental studies have identified the pore-pressure response of sediments during cyclic loading, other factors are necessary for liquefaction to occur in the field (Seed and Idriss, 1971; Seed, 1976). Most important is the maintenance of high pore-pressures during the earthquake. For instance, very fine sands are typically most susceptible to liquefaction because they combine low permeability with high pore-pressure potential. Another factor that favors liquefaction is a setting with low initial shear stresses, such as sediments in a level-ground setting (Seed, 1976, p. 3). During cyclic loading, sediments in slope settings display smaller changes in pore pressure (Egan and Sangrey, 1978), and also should tend to fail by shear failure before liquefaction can occur. Other factors that facilitate liquefaction include longer duration and greater intensity of ground shaking, which are in part dependent on earthquake magnitude and proximity to the epicenter (Seed, 1976).

ORIGIN OF MELANGE STRUCTURE

At this point it is possible to consider in more detail the origin of structures within the melange. The structural styles of Unit 2 and 1B suggest that shear failure and extensive sliding were the primary means of mass transport. While there is evidence of local liquefaction, sedimentary structures and bedding features are usually well preserved. Thick sections of overturned strata suggest long transport distances during sliding and the presence of at least a small slope gradient. The extensive involvement of basinal strata might be due to retrogressive enlargement of one or more submarine slides. In a retrogressive slide, the headwall scarp keeps moving rearward so that the size of the slide increases over a period of time. This process can happen slowly over a period of years or quickly as it did in the submarine slide at Valdez, during the 1964 Alaska earthquake (Seed, 1968).

The origin of structures within Unit 1A is more problematic. The consistent planar geometry of the unit argues against an origin by rotational slumping and sliding, or by remobilized debris flows. All of the sandstones in this unit appear to have been thoroughly liquefied and remobilized so that they now lack any evidence of primary sedimentary structures. The low permeability of the surrounding mud must certainly have enhanced the tendency for these sands to have liquefied. The presence of small sandstone dikes (e.g., Figure 8c) indicates that large pore-pressure gradients were locally developed between the sand and mud, directly analogous to the pore pressure gradients used to propagate tensile fractures during hydrofracture experiments (Lockner and Byerlee, 1977). As discussed above, sands have a greater pore-pressure potential during cyclic loading which would allow them to rapidly develop higher pore pressures than the surrounding muds. Furthermore, the chert was probably just as prone to liquefaction as the sand, because prior to lithification, it was a fine-grained radiolarian sand.

In contrast to the other melanges, Unit 1A probably formed in a level-ground setting. There is little evidence of non-coaxial deformation or brittle shear surfaces that would be expected to form during down-slope movement. Furthermore, the extensive amount of liquefaction indicates a setting with low initial shear stresses, typical of a level-ground setting (Seed, 1976). The main problem with this interpretation is that pinch-and-swell structures in the melange appear to indicate fairly large extensional strains in all directions parallel to layering (Figure 16a). Cowan (1982b) was first to call attention to this unusual structural style. Based on his study of a melange in the Franciscan complex, he suggested that axial-symmetric layer-parallel extension occurred during lateral spreading of an unconfined lobate mass of muddy sediments.

There are indications that pinch-and-swell structure in the Unit 1A melange might not have formed by layer-parallel extension. The alternative is that the boudin-shapes formed by flowage during liquefaction. In the extreme, this flowage might result in what I call <u>non-extensional boudinage</u> (Figure 16b) where a layer contracts and swells into boudin-like shapes, but without any layer-parallel extension. In proposing this term, I am attempting to distinguish this idealized situation from true boudinage which involves layer-parallel extension (Ramsay, 1967). The following features are offered as evidence that the boudin-like structures in Unit 1A have formed by a non-extensional process:

(1) If the boudins formed by layer-parallel extension then apparently there are abrupt changes and anomalously wide variations in the amount of extensional strain. For instance, an

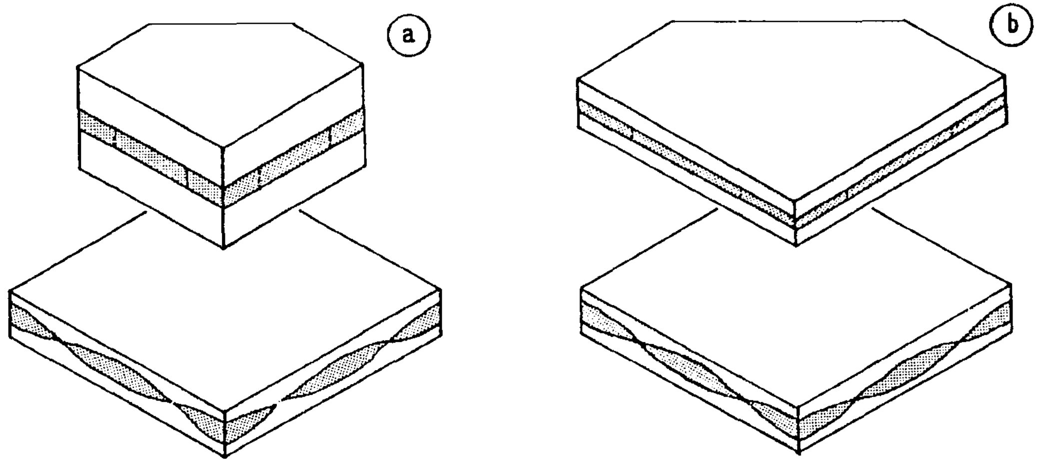

Figure 16. Two Processes that can produce boudin-like structures, such as those observed in Unit 1A. Figure 16a shows a typical example of extensional boudinage; note however, that extension occurs in all directions parallel to layering. Non-extensional boudingae, shown in Figure 16b, represents an alternative possibility. In this case, "boudinage" occurs by lateral flowage and thickening of the sand layer, without any layer-parallel extension. Note that unlike these idealized examples, boudin-like structures in Unit 1A are highly irregular in shape and in spacing.

undeformed tabular bed of sandstone or chert commonly occurs directly adjacent to a horizon where chert and sandstone are extensively "boudinaged" (e.g., see Figure 8a).
(2) Spheroidal boudins tend to be more widely separated than ellipsoidal boudins which suggests that apparent extension is controlled by the amount of thickening of individual boudins.
(3) Unlike true boudinage (Ramsay, 1967), the boudin-like shapes in Unit 1A are very irregular in shape, in size and in spacing (e.g., see figures 8 and 9). Theoretical analyses of the necking instability in true boudinage indicates that the boudins produced by this process should be relatively regular in shape and in spacing (see Smith, 1977); this conclusion is in accord with natural occurrences of true boudinage (Ramsay, 1967).
(4) Irregular bulbous protrusions are present on the upper and lower sides of some sandstone boudins (e.g., Figure 8d) and provide at least some direct evidence of thickening. Cowan (1982b) has noted similar features associated with pinch-and-swell structures in Franciscan melange.

The boudins in Unit 1A bear some resemblance to sedimentary load structures, such as ball-and-pillow structure (Allen, 1982). However, unlike load structures, the boudins appear to have grown in a relatively symmetric fashion and show no evidence of having sunk downward into the underlying mud (cf. Allen, 1982, p. 360). Furthermore, chert load structures would be unexpected because siliceous sediments typically have lower densities than clay-rich muds (Hamilton, 1976).

While these relationships do not prove a non-extensional origin for the boudin-like structures in Unit 1A, they do argue strongly against an origin by conventional boudinage. It is not clear how non-extensional boudinage occurs, although in the case of Unit 1A, the liquefaction phenomenon appears to be involved. The fact that these boudin-like shapes have formed exclusively by ductile flowage, with no evidence of tensile or shear failure, supports this contention. Experimental studies indicate the liquefaction process is very unstable (that is, "imperfection sensitive"; see Wood, 1982). As a result, a sand layer apparently does not liquefy all at once; small irregularities such as changes in the thickness of a bed or variations in porosity will causes certain regions of a sand layer to liquefy first. Seed (1968) used a finite-element model to determine how small lenses and layers of sand interbedded in mud would respond to progressive liquefaction. According to his study, regions that liquefy first tend to grow laterally because the liquefied region tends to increase cyclic shear stress in the adjacent unliquefied sand. Seed's (1968) analysis was mostly concerned with the stress distribution in the liquefying layer and did not consider how the layer deforms.

TECTONIC SETTING AND REGIONAL IMPLICATIONS

TECTONIC SETTING

The Pacific Rim melanges appear to record the Early Cretaceous formation (135 Ma) of a structurally controlled basin. A stage in the evolution of this basin is schematically illustrated in Figure 17, and represents the time of formation for Units 1A and 1B, which are coeval units (Figure 4). This interpretation is supported by the following observations: (1) The unconformity beneath the Lower Cretaceous melanges, together with the presence of rounded clasts of Ucluth Volcanics in pebbly mudstone of Unit 1B, indicates that the initiation of the basin was associated with the regional subsidence of the Ucluth Volcanics. (2) The presence of large diorite slabs in Unit 1A indicates the local presence of submarine fault scarps underlain by Ucluth Volcanics. (3) The difference in lithofacies between coeval units--mudstone and ribbon chert in Unit 1A, and turbidite and mudstone in Unit 1B--suggest a morphologically complex setting, perhaps dissected by large faults. (4) The indirect evidence for seismically induced liquefaction suggests a seismically active setting. For these reasons, the inception of deposition and melange formation are envisioned to be the result of large dip-slip displacements on basin-margin faults. Naylor (1982) has suggested a similar tectonic setting for the formation of an olistostromal melange in the northern Apennines. These large normal faults caused subsidence of the Ucluth unit, resulted in large submarine scarps of basement rock, and probably disrupted sediment transport patterns resulting in initial deposition of mud-rich facies. Contorted strata of Unit 1B were derived by retrogressive slumping of a turbidite fan sequence located upslope. Unit 1A was located in a more "distal" setting which was dominated by deposition of mud, chert and minor sand. Unlike Unit

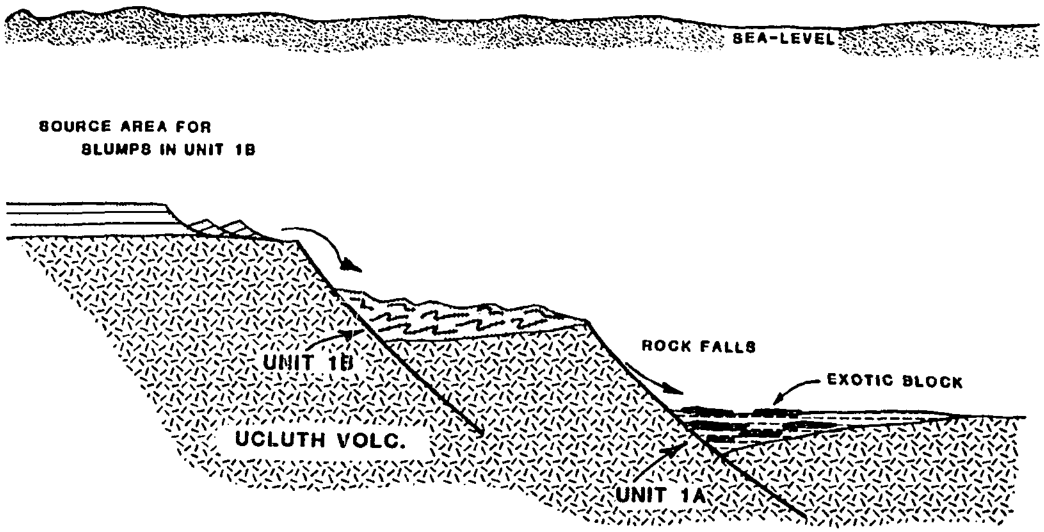

Figure 17. A schematic cross-section depicting an early stage in the evolution of the Pacific Rim melanges. Melange formation began with the development of a structurally controlled basin. Initially, basin-margin faults tended to isolate the melanges from coarse clastic sedimentation. Contorted strata of Unit 1B were derived by retrogressive slumping of a turbidite fan sequence located up-slope. Unit 1A was located in a more "distal" setting that was dominated by deposition of mud, chert and subordinate sand. Rockfalls originating from local fault scarps introduced exotic blocks of Ucluth Volcanics into Unit 1A.

1B the disruption of this unit is envisioned to have occurred by in-situ liquefaction; however, exotic blocks were introduced by locally derived rock falls. A later stage, not shown in Figure 17, involves the transition into a more widespread, sand-rich melange, Unit 2. This transition is envisioned to be the result of: (1) an increase in the proportion of sand-rich facies in the source area for the submarine slumps, and (2) a gradual "progradation" of mass-movement deposits across this originally morphologically complex margin.

Basin formation may have occurred in a transform-dominated setting similar to the southern California Boarderlands (Gorhine and Edwards, 1959; Field and Edwards, 1980), or in a rift-dominated setting related to intra-arc spreading (see Karig, 1971). Both settings include basin margin faults with large dip-slip offsets, relatively shallow basin floors, and subaerially exposed basement rock. It is difficult to distinguish between these setting because of the allochthonous nature of the Pacific Rim Complex, and the resulting uncertainties about its surrounding paleotectonic setting during the Early Cretaceous.

An alternative interpretation might propose that these exotic blocks and transported strata were derived from the front of large thrust sheets. A similar interpretation is proposed by Page and Suppe (1981) for the Pliocene Lichi melange of eastern Taiwan. In this case, the melange formed during an arc-continent collision. There are two important differences between the Lichi and Pacific Rim melanges. These differences indicate that the Pacific Rim melanges were not formed in a collisional setting. (1) The Lichi melange overlies a deeper water sedimentary sequence (about 2000 m water depth--Page and Suppe, 1981) and is overlain by fluvial strata. This sequence records the gradual emergence of the Taiwan forearc as it collided with the China continental shelf. In contrast, the Pacific Rim melanges appear to be associated with the subsidence of the underlying Ucluth basement. (2) For the

Lichi melange, the presence of large thrust sheets, with older-over-younger relationships provides a clear record of the collisional process. In contrast, major thrust faults have not been recognized in the Pacific Rim area. Furthermore, there is no evidence of major thrust faulting in the Pacific Northwest until the mid-Cretaceous (as summarized in Brandon and Cowan, 1983). This younger thrusting event probably did affect the Pacific Rim rocks (discussed below), but it clearly post-dated the formation of the Pacific Rim melanges by about 35 My.

REGIONAL TECTONIC IMPLICATIONS

The Pacific Rim Complex was probably originally coextensive with other similar Upper Jurassic-Lower Cretaceous units exposed on southern Vancouver Island (Figure 1; Pandora Peak unit--Rusmore, 1982; rocks of Gonzales Bay--Muller, 1980), and in the San Juan Islands (Constitution Formation and Lopez Complex--Brandon, et al., 1983, Brandon, 1980). Cowan and Brandon (1981) have collectively referred to these units, including the Pacific Rim Complex, as the "Western Facies" of Upper Mesozoic rocks exposed in the Pacific Northwest. They consist of chaotic assemblages of mudstone, sandstone, chert and green tuff with a variety of exotic blocks. The Constitution Formation bears the closest resemblance to the Pacific Rim Complex. The lowest two members of the Constitution Formation are probably correlative with Units 1A and 2 and consist of (1) mudstone and chert melange with exotic blocks of Permo-Triassic greenschist and Triassic limestone, overlain by (2) a thick sequence of massive sandstone (Brandon, 1980; Brandon, et al., 1983).

In addition to stratigraphic similarities, all of the "Western Facies" rocks, including the Pacific Rim Complex, have experienced a very distinctive high pressure-very low temperature metamorphism characterized by the assemblage: lawsonite + quartz $\pm$ prehnite (Brandon, 1982; Glassely, et al., 1976; Vance, 1968). Although aragonite is sporatically present in other "Western

Facies" rocks (Vance, 1968), it has not been observed in the Pacific Rim Complex. This metamorphic assemblage is apparently unique to the Pacific Northwest. Brandon (1980, 1982) was able to show that metamorphism in the San Juan Islands occurred as a direct result of rapid structural loading during the emplacement of a thick thrust sequence. Stratigraphic constraints indicate that San Juan thrusting occurred during a very short-lived mid-Cretaceous event, between 97 and 83 Ma (Brandon, 1982). Furthermore, cobbles of metamorphosed Constitution sandstone are present in Upper Cretaceous (lower Campanian) strata of the Nanaimo Group (shown in black in Figure 1), and represent the earliest direct tie between the "Western Facies" and the Wrangellia terrane (Brandon, 1982).

My work in the Pacific Rim area indicates that prehnite-lawsonite assemblages are widespread in the Pacific Rim Complex and are not present in adjacent rocks of the Wrangellia terrane to the east. In contrast to the San Juan Islands, there is no direct evidence of thrust sheets that might have once overlain the Pacific Rim Complex. However, the presence of lawsonite + quartz indicates depths of metamorphism and structural burial in excess of 11 km (Liou, 1976). These relations suggest that the Pacific Rim Complex was also involved in San Juan thrusting and metamorphism, and was subsequently displaced northward to its present position on western Vancouver Island.

As shown in Figure 18, displacement of the Pacific Rim Complex represents the first of two events that have truncated the west side of Vancouver Island. Age dates and geochemistry indicate that the Tertiary volcanic and plutonic rocks in the Pacific Rim area are part of a suite of intermediate to silicic calc-alkaline rocks, erupted and intruded during Late Paleocene to Early Eocene time (age dates summarized in Figure 2; geochemistry from Carson, 1973 and Brandon, unpublished data). This volcanic-plutonic suite

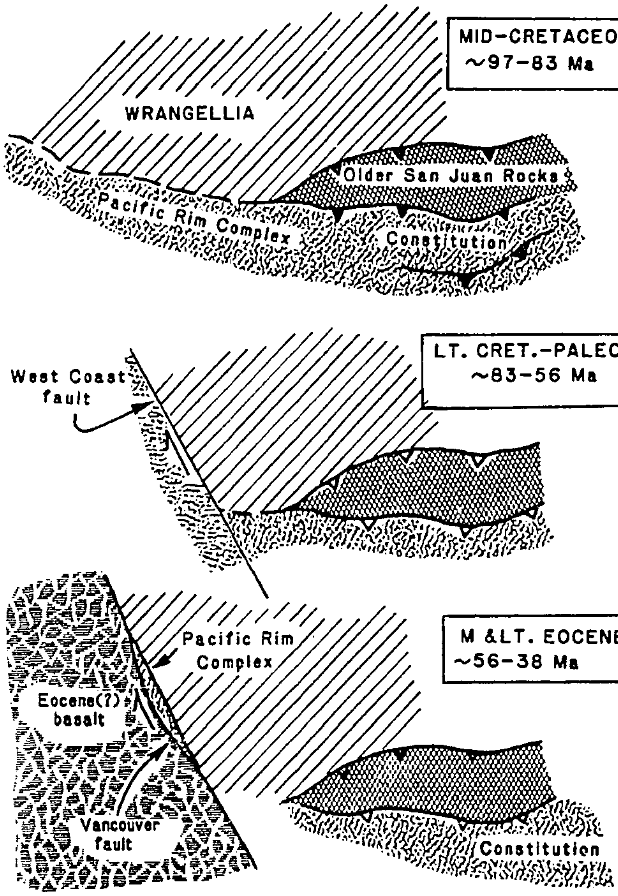

Figure 18. A schematic model for the offset of the Pacific Rim Complex and the truncation of Vancouver Island. In this model, the Pacific Rim is shown as part of the mid-Cretaceous San Juan thrust system. During the Late Cretaceous or Paleocene, the Pacific Rim Complex was displaced northward along the West Coast fault to its present position on western Vancouver Island. Subsequent displacement on another fault, the Vancouver fault, truncated the west side of the Pacific Rim; a thick sequence of Eocene(?) basalt presently lies to the west.

occurs on both sides of the West Coast fault (Figure 2), and indicates major northward displacement of the Pacific Rim Complex occurred prior to the Early Eocene.

The Pacific Rim is bounded on its west side by another major transcurrent fault. In the offshore region to the west of the Pacific Rim area, drilling and exploration by Shell Canada has identified a regionally extensive sequence of Eocene(?) basalts (Shouldice, 1971). MacLeod, et al. (1977) have correlated these rocks with Eocene tholeiitic basalts of the Crescent and Metchosin Formations, located to the southeast (Figure 1). Geochemical analyses and petrographic study of drilling samples provided by Shell Canada confirm this correlation (Brandon, unpublished data). Aeromagnetic maps in this area (Shell Canada, unpublished data) suggest a steep, northwest-trending contact between Eocene(?) basalts and rocks of the Pacific Rim area. The dissimilarity between coeval volcanic rocks--tholeiitic basalt to the west and calc-alkaline dacite to the east--indicates that this contact is a major transcurrent fault, named the Vancouver fault by Brandon and Cowan (1983). Major movement on this fault must post-date Early Eocene volcanism and pre-date Late Eocene and younger strata of the Tofino Basin which overlie both volcanic units (Figure 1; shown as the Carmanah Group in Figure 2).

A number of papers have suggest an original more southerly location for portions of southern Alaska (Stone and Packer, 1979; Cowan, 1982a; Moore, et al., 1983; Stevenson, et al., 1983; Bruns, 1983). For instance, Cowan (1982a) has argued that rocks presently exposed on Baranof Island, southeast Alaska, were offset by Eocene transcurrent faulting from the Leech River Schist on southern Vancouver Island. However, more typically the evidence for offset is based on paleomagnetic or faunal data and only gives a rough indication of the original paleolatitude (within 500 km at best). My work in the Pacific Rim area indicates that western Vancouver Island preserves a record of this northward-directed traffic and probably represents an important source area for offset terranes in southern Alaska.

CONCLUSIONS FOR PART I

My major conclusions are as follows:

(1) The Pacific Rim Complex is underlain by a basement comprising Triassic arc volcanic rocks which are not correlative with coeval rocks of Vancouver Island.

(2) Melanges in the Complex represent a stratigraphic accumulation of various mass-movement deposits. Frequent large earthquakes were probably responsible for the extensive amount of soft-sediment deformation.

(3) The present position of the allochthonous Pacific Rim Complex is wholly an artifact of younger transcurrent displacements.

PART II

DEFORMATION OF SEDIMENTS AT SUBDUCTION ZONES:

AN APPLICATION OF CRITICAL STATE SOIL MECHANICS

INTRODUCTION FOR PART II

Since the recognition of plate tectonics, much attention has been focused on ancient and modern convergent margins in order to resolve a record of plate interactions. In many modern convergent margins, young trench-fill sediments are continually deposited across the surface trace of the active subduction boundary (Figure 19), and invariably become incorporated and deformed within the subduction zone. The popular subduction accretion model (Beck, 1972; Karig, 1974; Seely, et al., 1974) predicts that trench slopes are underlain by structural complexes that have grown by frontal accretion of imbricate thrust slices derived from sediments on the down-going plate. This orderly and sequential process is analogous to frontal imbrication in on-land thrust belts (Boyer and Elliott, 1982) and should provide a fairly complete record of subduction interaction, especially in trench settings where the down-going plate has a thick sedimentary cover.

Thrust imbrication can be documented in the frontal regions of several modern subduction systems (northern segment of the Middle America trench -- Moore, et al., 1982; Sumatra trench -- Karig, et al., 1980; Barbados Ridge complex -- Moore, Biju-Duval, et al., 1982; Nankai trough -- Aoki, et al., 1983)); but there is no ready assurance that deformation within the deeper portions of convergent margins is at all like on-land thrust belts. To begin with, subduction rates are typically one to two orders of magnitude faster than the rates of overthrusting reported for on-land thrust systems (Gretener, 1972, p. 592). Furthermore, subduction-zone deformation typically involves unlithified water-saturated sediments. Seismic profiles across some modern accretionary wedges (Westbrook, et al., 1982; Aoki, et al., 1983) demonstrate that as much as 50% of the sediment cover on the down-going plate is not accreted at the front of the wedge, but instead is carried some 10's of kilometers arcward beneath the wedge.

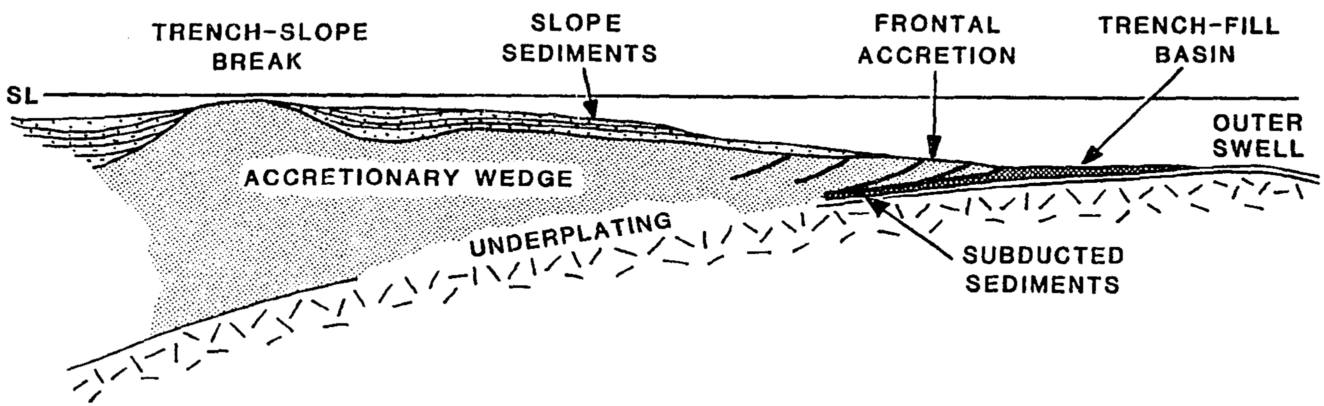

Figure 19. Cross-section of a typical accretionary wedge.

High excess pore fluid pressures are bound to develop in these subducted sediments (Westbrook, et al., 1982; Von Huene and Lee, 1983).

As a result, some geologists (Bachman, 1978; Byrne, 1982; Cloos, 1982; Moore and Karig, 1979) suggest that the subduction-zone setting is probably conducive to the development of unusual deformational styles, such as those found in chaotic melanges. This possibility is in accord with the common occurrence of melanges in ancient, sediment-rich subduction complexes (Cowan, in press). In the subduction-zone interpretation, melanges are thought to form when unlithified sediments move beneath the accretionary wedge and are deformed within a subduction-related shear zone. Judging from the exposed dimensions of these melange units, this shear zone would be on the order of 100's of meters thick; Cloos (1982) suggests that this shear zone might be several kilometers thick, and therefore involve large parts of the accretionary wedge.

Whether or not these interpretations are correct, they pose an important question: What factors control the deformational behavior of unlithified sediments within the subduction zone setting? Before considering this question, let us first examine the deformational conditions and strains expected within a typical subduction zone. Deformation in this setting can be represented by two idealized, end-member situations (Figure 20). As sediments approach the accretionary wedge, they first begin to deform in a fashion approximating coaxial horizontal shortening. Those sediments subducted beneath the wedge are confined to an actively moving shear zone, and therefore must deform in a non-coaxial manner, probably best approximated by simple shear. The expected range of deformational behavior within this zone can be characterized in a simple fashion by the three structural styles shown in Figure 21. These styles consist of: (1) a wide ductile shear zone composed of cohesively flowing sediments; (2) a wide zone consisting of a network of closely spaced faults or slip surfaces, which in the case of muds may begin to resemble a scaly fabric; and (3) widely spaced faults, perhaps with a geometry similar

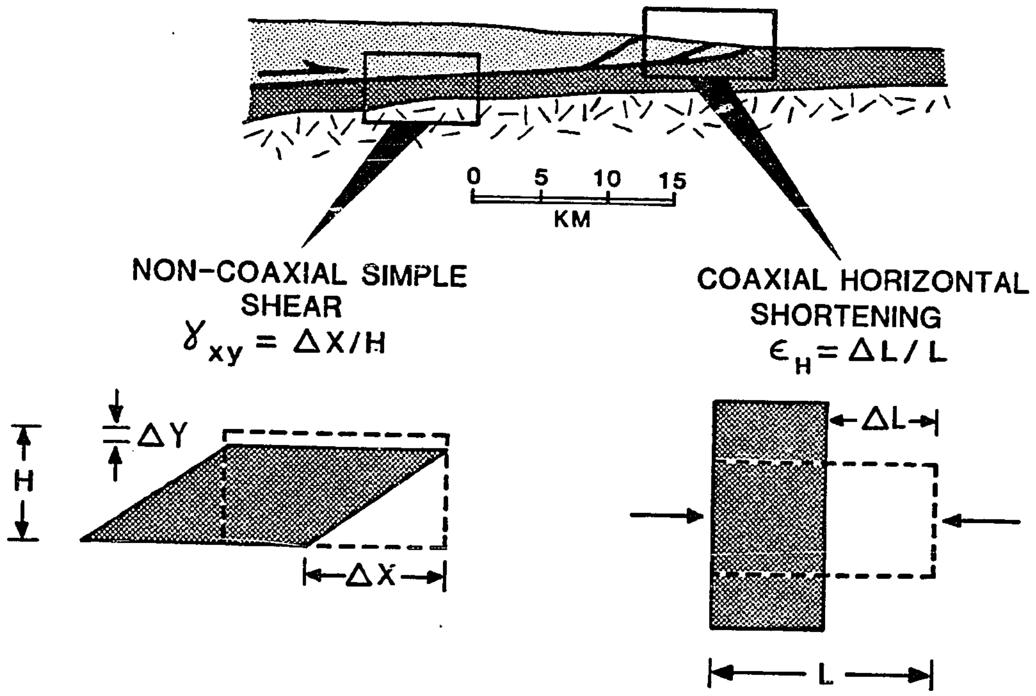

Figure 20. Two idealized situations for deformation in a subduction zone setting.

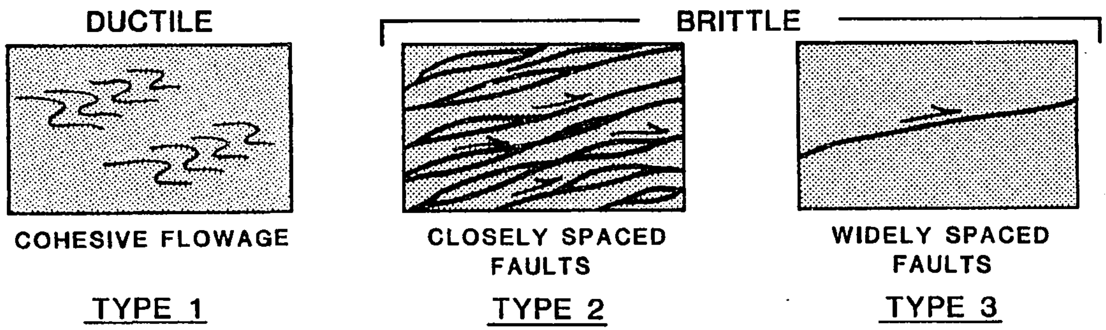

Figure 21. Three general structural styles which characterize the expected range of deformational behavior within a subduction zone.

to on-land thrust belts. The first structural style is considered ductile because the sediment deforms in a continuous fashion at scales large than individual grains. The last two structural styles are considered brittle because the bulk of the deformation is accommodated along discrete slip surfaces. Laboratory deformation of water-saturated clays and sands indicates that failure typically occurs after relatively small strains (Table 2), especially when compared with the geologic situation. For instance, sediment deformed under simple shear conditions generally fails at shear strains less than 25%. However, because the displacements across the zone are large in comparison with the thickness of the zone, sediments in a subduction shear zone such as the one depicted on the left side of Figure 20, are subject to much greater shear strains, on the order of 100's and 1000's of percent. Unfortunately, it is impossible to experimentally deform sediments to the large strains and large displacements typical of the subduction zone setting. Furthermore, when sediments reach their failure condition, continued deformation tends to be unstable and is highly influenced by the artificial nature of the testing apparatus (see Wood, 1982).

The approach used in this paper is to examine the generalized constitutive behavior of water-saturated sediments. The main premise is that the predominance of any one of the above structural styles is determined primarily by this constitutive behavior. In particular, there are three aspects of this behavior to be considered: (1) What factors allow a deforming sediment to flow in a stable and cohesive fashion, as opposed to failing in an unstable fashion with the development of localized slip surfaces? (2) How much ductile strain occurs before failure? (3) When failure occurs, how much weaker is the failed zone with respect to the surrounding unfailed sediment? This last question is particularly important because a sediment may fail (i.e., reach its peak strength), but in order for continued deformation to be isolated along a discrete slip surface, failure must involve a significant loss of strength.

TABLE 2. Typical strains at failure for water-saturated clays and sands.

SEDIMENT TYPE AND CONSOLIDATION STATE*	TRIAXIAL COMPRESSION† AXIAL STRAIN AT FAILURE ε_1 (%)	DEVIATORIC STRESS AT FAILURE $(\sigma_1-\sigma_3)$ (kPa)
DRAINED		
Loose clay	~23%	255
Loose sand (45.6%)	~20%	520
Dense clay	8%	50
Dense sand (39%)	5%	725
UNDRAINED		
Loose clay	17%	~115
Loose sand (45.8%)	14%	115
Dense clay	27%	~95
Dense sand (43.0%)	33%	~1210

SEDIMENT TYPE AND CONSOLIDATION STATE*	SIMPLE SHEAR§ SHEAR STRAIN AT FAILURE γ_{xy} (%)	DEVIATORIC STRESS AT FAILURE $(\sigma_1-\sigma_3)$ (kPa)
DRAINED		
Loose kaolin clay	25%	75-145
Loose sand (46.0%)	~15%	65
Dense sand (38.5%)	8%	85

* Initial porosity shown where available.

† Compiled from Bishop and Henkel (1962), p. 110, 115, 116, 123, 128.

§ Sands were tested by Fukushima and Tatsuoka (1982) using a torsional simple shear apparatus. Kaolin clay was tested by A. Thurairajah using a Cambridge simple shear device (cited in Roscoe and Burland, 1968, p. 599).

This paper is developed in three parts. In the first part, a well established constitutive model is used to explain the generalized behavior of deforming sediment. This model establishes a firm basis with which to judge the relative effects of strength, porosity, state-of-stress and pore pressure. The second part examines the loading conditions present at a subduction zone, and the deformational behavior that might be expected in subducted and accreted sediments. The last part of the paper explores some of the implications of this analysis for structural styles in accretionary wedges. Two specific problems are considered: (1) the development of scaly clays and thrust faults in the region of the Barbados drilling transect (Leg 78A of the Deep Sea Drilling Project [DSDP]--Moore, Biju-Duval, et al., 1982), and (2) structural styles that might be associated with underplating, that is, accretion to the base of the wedge.

SEDIMENT DEFORMATION AS DESCRIBED BY CRITICAL STATE SOIL MECHANICS

There has been a strong motivation in soil mechanics to provide a more rational basis for soil testing and engineering design. As a consequence, a number of sophisticated constitutive models have been developed over the past 25 years (see review by Ko and Sture, 1981). However, a series of models developed during the 1960's by K. H. Roscoe and others at Cambridge University (Schofield and Wroth, 1968; Roscoe and Burland, 1968) still provide the simplest and most concise description of deformational behavior of water-saturated granular materials. The Cambridge models were initially developed to describe stress-strain behavior of loosely consolidated clays deformed under triaxial conditions. These models, however, have been successfully used to predict the general deformational behavior of sand and clay over a range of initial consolidation conditions (Roscoe, 1970, 1971; Atkinson and Bransby, 1978). Futhermore, Roscoe and Burland (1968) show that one of the Cambridge models is applicable to more generalized stress-strain conditions, such as plane strain and simple shear.

The Cambridge models are based on the concepts of critical state soil mechanics (Schofield and Wroth, 1968) which view sediments as elastic-plastic materials. The term plastic is used in the generic sense to refer to the permanent, non-recoverable component of deformation, as opposed to the elastic component which is fully recoverable when the material is unloaded. Ideally plastic materials are considered to have a constant yield strength; however, the yield strength for a deforming sediment changes depending on the current state of the sediment, defined by its state-of-stress and porosity. A material with these properties could be more formally referred to as a pressure-sensitive, strain-hardening elastic-plastic material. As might be expected, the stress-strain behavior of such a material is more complicated than that of an ideally plastic material.

The Cambridge models are ideally suited for the problem considered here, for the following reasons:

(1) The models are relatively simple in form.

(2) The models only require five material constants which are easily measured using conventional triaxial tests. These constants appear to be invariant properties of the sediment, and, therefore, allow the models to be used to simulate a wide range of deformational conditions.

(3) The models provide a conceptual framework for sediment deformation that manages to tie together, in a coherent fashion, a number of observations and relationships that otherwise appear to be unrelated. This last feature is an important one, because it allows us to treat problems of sediment deformation, such as the subduction zone problem, in a more confident and generalized fashion.

In this section, the Cambridge models are introduced in several steps. The first step considers how the porosity of the sediment affects its deformational behavior. This topic is used to introduce some general concepts, such as strain-hardening, strain-softening and deformational stability. The second step introduces the idea of a critical state line, which separates regions of different deformational behavior. And finally in the last step, one of the Cambridge models, called the modified Cam Clay model, is described and used to introduce the idea of plastic yield surfaces. This model is also used in a another section to examine representative examples of strain-hardening and strain-softening deformation, under drained and undrained conditions. Triaxial deformational conditions are used in these examples ($\sigma_1' > \sigma_2' = \sigma_3'$), despite the fact that the subduction zone setting is better represented as plane-strain deformation. A more rigorous presentation could be made using the plane-strain version of the modified Cam Clay model (Roscoe and Burland, 1968); however, it is quite clear that the conclusions drawn from the triaxial examples are applicable to the plane-strain situation. This point is discussed in more detail below.

DEFINITION OF VARIABLES

In the following discussion, sediments are assumed to be saturated with water, and, unless otherwise noted, all stresses are represented as effective stresses and are designated as such with a prime (σ'). Compressional stresses and shortening strains are defined as positive, in accordance with the convention in soil mechanics (Atkinson and Bransby, 1978); to be consistent, a decrease in volume corresponds to a positive volumetric strain. Note that the typical convention in geology (Ramsay, 1967) defines shortening strains and decreasing volume as negative strains. Void ratio, e, is used as the measure of relative pore volume, and is defined by:

$$e = \frac{\text{pore volume}}{\text{solid volume}} = \frac{n}{(1-n)} \tag{1}$$

where n represents fractional porosity. While porosity is probably more familiar, void ratio is preferred for sediment deformation because the changing pore volume is compared against a fixed solid volume, thereby providing a more direct measure of volumetric strain.

Figure 22 shows the layout for the triaxial compression test, which is probably more appropriately described as axially symmetric compression. The axial stress, σ_1', is the maximum compressive stress; the confining stress is provided by $\sigma_2' = \sigma_3'$. Pressure, P', is defined as the mean effective stress. In the plasticity models, large strains are typically determined by summation of small incremental strains, $\Delta\varepsilon = (-\Delta L/L)$, which results in:

$$\varepsilon = \mathrm{Ln}\,[-(L_f - L_o)/L_o] \;=\int d\varepsilon \;\doteq\; >\Sigma\Delta\varepsilon \tag{2}$$

where ε is known as the natural or logarithmic strain (Ramsay, 1967, p. 52), and L_o and L_f are the initial and final length, respectively. The shear strain increment, $d\varepsilon_s$, and the volumetric strain increment, $d\varepsilon_v$, are defined in Figure 22. A list of symbols is provided in Appendix B.

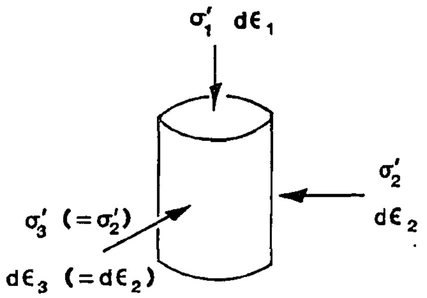

U = PORE-FLUID PRESSURE

$\sigma' = \sigma - U$

$d\epsilon = -dL/L$

TRIAXIAL COMPRESSION

STRESS

DEVIATORIC $Q' = (\sigma_1' - \sigma_3')$

PRESSURE $P' = (\sigma_1' + \sigma_2' + \sigma_3')/3$

STRAIN INCREMENTS

SHEAR $d\epsilon_s = 2/3(d\epsilon_1 - d\epsilon_3)$

VOLUME $d\epsilon_v = \frac{-de}{(1+e)} = \frac{-dV}{V}$

$$\text{VOID RATIO } (e) = \frac{\text{PORE VOLUME}}{\text{SOLID VOLUME}}$$

Figure 22. Stress and strain relationships for triaxial compression.

THE EFFECT OF VOID RATIO ON SHEAR STRENGTH

The stress-strain behavior of sediments, be it clay or sand, is significantly dependent on the current void ratio of the sediment. The schematic diagrams in Figure 23 illustrate the effect of void ratio on the shear strength of a typical sediment. In this example, pressure is held constant, and excess pore pressure is allowed to dissipate (i.e., drained conditions), so that any change in void ratio (i.e., volume strain) is due solely to changing deviatoric stress. A number of specific tests for sands and clays (Atkinson and Bransby, 1968; Vesic and Clough, 1968; Lade, 1982) indicate that these generalized relationships are, in fact, representative.

As shown in Figure 23a, the densely packed sediment is characterized by a peak in strength and can initially sustain greater deviatoric stresses in comparison with a more loosely packed sediment. With continued deformation, both the dense and loose sediment develop a constant shear strength or ultimate strength which is independent of their initial packing. As these sediments approach their ultimate strength, they also converge on a constant void ratio called the critical void ratio (Casagrande, 1936; Roscoe, et al., 1958). Within the context of critical state soil mechanics, when a sediment reaches its critical void ratio, it is considered to be at its critical state (Schofield and Wroth, 1968); further deformation at the same pressure occurs without any change in volume (Figure 23b and 23c). Therefore, the critical state, and its associated critical void ratio, represent a unique condition during constant-pressure deformation where the sediment has developed a steady-state packing arrangement and deforms at constant deviatoric stress. It is important to point out, however, that for densely packed sediments which develop localized zones of deformation, only the sediment within the failure zone reaches the critical state (Schofield and Wroth, 1968, p. 211). As a consequence, the bulk void ratio of a dense sediment at its ultimate strength is typically smaller than its critical void ratio.

Figure 23. The effect of void ratio on drained deformation at constant pressure. Dense and loose refer to the void ratio of the sediment prior to deformation.

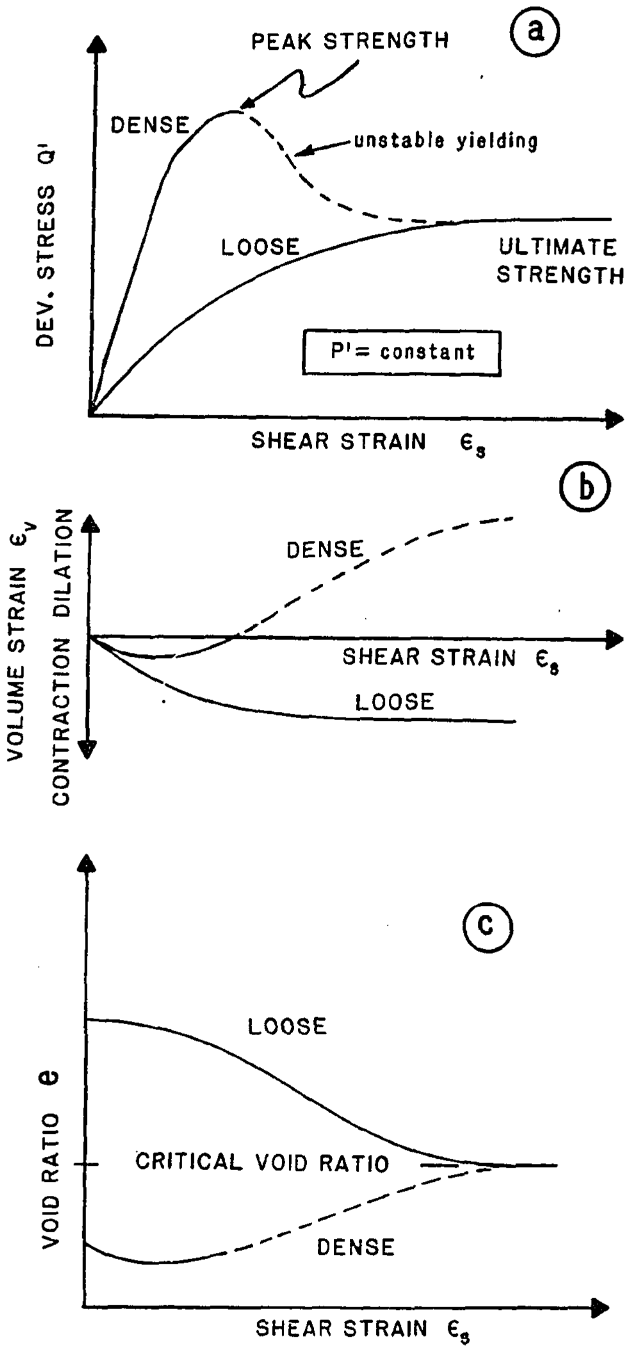
a
PEAK STRENGTH
DENSE
unstable yielding
LOOSE
ULTIMATE STRENGTH
P'= constant
DEV. STRESS Q'
SHEAR STRAIN ϵ_s
b
VOLUME STRAIN ϵ_v
CONTRACTION DILATION
DENSE
SHEAR STRAIN ϵ_s
LOOSE
c
LOOSE
VOID RATIO e
CRITICAL VOID RATIO
DENSE
SHEAR STRAIN ϵ_s

The fact that sediments at the critical state deform at a constant volume and constant shear strength, indicates that variations in shear strength are somehow related to the volumetric strain behavior of the sediment. Figure 23b and 23c illustrate typical changes in volumetric strain and void ratio during deformation. The loosely packed sediment continually decreases in volume and in void ratio until it reaches its critical void ratio. This contractive behavior is associated with a progressive increase in shear strength. In contrast, the densely packed sediment dilates or increases in volume during deformation, and after reaching an initial peak strength, is characterized by a progressive decrease in shear strength. (The relatively small, initial decrease in volume for the dense sediment in Figure 23 represents elastic volumetric strain acquired before plastic yielding begins. This is discussed in more detail below.)

STRAIN-HARDENING AND STRAIN-SOFTENING BEHAVIOR

The stability of a deforming plastic material--that is, whether it deforms in a cohesive stable fashion or ruptures in an unstable fashion--is determined by the strain-hardening or strain-softening behavior of the material (Drucker, 1966; Schofield and Wroth, 1968, p. 97). Strain-hardening or strain-softening indicates that with progressive strain, a plastic material either increases or decreases in strength. For the sediments illustrated in Figure 23, the dominant type of behavior, either stain-hardening or strain-softening, depends upon whether the current void ratio is looser or denser than the critical void ratio (Schofield and Wroth, 1968, p. 107).

How does strain-hardening and strain-softening behavior affect the deformational stability of a plastic material? Real plastic materials have internal variations in strength; therefore, weaker regions within the material will deform first. Strain-hardening promotes stable, homogeneous deformation because those initially weaker regions become stronger causing deformation to spread out and involve all of the material at a common yield stress. Hence, a loose sediment which displays strain-hardening behavior (Figure 23) should deform in a stable ductile fashion. In contrast, strain-softening is an inherently unstable mode of deformation because initial variations in strength are enhanced with continued deformation. As a consequence, strain becomes preferentially concentrated into discrete zones, which causes the material within these zones to weaken further. Strain-softening elastic-plastic materials are therefore characterized by planar zones of localized deformation. They are also prone to brittle rupture because as these localized zones weaken, they unload the surrounding material, thereby releasing elastic strain energy. This energy release can cause the formation and propagation of a discrete rupture surface within the weakened zone; this process is analogous to the propagation of a fault through a rock (Rudnicki and Rice, 1975; Palmer and Rice, 1973). Thus, for dense sediments that display strain-softening behavior, we can expect progressive deformation to culminate with brittle rupture and the formation of discrete faults. These newly formed faults will be significantly weaker than the surrounding sediment, and therefore will tend to accommodate further deformation.

It is common practice in soil mechanics to assume that failure occurs when a sediment reaches its peak strength (e.g., Bishop and Henkel, 1962). This assumption seems reasonable for dense sediments because their peak strength marks the onset of strain-softening deformation. However, for loose sediments, there is no loss-of-strength at peak strength because peak strength and ultimate strength are the same. Furthermore, experimental data indicate that loose sediments do not rupture at failure (Vesic and Clough, 1968; Atkinson and Bransby, 1978; Lade, 1982).

What does occur when a loose sediment reaches its peak strength? The peak strength of a loose sediment also coincides with its critical state. At the critical state, the sediment neither hardens nor softens with continued deformation. Without strain-softening, the elastic release required to propagate a brittle rupture surface cannot occur. Furthermore, in the absence of strain hardening, there is no mechanism to ensure stable ductile deformation of the sediment. Therefore, the deforming sediment is considered neutrally stable, and under this condition should be more highly influenced by local features, such as variations in strength. Evidence is given below which suggests that wide zones of scaly clays might develop under this neutrally stable condition. In the following discussion, these two failure conditions are distinguished by the term rupture failure, referring to strain-softening failure in dense sediments, and stable failure, referring to neutrally stable failure of loose sediments at the critical state. Lade (1982) makes a similar distinction in his discussion of failure modes for sands in triaxial tests.

At this point, it is important to emphasize that the relationships described above between deformational stability and strain-hardening and strain-softening behavior have been experimentally verified for a variety of clays and sands, and under a wide range of test conditions (see examples summarized in Schofield and Wroth, 1968; and in Atkinson and Bransby, 1978; also Vesic and Clough, 1968; Lade, 1982). Furthermore, a generalized analysis by Rudnicki and Rice (1975) of the deformational stability of pressure-sensitive, elastic-plastic materials establishes a firm theoretical basis for these concepts. It should be mentioned that Rudnicki and Rice are primarily concerned with the problem of fault rupture in rocks, but they specially note that their analysis is also applicable to sediments.

For the problem considered here, we are interested in using these concepts of deformational stability to help predict the general structural style of sediment deformation in the subduction-zone setting (Figure 21). The critical state concept represents a means towards that end, because it allows us to identify those conditions where a sediment will either strain-harden or strain-soften. In the case of constant-pressure deformation, the critical state of a specific sediment can be represented by two parameters: the ultimate strength and the critical void ratio. However, for generalized deformational conditions, the critical void ratio of a sediment changes as a function of pressure, P'. In order to introduce a generalized relationship for the critical state, we must first consider how void ratio changes with pressure during isotropic consolidation (i.e., $Q' = 0$).

VOLUMETRIC STRAIN DURING ISOTROPIC CONSOLIDATION

Isotropic consolidation refers to a special test conducted under drained conditions where all three principal stresses are maintained at equal values ($\sigma_1' = \sigma_2' = \sigma_3' = P'$), so that the sediment deforms solely by changes in pressure, P'. The advantage of this test is that it creates a situation where there is a direct relationship between pressure and volumetric strain in the absence of deviatoric stress (note that $Q' = 0$). The volumetric strain behavior of sediment during isotropic consolidation forms an important basis for the Cambridge models; three of the five material constants used in the models are derived from this test.

When sediment is isotropically consolidated for the first time, its void ratio decreases with increasing pressure, a relationship which is described by the virgin isotropic consolidation line (ICL) or λ line (Figure 24). The isotropic consolidation line forms a straight line in an e-Ln(P') diagram (Roscoe and Burland, 1968, p. 551):

$$e = e_I - \lambda \, Ln(P') \qquad (3)$$

where e_I and λ represent material constants (e_I is the void ratio when $P'=1$ kPa). Void ratio changes indicated by the isotropic consolidation line represent both the elastic and plastic components of volumetric strain. Consider the example in Figure 24; an increase in pressure from P_1' to P_2' causes a decrease in void ratio from e_a to e_b. When the pressure is reduced back to P_1', there is only a small increase in void ratio as the sample recovers the elastic component of the volumetric strain. This elastic unloading curve is called a swelling curve. When the sediment is subjected to another pressure increase, the void ratio decreases again and roughly retraces the swelling curve back to the isotropic consolidation line. This elastic

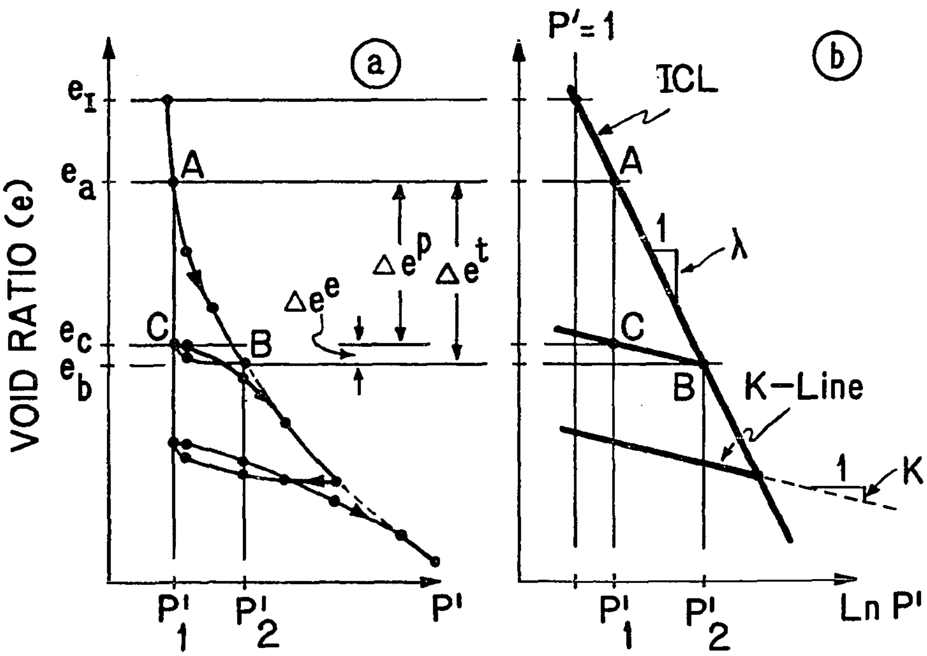

Figure 24. Deformation and volume change occurring during isotropic consolidation. Figure 24a illustrates typical changes in void ratio when a sediment is consolidated for the first time from P'_1 to P'_2, and then unloaded back to P'_1. Figure 24b shows the same relationships, but with void ratio plotted against ln (P'); the isotropic consolidation line (ICL) and the elastic K-line form straight lines in this e-Ln(P') diagram.

reloading curve is called a recompression curve. The swelling and recompression curves are represented by an average elastic curve called the K-line defined by (Schofield and Wroth, 1968, p. 72, 136):

$$e_2 = e_1 - K\ \mathrm{Ln}(P_2'/P_1') \tag{4}$$

where K is a third material constant.

Using λ and K, the following expressions can be used to determine the amount of total, plastic and elastic changes in void ratio imposed during a given change in pressure from P_1' to P_2',

$$e^t = (e_b - e_a) = -\lambda\ \mathrm{Ln}(P_2' \,/\, P_1') \tag{5}$$

$$e^e = (e_c - e_b) = -K\ \mathrm{Ln}(P_2' \,/\, P_1') \tag{6}$$

$$e^p = (e_c - e_a) = -(\lambda - K)\ \mathrm{Ln}(P_2' \,/\, P_1') \tag{7}$$

For infinitesimal increments of deformation, a volumetric strain increment, $d\epsilon_v$, is defined as (Roscoe and Burland, 1968, equation 8):

$$d\epsilon_v^p = -dV/V = -de/(1+e) \tag{8}$$

where V is the volume (the minus sign reflects the convention that volumetric strains are positive when volume decreases). Differentiating equations 5-7 with respect to pressure gives the volumetric strain increments during isotropic deformation:

$$d\epsilon_v^t = \frac{-\lambda}{(1+e)}\ \frac{dP'}{P'} \tag{9}$$

$$d\varepsilon_v^e = \frac{-K}{(1+e)} \frac{dP'}{P'} \qquad (10)$$

$$d\varepsilon_v^p = \frac{-(\lambda-K)}{(1+e)} \frac{dP'}{P'} \qquad (11)$$

These expressions are used in the Cambridge models to determine volumetric strains associated with more generalized types of deformation. In the discussion below, void ratio is frequently used as an informal measure of volumetric strain. Therefore, it is important to note that a change in void ratio (de, Δe) is proportional to a change in volumetric strain ($d\varepsilon_v$, $\Delta\varepsilon_v$) (equation 8).

THE CRITICAL STATE LINE

The critical state line (CSL) delimits those conditions under which a sediment will strain-harden or strain-soften (Figure 25). The "condition" of a sediment can be more accurately referred to as its state (Roscoe and Burland, 1968, p. 538), which is defined by the current void ratio, pressure and deviatoric stress (e, P', Q') for that sediment. Therefore, the critical state line indicates the specific values of e, P' and Q' where a plastically deforming sediment neither strain-hardens nor strain-softens. When in this state, the sediment is said to be in its critical state (Schofield and Wroth, 1968, p. 107).

In principle, we could define the critical state line by submitting a sediment to a series of triaxial tests, like the ones shown in Figure 23. The critical void ratio, ultimate strength and pressure determined in each test would represent a point on the critical state line for that sediment. These tests are best performed with the sediment initially in a state looser-than-critical, in order to ensure that the whole sample deforms in a stable, homogeneous fashion, and to avoid unstable deformation and localization associated with denser-than-critical states. This approach has been used to determine the position of the critical state line for a variety of sediments

Figure 25. The location of the critical state line (CSL) is shown as a function of void ratio e, pressure P', and deviatoric stress Q'. Sediments that are densier-than-critical dilate upon yielding and exhibit unstable strain-softening behavior, whereas sediments looser-than-critical compact upon yielding and exhibit stable strain-hardening behavior. A series of elliptical yield surfaces are also shown in Figure 25a; only one yield surface is active at a time depending upon the current void ratio and pressure. Plastic strains can only occur when the state-of-stress (P', Q') is on the current yield surface.

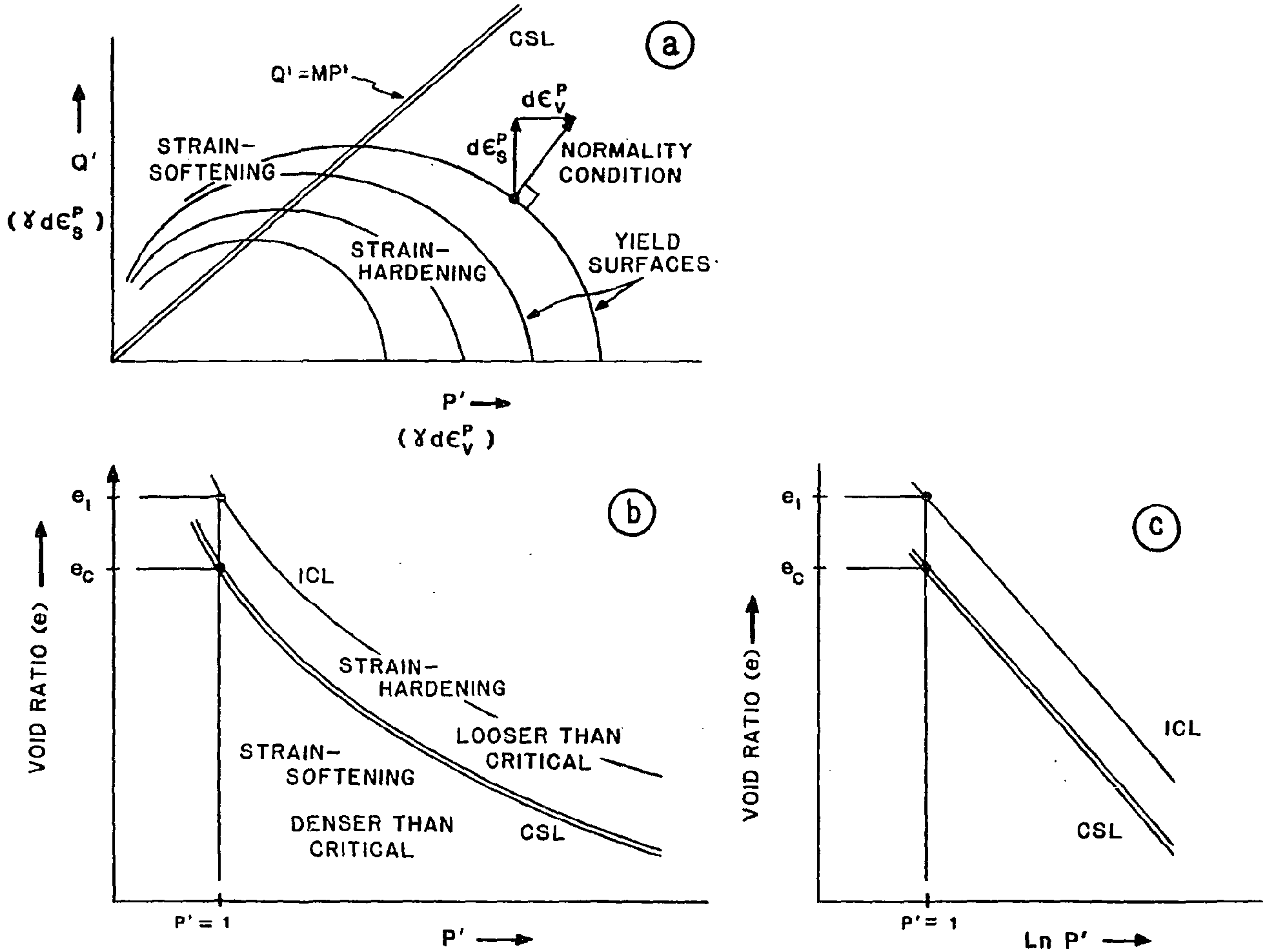
a
CSL
Q' =MP'
Q'
(γdε_s^p)
P'
(γdε_v^p)
dε_v^p
dε_s^p
NORMALITY CONDITION
STRAIN-SOFTENING
STRAIN-HARDENING
YIELD SURFACES
b
e_i
e_c
VOID RATIO (e)
ICL
STRAIN-HARDENING
LOOSER THAN CRITICAL
STRAIN-SOFTENING
DENSER THAN CRITICAL
CSL
P' = 1
P'
c
e_i
e_c
VOID RATIO (e)
ICL
CSL
P' = 1
Ln P'

(numerous examples are reviewed in Schofield and Wroth, 1968; and Atkinson and Bransby, 1978). These studies indicate that in an e-Ln(P') diagram, the critical state line lies beneath and parallel to the isotropic consolidation line (Figure 25). Therefore, e and P' for the critical state line can be defined by the following relationship (cf. equation 3) (Schofield and Wroth, 1968, p. 108):

$$e = e_C - \lambda \, Ln(P') \qquad (12)$$

where e_C is the critical void ratio at P'=1 kPa and λ is the slope of the isotropic consolidation line. For the P'-Q' diagram (Figure 25), these tests indicate that the critical state line is described by (Schofield and Wroth, 1968, p. 108):

$$Q' = M\,P' \qquad (13)$$

where M is a material constant and Q' and P' are the deviatoric stress and pressure for a sediment at its ultimate strength (i.e., critical state). The constant M is related to the more familar parameter Ø, the angle of friction, by the following relationship (Roscoe and Burland, 1968, p. 584):

$$M = [(6 \sin Ø) / (3 - \sin Ø)] \qquad (14)$$

The angle of friction used here is for triaxial compression and is referred to as the "ultimate friction angle" by Lambe and Whitman (1979, p. 144).

With these relationships, only two triaxial tests are needed to locate the critical state line: (1) An isotropic consolidation test is used to determine the material constant, λ (equation 3). (2) A drained triaxial compression test, such as the test in Figure 23, is used to determine e, P' and Q' at stable failure. These values (e, P', Q') represent a point on the critical state line, and therefore can be used with equations 12 and 13 to solve for M and e_c.

As shown in Figure 25, the critical state line separates the e-P' and P'-Q' diagrams into two regions corresponding to strain-hardening and strain-softening behavior. For instance, in the e-P' diagram, a plastically deforming sediment located above the critical state line (looser-than-critical) would strain-harden, and below the line (denser-than-critical) would strain-soften. In the P'-Q' diagram, the critical state line represents the ultimate strength of the sediment as a function of pressure. Therefore, a plastically deforming sediment located to the left of the line would strain-soften because its present strength would be greater than its ultimate strength. If instead it was located to the right of the line, the sediment would strain-harden because its ultimate strength would be greater than its present strength.

SEDIMENT PLASTICITY AND THE MODIFIED CAM CLAY MODEL

This section introduces several of the remaining features of the Cambridge models, such as plastic yield surfaces, the normality condition and stress-incremental strain relationships. These features are also used by other sediment plasticity models (see review by Ko and Sture, 1981); however, for the Cambridge models the critical state line forms the basic framework around which the various plasticity models have been constructed. In this approach, the critical state line is considered to be a line of reference which can be used to compare plastic deformation in states other than critical (Roscoe, 1971, p. 940). The significance of this approach should become apparent, especially when specific examples of triaxial deformation are considered in the next section.

The Cambridge models employ a series of plastic yield surfaces which in a triaxial P'-Q' diagram appear as a nested set of elliptical curves radiating out from the origin (Figure 25a). Only one yield surface is active at a time, depending on the current void ratio and pressure (e, P') of the deforming sediment. A sediment with a state-of-stress (P', Q') inside the current yield surface will only deform elastically, while a state-of-stress on the yield surface permits plastic deformation. The current yield surface therefore bounds the regions of elastic, fully recoverable strain. A state-of-stress outside of the current yield surface is not possible until an increment of plastic strain reduces the void ratio and causes the yield surface to move outward.

Yield surfaces used in the modified Cam Clay model are described by the following expression (Roscoe and Burland, 1968, p. 549):

$$\frac{(P' - P'_o/2)^2}{(P'_o/2)^2} + \frac{Q'^2}{M^2} = 1 \qquad (15)$$

where P'_o defines the current position of the yield surface. This equation indicates that the yield surface is an ellipse with its major axis lying on the P' axis. The ellipse intersects the P' axis at the origin and at P'_o; the minor axis is vertical and extends to the point where the ellipse intersects the critical state line at $P' = P'_o/2$ and $Q' = M\,P'_o/2$. The position of the current yield surface is therefore defined solely by the variable P'_o, which is a function of the current void ratio and pressure. P'_o can be determined graphically from the e-P' diagram. The K-line passing through the current void ratio and pressure (e, P') is traced to its intersection with the isotropic consolidation line; the pressure at this point is the current value of P'_o. Consider the example in Figure 26. A sediment with a current state at point F (e_f, P'_f, Q'_f) lies on a K-line which intersects the isotropic consolidation line at the point C; the current yield surface is located at $P'_o = P'_c$. An equation for P'_o can be derived by combining equation 4 for the K-line and equation 3 for the isotropic consolidation line, which results in :

$$\mathrm{Ln}(P'_o) = \frac{e - e_I + K\,\mathrm{Ln}(P')}{(K-\lambda)} \qquad (16)$$

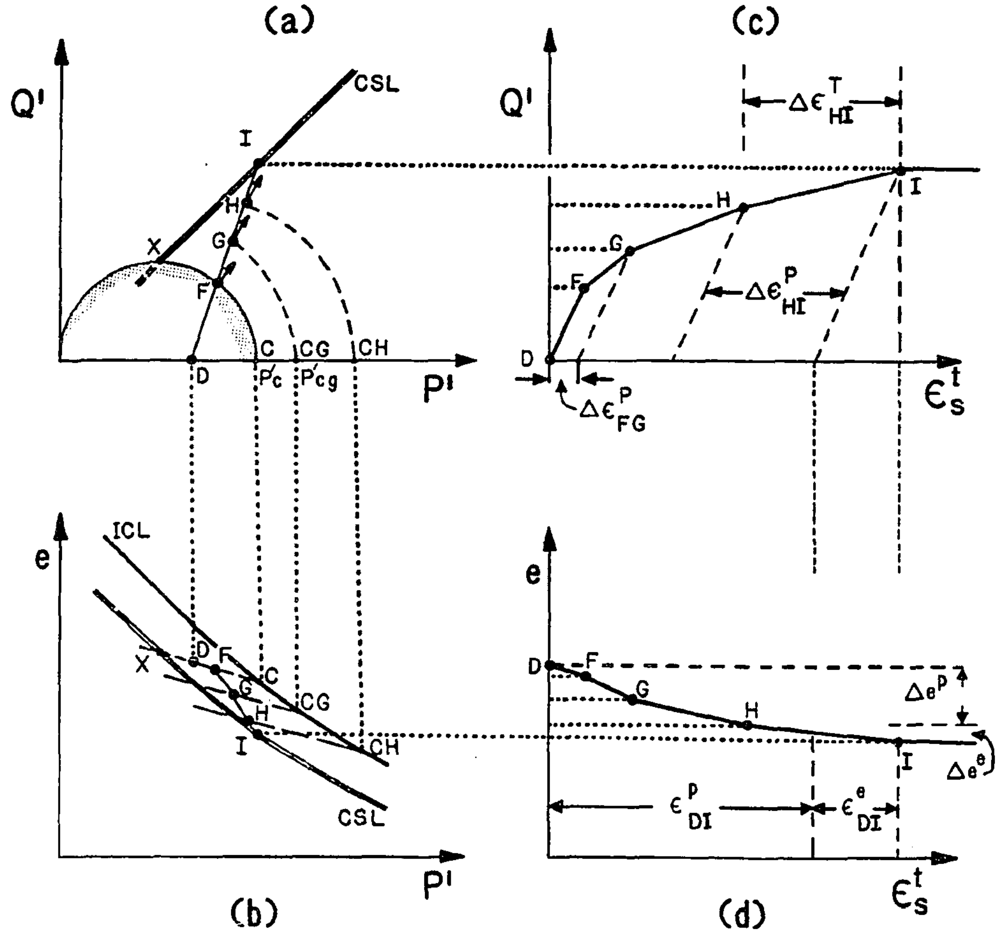

Figure 26. Drained triaxial deformation of looser-than-critical sediment, as simulated by the modified Cam Clay model (after Figure A9-1 of Jain, 1980). Prior to the test, the sediment is preconsolidated so that initial yield surface intersects the P' axis at point C (Figure 26a). The sediment is then deformed along a stress path from D to I; stable failure occurs at point I on the critical state line.

where e and P' are the current void ratio and pressure. It should be noted that the yield surfaces used in the other Cambridge models (Granta-Gravel, Cam Clay -- Schofield and Wroth, 1968) have a slightly different shape which reflects that fact that they use a different work function (Roscoe and Burland, 1968, p. 547-48). For the problem considered here, this difference is of minor importance.

The stress-strain relationships used in the Cambridge models employ the strain increment approach of plasticity theory (Ramsay, 1967, p. 319; Atkinson and Bransby, 1978, p. 274-83), where the principle directions of the plastic strain increment are considered to be parallel with the principle stress directions. Roscoe, et al. (1967) present evidence that supports this assumption. The resulting deformation need not be coaxial, unless the principal stress directions remain fixed to the finite strain axes throughout the deformation, which, in fact, is the case for triaxial deformation. Thus, for the P'-Q' diagram in Figure 25, the P' axis corresponds to the plastic volumetric strain increment, $d\epsilon_v^p$, and the Q' axis corresponds to the plastic shear strain increment, $d\epsilon_s^p$ (Atkinson and Bransby, 1978, p. 282). This relationship defines the orientation of the incremental plastic strain ellipsoid, but the actual shape of the ellipsoid is determined through the normality condition, which states that the plastic strain increment, due to a state-of-stress (P', Q') on the yield surface, is normal to the surface at that point (Figure 25a). Therefore, the ratio of the plastic strain increments, $(d\epsilon_s^p/d\epsilon_v^p)$, is equal to the slope of the yield surface normal $(-1/S_y)$ where S_y is the slope of the yield surface itself. The slope of the yield surface normal can be obtained by differentiating the yield surface equation (equation 15), which gives the following relationship (Roscoe and Burland, 1968, equation 34):

$$\frac{d\varepsilon_s^p}{d\varepsilon_v^p} = \frac{-1}{S_y} = \frac{2Q'P'}{(MP')^2 - Q'^2} \tag{17}$$

The left side of this equation yields the following relationship:

$$S_y = -d\varepsilon_v^p/d\varepsilon_s^p \tag{18}$$

which relates the normality condition in a more comprehensible form. Simply stated, where the yield surface is steep (i.e., S_y is large), plastic deformation results in a much greater volumetric strain relative to shear strain. Conversely, where the surface is gently dipping (i.e., S_y is small), shear strain is much greater (note that at the critical state line, the yield surface is flat, indicating that $d\varepsilon_v^p = 0$). Therefore, the slope of the yield surface at the current state-of-stress (P',Q') gives an immediate indication of the relative proportion of shear strain $d\varepsilon_s^p$ to volumetric strain $d\varepsilon_v^p$ that will occur in the next increment of plastic deformation.

Since the normality condition only specifies the relative proportion of the components of the plastic strain increment ($d\varepsilon_s^p/d\varepsilon_v^p$), another relationship is need to determine the actual magnitude of one of these components. For this purpose, equation 11 is recast in terms of P'_o, which results in (Roscoe and Burland, 1968, equations 15 and 17):

$$d\varepsilon_v^p = \frac{-de^p}{(1+e)} = \frac{(K-\lambda)}{(1+e)} \frac{dP'_o}{P'_o} \tag{19}$$

where e is the current void ratio, de^p is the plastic incremental change in void ratio, and dP'_o and P'_o are determined from equation 16.

We have accounted for the plastic strain components, $d\varepsilon_v^p$ and $d\varepsilon_s^p$, and the elastic volumetric strain component, $d\varepsilon_v^e$, which leaves the elastic shear strain component, $d\varepsilon_s^e$. Early Cambridge models assumed that elastic shear strain was negligible (Schofield and

Wroth, 1968; Roscoe and Burland, 1968). More recent investigators (Atkinson and Bransby, 1978; Wroth and Houlsby, 1981; Jain, 1980) include a linear elastic shear strain component, defined by:

$$d\varepsilon_s^e = dQ'/3G \tag{20}$$

where G represents a constant shear modulus. The elastic shear strain component becomes important for problems of non-homogeneous deformation. Wroth and Houlsby (1981) cite shear modulus values G for several clays, all of which are between 2 - 14 MPa.

These relationships form the basis of the modified Cam Clay model. Given the five material constants for a particular sediment (K, λ, e_I, M, and G), all of which can be determined from standard triaxial tests, the model can be used to predict stress-strain relationships and the point of failure during progressive deformation. Table 3 gives some average values of λ, K, and M for sands and clays (from compilation by Egan and Sangrey, 1978). Maximum and minimum void ratios are also included to give an indication of the relative volumetric strain possible during typical deformation. In the next section, this model is used to examine specific examples of triaxial deformation.

Table 3. Average and range of material constants for typical sands and clays (from compilation by Egan and Sangrey, 1978).

MATERIAL CONSTANTS	CLAYS (n=16)	SANDS (n=9)
λ	0.204 (0.071-0.69)	0.119 (0.020-0.37)
K *	0.040 (0.011-0.18)	0.0081 (0.0043-0.015)
M	1.03 (0.85-1.53)	1.42 (1.29-1.58)
e_{max} †	1.73 (0.77-3.52)	1.22 (0.73-2.22)
e_{min} †	0.79 (0.5-1.20)	0.66 (0.38-1.23)

* The values of K compiled by Egan and Sangrey (1978) are actually for the elastic reloading curve, so that these values are somewhat less than K used in the model, which is the average of the unload and reload curves.

† e_{max} and e_{min} are given as a rough measure of the range of void ratios that a deforming sediment might attain. For clays, e_{max} and e_{min} represent the liquid and plastic Atterberg limits. For sands, these values represent the void ratios at minimum and maximum relative density.

EXAMPLES OF TRIAXIAL DEFORMATION

In this section, four examples of triaxial deformation are presented with the purpose of illustrating how loose and dense sediments respond under drained and undrained conditions. These examples are not real triaxial tests, but instead are simulated using the modified Cam Clay model. They are, however, representative of typical laboratory triaxial tests, such as those presented by Bishop and Henkel (1962). Any discrepancies between the model and real triaxial tests are noted in the descriptions below. It should be emphasized that, in these simulated tests, loading occurs slowly and the sediment is saturated by the pore fluid; these conditions ensure that a uniform pore pressure is maintained throughout the sediment during deformation.

DRAINED DEFORMATION OF LOOSE SEDIMENT

Figure 26 shows the results of a simulated drained triaxial test based on the modified Cam Clay model. (This example is adapted from Jain [1980]; he also provides a short description of the numerical procedure used for the model.) Prior to the simulated test, the sediment is isotropically consolidated to a pressure P'_c and void ratio e_c, corresponding to point C in Figure 26b. The sample is then unloaded to point D where the test begins. The load test is shown as a stress path, labelled D through I, in the P'-Q' diagram. The test begins at point D, and continues until it reaches the critical state line at point I where the sediment fails. In addition to the typical P'-Q' and e-P' diagrams, Figure 26 also shows how Q' and e change with increasing shear strain ε_s^t.

Preconsolidation of the sediment establishes the intercept of the initial yield surface at point C with $P'_o = P'_c$. The test starts with the first stress increment from point D to F, which is inside the initial yield surface, and results only in elastic deformation, as shown in Figure 26c and 26d. The fact that D and F lie on the same K-line in the e-P' diagram indicates the elastic nature of the volumetric strain component. If the sediment were unloaded back to point D, the strain increment would be completely recovered and the initial yield surface would remain in the same position.

The next stress increment, F-G, crosses the initial yield surface resulting in a combined elastic-plastic strain increment. The resulting increment of plastic volumetric strain is shown in the e-P' diagram by a departure from the K-line at point F. The magnitude of the plastic volumetric strain is represented by the distance parallel to the e axis between K-lines containing F and G. The amount of plastic shear strain ε_s^p can be determined by graphically unloading the sediment back to the ε axis. The slope of the elastic loading path, represented by D-F in the ε_s^t-Q' diagram, can be used for this purpose, since the elastic shear modulus is constant (equation 20). An example of this procedure is shown by the dashed line from point G (Figure 26c).

Strains imposed by the stress increment F-G cause the yield surface to shift to CG with $P'_o = P'_{cg}$ (Figure 26a). For a simulated test, the yield surface moves in incremental steps, but in reality it should move in a continuous fashion with increasing stress. The next stress increment, G-H, results in another increment of elastic-plastic strain, similar to that for F-G. The effect of the normality condition (equation 18) can be seen by comparing the decreasing slope of the yield surface at successive points on the stress path (Figure 26a) with the decreasing slope of the shear strain (ε_s)-void ratio (e) curve in Figure 26d. In addition, the slope of the deviatoric stress (Q')-shear strain (ε_s) curve (Figure 26c) shows a steady decrease, which reflects a decreasing rate of strain-hardening as the stress path approaches the critical state.

Stable failure occurs when the stress path reaches the critical state at point I. The yield surface at this point has a slope of zero, so that $S_y = (-d\varepsilon_v^p/d\varepsilon_s^p) = 0$. As discussed above, plastic deformation at the critical state occurs at constant volume. Therefore, since $(d\epsilon_v^p/d\epsilon_s^p) = 0$ and $d\epsilon_v^p = 0$, the plastic shear strain increment $(d\epsilon_s^p)$ becomes indeterminate, which reflects the fact that there is no longer a mechanism, such as strain-hardening, to stabilize the deformation.

If pressure and deviatoric stress continue to increase after failure, then the stress path would diverge from point I and start to follow the critical state line to the right. This relationship illustrates the fact that, for loosely packed strain-hardening sediments, the critical state line represents a limit boundary directly analogous to the Mohr-Coulomb failure envelope; the sediments cannot sustain deviatoric stresses larger than those at the critical state.

DRAINED DEFORMATION OF DENSE SEDIMENT

The preceeding example shows how the model accounts for the stress-strain behavior of loosely packed, strain-hardening sediment. Densely packed sediment can respond quite differently during progressive deformation. The initial yield surface, which intersects the P' axis at point CL in Figure 27, bounds a large elastic region on the P'-Q' diagram (the dashed yield surfaces shown inside the initial yield surface do not become active until later in the deformation). Note that the critical state line does not continue below the initial yield surface; only elastic recoverable strains occur within this region.

The current state of the sediment (P_k', Q_k', e_k), represented by point K, lies well within the initial yield surface, indicating that the sample was previously deformed and consolidated along a stress path that ended somewhere on that surface and then was unloaded. Therefore, the initial state of the sample is described as highly overconsolidated because its void ratio is much smaller than would be expected from its present load condition (P_k', Q_k'). This highly overconsolidated condition is illustrated in the e-P' diagram (Figure 27) where point K lies on the dense side of the critical state line, far below the isotropic consolidation line. In soil mechanics,

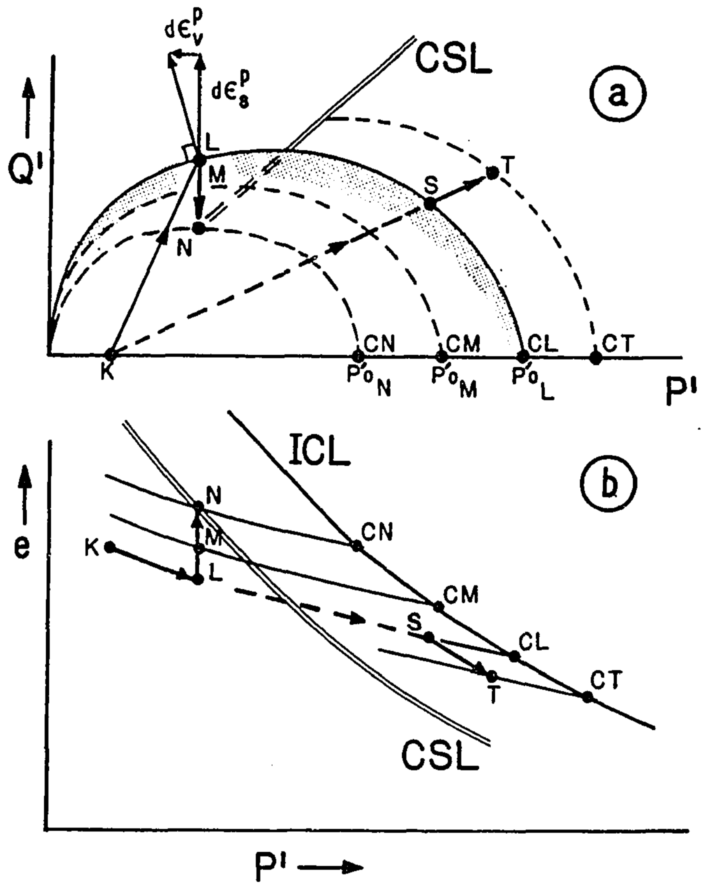

Figure 27. Drained triaxial deformaton of denser-than-critical sediment, as simulated by the modified Cam Clay model. Unstable strain-softening deformation begins when the stress path K-N meets the initial yield surface at point L. Plastic yielding cause the sediment to become progressively weaker, and to fail by rupture failure. A shallower stress path, such as K-T, would result in stable strain-hardening deformation because the stress path would intersect the initial yield surface in a state looser-than-critical.

the term overconsolidated and normally consolidated are defined as follows (Lambe and Whitman, 1979, p.74,299): an overconsolidated sediment is presently under an effective stress less than that to which it was once consolidated, whereas a normally consolidated sediment is currently under the maximum stress it has ever experienced. With respect to the modified Cam Clay model, an over consolidated sediment has a state-of-stress inside the current yield surface, whereas a normally consolidated sediment has a state-of-stress that lies somewhere on the strain-hardening portion of the current yield surface. The degree of overconsolidation is typically indicated by on over-consolidation ratio (Atkinson and Bransby, 1978; Lambe and Whitman, 1979, p.299), which represents the relative position of the current state-of-stress for the sediment, with respect to the position of the current yield surface. Atkinson and Bransby (1978) use the ratio: P'_o/P', where P'_o is the P'-axis intercept of the current yield surface and P' is current pressure of the sample. Highly overconsolidated sediments have $P'_o/P' > 2$; the example shown in Figure 27 has a ratio equal to 7.6 (P'_{oL}/P'_k).

Highly overconsolidated sediments are prone to unstable brittle failure as illustrated by stress path K-N. The first stress increment K-L results in elastic strain, which is represented by a reduction in void ratio as the sediment moves from K to L on the elastic K-line in the e-P' diagram. The first increment of plastic yielding occurs at point L and involves strain-softening behavior, as indicated by the positive slope of the yield surface ($S_y>0$) for the region to the right of the critical state line. When $S_y>0$, the normality condition indicates that one of the plastic strain components is less than zero, since $S_y = (-d\epsilon^p_v/d\epsilon^p_s) > 0$ (equation 18). Triaxial shortening requires that the shear strain is greater than zero ($d\epsilon^p_s>0$), indicating that the first plastic strain increment at point L must have a negative volumetric strain component ($d\epsilon^p_v<0$), which corresponds to an increase in volume and in void ratio. This volume increase represents the dilatancy effect characteristic of highly overconsolidated sediments, and also of brittle deformation of rock.

The negative volumetric strain causes the yield surface to move inward towards point M, which indicates that the yield strength of the sediment is decreasing.

As the sample deforms between L and N, strain-softening behavior leads to localized zones of deformation which result in elastic unloading and rupture failure. (This failure process is considered in more detail by Rudnicki and Rice [1975] who treat it as a bifurcation problem.) Because the sample weakens with progressive deformation, it becomes impossible to determine the stress path beyond the initial yield point at L, although it ultimately converges on the critical state line, perhaps as shown by point N. The progressive stress-strain path shown in Figure 27 applies only for the failure zone (Atkinson and Bransby, 1978, p. 227). For instance, the strain-softened failure zone might exhibit a yield strength of Q'_n, whereas the surrounding "harder" sediment would retain its initial yield strength, Q'_L.

In general, these relationships are consistent with experimentally observed behavior, but it should be noted that the modified Cam Clay model tends to overpredict the peak strength of overconsolidated sediments (denser-than-critical). In order to correct this problem, Atkinson and Bransby (1978, p. 211) employ a different yield surface for the region in the P'-Q' diagram to the right of the critical state line. Another discrepancy is that after rupture failure in clays, further deformation causes the strength of the rupture surface to decrease from its critical state value, or ultimate strength, to a residual strength (Skempton, 1964; Schofield and Wroth, 1968, p. 225). Schofield and Wroth (1968) suggest that the material properties of the clays at the rupture surface are modified by the very large shear strains that become concentrated at the rupture surface after localization sets in. If correct, this interpretation indicates that the material "constants" of the model can change during the course of the deformation. In any case this phenomenon ensures that a strain-soften rupture surface actually remains much weaker than the surrounding sediment.

Highly overconsolidated sediments do not always deform by strain-softening failure. An alternative stress path, labelled K-T in Figure 27, would have resulted in stable strain-hardening deformation similar to the example described above in Figure 26. The important distinction that must be made is whether the sediment is looser or denser than the critical state when it first reaches the initial yield surface. Strain-softening occurs when the stress path intersects the yield surface to the left of the critical state line, so that $P' < P'_o/2$, where P'_o represents the P-axis intercept of the initial yield surface. As can be seen, the occurrence of strain-softening or strain-hardening yielding is a function of both the stress path and the position of the yield surface.

UNDRAINED DEFORMATION OF LOOSE SEDIMENT

Deformation of low permeability sediments, such as clays and muds, commonly occurs under partially drained or, in the extreme, under completely undrained conditions. In soil mechanics, this situation is simulated by an undrained triaxial test where pore fluid is not allowed to move in or out of the deforming sediment. The result is that deformation occurs without volume change (based on the reasonable assumption that the pore fluid and mineral grains are relatively incompressible), and with large changes in pore pressure. This type of test is usually performed at a slowly enough to ensure a uniform pore pressure distribution (Bishop and Henkel, 1962).

Figure 28 shows the results of a simulated undrained test for a looser-than-critical sediment. Before the test, the sediment is isotropically consolidated under drained conditions to point CN on the P' axis, after which pore fluid drainage is no longer permitted. The sediment is then subjected to an applied (or total) stress path, which in this case extends from CN to F. If the test were conducted under drained conditions, the sediment would follow the applied stress path and would deform like the drained strain-hardening sediment shown in Figure 26. There is no significance to this particular applied stress

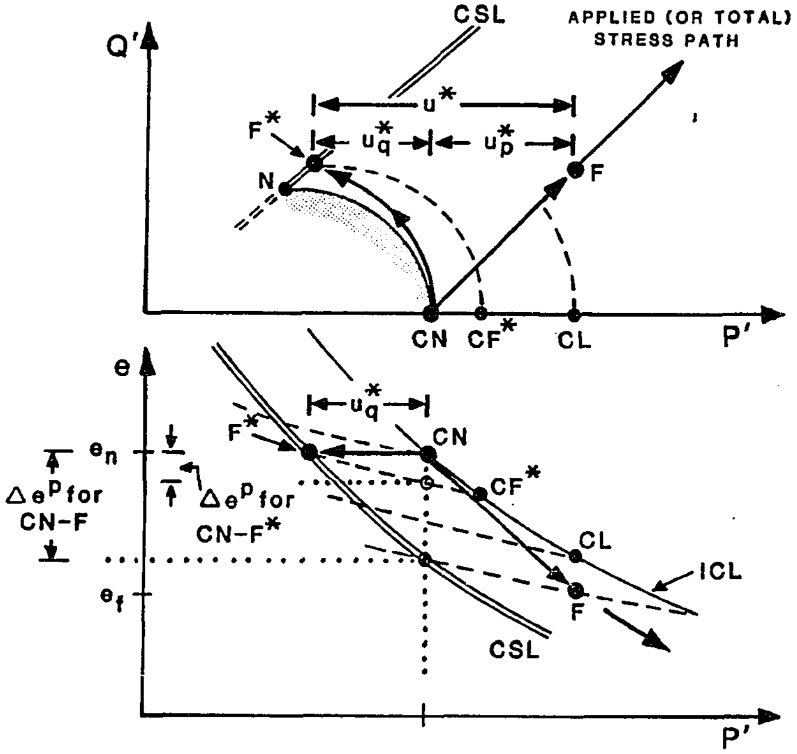

Figure 28. Undrained triaxial deformation of looser-than-critical sediment as simulated by the modified Cam Clay model. During deformation, excess pore pressure, U^*, progressively increases which causes the undrained stress path, CN-F*, diverges from the applied (or total) stress path, CN-F, and curves towards lower effective pressure.

path; in fact, it is shown below that the trajectory of the undrained stress path is independent of the orientation of the applied stress path.

The same tendency that causes strain-hardening sediments to decrease in volume during drained deformation, is manifested during undrained deformation by an increase in pore pressure. Therefore, in an undrained test, the stress path curves to the left towards lower effective pressures, as shown by the stress path CN-F^* in Figure 28. In the modified Cam Clay model, undrained deformation is simulated by holding the volume constant in the e-P' diagram (Figure 28b), so that the void ratio from its initial value, e_n, does not change during deformation. Pore pressure and effective pressure are allowed to vary, in order to compensate for this constant volume restriction. Stable failure occurs when this constant volume path reaches the critical state line in the e-P' diagram, which for this situation is at point F^*. Failure of undrained looser-than-critical sediments occurs essentially in the same way that it does in the drained case. As the state path approaches the critical state line, the amount of strain-hardening decreases to zero which results in stable failure without a significant loss-of-strength (Atkinson and Bransby, 1978, p. 178).

The excess pore pressure, U^*, developed during undrained deformation is represented by the pressure difference between the undrained and the applied (or total) stress paths (Figure 28). The excess pore pressure is composed of two components: (1) a pressure-induced component, U_p^*; and (2) a deviatoric stress-induced component, U_q^*. (U_q^* is indirectly related to the A pore-pressure parameter used in soil mechanics; see Atkinson and Bransby [1978, p. 324] for further discussion.) The pressure-induced component, U_p^*, is due to the fact that as soon as drainage is stopped (i.e., at point CN), an increase in total pressure causes an equivalent increase in pore pressure. Therefore, during undrained deformation, the effective pressure is no longer affected by changes in total pressure. For the example shown in Figure 28, the pressure-induced component at F^* is $U_p^* = P'_f - P'_{cn}$.

Since changes in total pressure are directly cancelled by U_p^*, the curved trajectory of the undrained stress path is due solely to increasing deviatoric stress, which contributes to the excess pore pressure through the component U_q^*. The explanation is as follows. During drained plastic deformation of a strain-hardening sediment, an increase in deviatoric stress causes a decrease in void ratio (Figure 23). Since undrained deformation occurs at constant volume, an increase in deviatoric stress is accompanied by a decrease in effective pressure, which in fact is compensating for the potential change in void ratio. The pore pressure component U_q^* is what actually causes the change in effective pressure. In the example shown in Figure 10, the deviatoric stress-induced component at F^* is $U_q^* = P'_{cn} - P'_{f*}$.

As might be expected, when the sediment fails at the critical state line, continued undrained deformation occurs without any further increase in U_q^* (Atkinson and Bransby, 1978, p. 219). This situation reflects the fact that the sediment is now deforming at its critical state. Since any change in total pressure is cancelled by U_p^*, the effective pressure no longer decreases. Therefore, continued undrained deformation occurs at a constant deviatoric stress with the state path fixed at the initial point of failure (i.e., at point F^*).

Now consider an applied stress path originating from point CN but with a slope different from that of the applied path shown in Figure 28. During undrained deformation, this new stress path will develop a different amount of excess pore pressure; however, the component U_q^* remains the same with the difference in excess pore pressure due solely to U_p^*. It becomes apparent from this example that any applied stress path originating from point CN and increasing in deviatoric stress will result in the same undrained stress path CN-F^* and will fail at the same deviatoric stress, Q'_f (Atkinson and Bransby, 1978, p. 306). As a result, the strength of the sediment remains constant despite changes in total pressure. This relationship, which is well established in soil mechanics (Lambe and Whitman, 1979, p. 433; Atkinson and Bransby, 1978, p. 306), represents the underlying concept for the routine soil test of undrained shear strength. The undrained shear strength is equal to half of the deviatoric stress at failure. For the test shown in Figure 28, the undrained shear strength is $Q_f'/2$.

Another aspect of undrained deformation is that, when compared with drained deformation conducted under similar conditions, the amount of plastic strain before failure is much reduced, primarily because of the constant volume restriction imposed by the undrained condition. Plastic volumetric strains do occur (represented by Δe^p for CN-F* in Figure 28), but they are relatively small because they have to be directly compensated by elastic volumetric strains, which are typical small. Therefore, because of the normality condition (equation 18), a smaller plastic volumetric strain implies a smaller plastic shear strain. Schofield and Wroth (1968, p. 186) give evidence that for normally consolidated clays, pre-failure shear strain for a typical drained test is about 2.5 to 3.5 times greater than that for a comparable undrained test. Because sands are elastically stiffer than clays (Table 3), the difference in pre-failure shear strain for drained and undrained tests should be greater.

The small amount of plastic strain that does occur during undrained strain-hardening deformation causes the undrained stress path to continually move outward--although at a low angle--from the current yield surface. Therefore, despite the fact that load-related[5] excess pore pressure can become very large, the undrained stress path will always lie in a region to the right of the initial yield surface and beneath the critical state line. This

[5] In the case considered here, excess pore pressure is assumed to be entirely the result of the applied load. The effect of internally generated pore pressure, caused by diagenetic reactions, generation of methane, etc., is considered briefly in another section below.

conclusion indicates that, regardless of drainage conditions, looser-than-critical sediments will always display the same general deformational behavior, that is, strain-hardening and stable failure. Furthermore, for looser-than-critical sediments, the critical state line represents a fundamental stress limit for both drained and undrained stress paths. Drainage conditions do affect the details of the deformation. When compared with drained deformation, the undrained condition causes a reduction in ductile strain before failure and a decrease in failure strength.

UNDRAINED DEFORMATION OF DENSE SEDIMENT

An example of undrained deformation of denser-than-critical sediment is shown by the state path K-M^* in Figure 29. For purposes of comparison, the drained stress paths K-N and K-S from Figure 27 are also included. The sediment in its initial condition at point K is highly overconsolidated and is associated with an initial yield surface that bounds a large elastic region. As is shown in the preceeding section, an undrained stress path is indifferent to changes in total pressure. Therefore, the undrained stress path K-M^* would result from any applied stress path that originates from point K and increases in deviatoric stress; the stress paths K-L and K-S are two possibilities.

The undrained test begins at point K, and is simulated by holding the initial void ratio, e_k, constant through the course of the test, as shown in the e-P' diagram. The first segment of the undrained stress path is vertical, because U_p^* cancels any change in total pressure. However, unlike the example in Figure 28, this initial segment of the stress path is not curved, because U_q^* is zero for the elastic region inside the initial yield surface. Only when the sediment is deforming plastically can deviatoric stress cause significant changes in volumetric strain and/or pore pressure (Atkinson and Bransby, 1978, p. 324-6). The stress path starts to curve when it meets the initial yield surface; at this point, the sediment begins to deform plastically in an unstable strain-softening fashion. The same

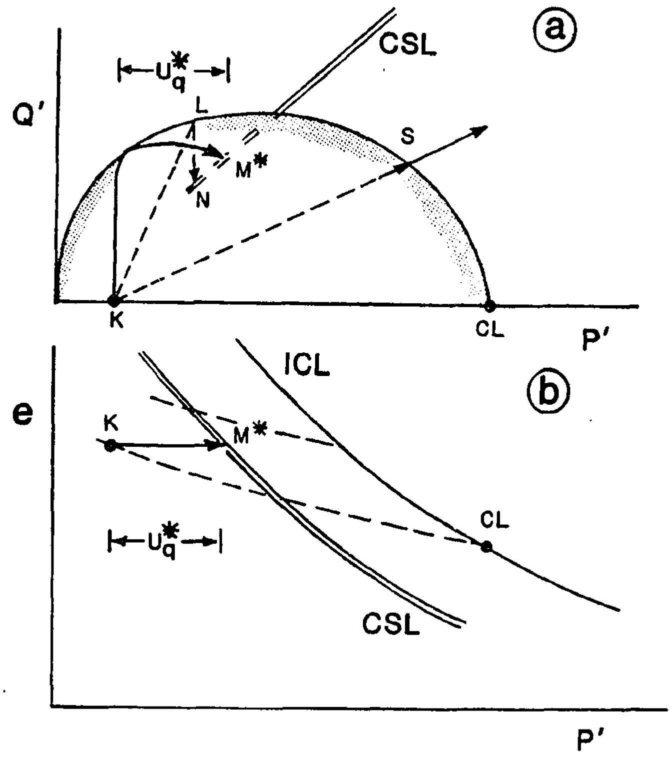

Figure 29. Undrained triaxial deformation of denser-than-critical sediment, as simulated by the modified Cam$_*$Clay model. Plastic yield begins when the undrained stress path, K-M*, reaches the initial yield surface. During undrained strain-softening deformation, pore-pressure progressively decreases which causes the undrained stress path to curve towards higher effective pressure. This simulated example is at variance with actual triaxial tests, and also with a theoretical analyses by Rice (1975). These discrepancies are discussed in the text.

tendency that causes strain-softening sediments to increase in volume (dilate) during drained deformation, is manifested by a decrease in pore pressure during undrained deformation. As a result, the effective pressure increases with continued plastic deformation, until the undrained path intersects the critical state line at point M^*, as shown in the e-P' diagram. This decrease in pore pressure represents the excess pore pressure component U_q^*; the magnitude of this component at failure is shown in Figure 29.

While the general pattern is correct, the simulated example in Figure 29 has some important differences when compared with a real triaxial test. One minor discrepancy is that in a real test, the initial segment of the stress path is not vertical but instead curves to the right at a steep angle (Atkinson and Bransby, 1978, p. 223; Bishop and Henkel, 1962). This discrepancy may be an artifact of the testing apparatus, or alternatively, it may indicate that a real sediment undergoes some plastic deformation before reaching the initial yield surface. A more important discrepancy is that in real triaxial tests, a loss-of-strength at failure is not observed (Atkinson and Bransby, 1978, p. 181; Bishop and Henkel, 1962). Futhermore, it is not clear from these tests whether or not a rupture surface forms in the failed sediment. The underlying problem is that, because of its unstable nature, strain-softening deformation is difficult to simulate in a model and is also difficult to observe in a testing apparatus (Atkinson and Bransby, 1978, p. 218; Wood, 1982; Rice, 1975). For example, Rice (1975) points out the importance of local variations in pore pressure and in volume change that develop during rupture failure. These variations are not accounted for in the model, and are not detected or catered to in a typical triaxial test. Therefore, it becomes doubtful whether either of these situations, the model or the triaxial test, is representative of the failure behavior of the sediments under natural conditions.

Rice (1975) examines the deformational stability of dilatant, strain-softening materials (i.e., denser-than-critical sediments) during undrained simple shear. His results are not directly applicable to the triaxial situation, but they are certainly relevant to the subduction zone setting, which closely approximates a simple shear zone (Figure 20). He shows quite clearly that undrained dilatant materials will develop heterogeneities in deformation, which presumably will lead to rupture failure as soon as they reach their drained peak strength and begin to strain-soften. Even though dilatancy causes an overall decrease in pore pressure, Rice (1975) shows that as the incipient rupture surface begins to strain-soften, a very localized, relative increase in pore pressure develops within the failure zone, and causes it to become progressively weaker. While he makes no explicit prediction, Rice's analysis suggests that the loss-of-strength at failure during undrained deformation is similar to that for the drained case.

Rice (1975) and Rudnicki and Rice (1975) conclude that, regardless of drainage conditions, rupture failure is the characteristic failure mode of strain-softening materials, such as brittle rocks and denser-than-critical sediments. This conclusion emphasizes the importance of the critical state line, which delimits those states where a sediment has fundamentally different types of deformational behavior--strain-hardening and stable failure vs. strain-softening and rupture failure.

SUMMARY OF DEFORMATIONAL BEHAVIOR

The examples above indicate that the deformational behavior of a sediment is affected by three factors: (1) consolidation state, (2) stress path, and (3) drainage conditions. Table 4 summarizes the effects of these factors on deformational processes and structural styles. Of these three factors, the stress path and drainage conditions play a subordinate role. For instance, failure is more likely to occur under poor drainage conditions; however, the mode of failure--whether it be rupture failure or stable failure--will remain unchanged, as illustrated in Figure 30.

Table 4. A summary of structural styles and deformational processes affecting deforming sediments.

STRUCTURAL STYLE *	DEFORMATION PROCESS	CONTRIBUTING FACTORS † §
TYPE 1 ductile deformation without failure	strain-hardening	• normally consolidated ** • gentle stress path drained condition
TYPE 2 minor to moderate pre-failure ductile strain; closely spaced slip surfaces	strain-hardening & stable failure	• normally consolidated ** steep stress path partially drained
TYPE 3 widely spaced faults; minor pre-failure ductile strain	strain-softening & rupture failure	• highly overconsolidated steep stress path partially drained

* Refers to styles shown in Figure 21.

† For these contributing factors: required factors are marked with a dot; the unmarked factors are not required but at least one is needed.

§ A steep stress path intersects the critical state line, while a gentle path does not.

** As used here, the term normally consolidated also includes underconsolidated sediments.

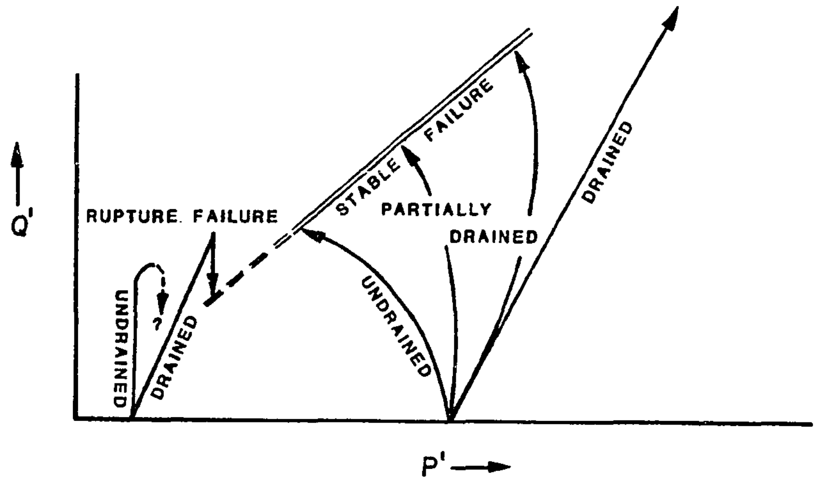

Figure 30. A schematic summary of failure modes for various stress paths. Two partially drained stress paths are included in this figure. They are curved in a fashion similar to undrained stress paths, but since excess pore pressure is partially dissipated during deformation, the partially drained paths do not diverge as much from the drained stress paths.

With respect to the subduction zone problem, we are mostly interested in those factors that cause deformation to become localized, and therefore are probably responsible for the formation of discrete faults (Type 3 structural style in Figure 21). Given the large strains that occur in the subduction zone setting (Figure 20), much of the deformation probably occurs after the sediments reach failure. Hence, the consolidation state of the sediment--whether it is normally consolidated (looser-than-critical) or highly overconsolidated (denser-than-critical)--is the main factor that determines whether or not localization will occur. For highly overconsolidated sediments, localization occurs during rupture failure, and the rupture surface is significantly weaker than the surrounding unfailed sediment. As a result, a Type 3 structural style, characterized by widely spaced, discrete faults, is likely to develop. However, for normally consolidated sediments, there is no strong tendency for localization, since stable failure occurs without a significant loss of strength. For these sediments, continued deformation after failure probably results in a Type 2 structural style, which is probably characterized by a more distributed development of closely spaced slip surfaces (Figure 21).

LOADING CONDITIONS AT A SUBDUCTION ZONE

In the preceeding sections, we examined the various factors controlling the deformational behavior of unlithified, water-saturated sediments, with the ultimate goal being to predict the structural style of deforming sediments in a subduction zone setting. At this point, it is appropriate to consider how the loading conditions at the subduction zone might affect this behavior. Sediments on the down-going plate can be characterized by a two-stage loading history. The first stage involves deposition and compaction in a basinal setting. The second stage occurs as these sediments approach and descend beneath the inner trench slope. We are primarily interested in what occurs during the second stage of this loading history, but one of the main conclusions of the preceeding section is that for slow rates of deformation, the initial state of a sediment is what largely determines its subsequent deformational behavior. Compaction actually represents a special type of plastic deformation, which is referred to in soil mechanics as rest-state consolidation. Therefore, this process is examined below with a special emphasis on how it affects the state of a sediment.

REST-STATE CONSOLIDATION

Consolidation of sediment in a flat-lying basin represents a special type of strain-hardening deformation where, due to lateral confinement of the basin, horizontal strains are approximately zero (ε_H=0). For this situation, the maximum compressive stress , σ'_V, is oriented vertically and is due to gravity (equivalent to the effective overburden stress); horizontally directed stresses, σ'_H, are equal in all directions, and are of sufficient magnitude to prevent horizontal strains. This state-of-stress is referred to as rest-state or K_o consolidation (Lambe and Whitman, 1979, p. 100). The principal stress directions remain fixed during K_o consolidation, so long as the basin remains flat-lying and is in a rest-state condition (ϵ_H=0).

As sediments are buried and compacted, they are subjected to an increasing vertical effective stress, σ'_V. During rest-state consolidation, a fairly constant ratio, called the K_o ratio, is maintained between horizontal and vertical effective stresses ($K_o = \sigma'_H/\sigma'_V$). The actual values of this K_o ratio is dependent on the specific sediment; measured values for normally consolidated sands and clays range from 0.3 to 0.75 (Mayne and Kulhawy, 1982). The ratio can also be estimated using a well tested empirical relation (Mayne and Kulhawy, 1982; Jaky, 1944):

$$K_o = \frac{\sigma'_H}{\sigma'_V} - \frac{6 - 2M}{6 + M} = (1 - \sin \emptyset) \qquad (21)$$

where $\emptyset$ is the angle of friction at the critical state and M is the slope of the critical state line (see equations 13 and 14).

We can use the K_o ratio to determine a stress path for K_o consolidation in a P'-Q' diagram. If the material constants for the sediment are also known, the modified Cam Clay model can be used to predict and simulate K_o consolidation (Roscoe and Burland, 1968, p. 563). The P'-Q' and e-P' diagrams in Figure 31 show an example of the state path during K_o consolidation. The material constants used are representative of London Clay, an Eocene marine clay (Schofield and Wroth, 1968, p. 157). In the P'-Q' diagram, the K_o stress path is directed outward from the origin with a constant slope, N_{Ko}, which is dependent on the K_o value:

$$N_{Ko} = \frac{Q'_{Ko}}{P'_{Ko}} = \frac{3 - 3K_o}{1 + 2K_o} = \frac{3M}{6 - M} \qquad (22)$$

Based on the range of measured K_o values cited above, equation 22 indicates that K_o stress paths for a variety of sediments have slopes, N_{Ko}, between 0.3 and 1.3. Furthermore, using typical values for M

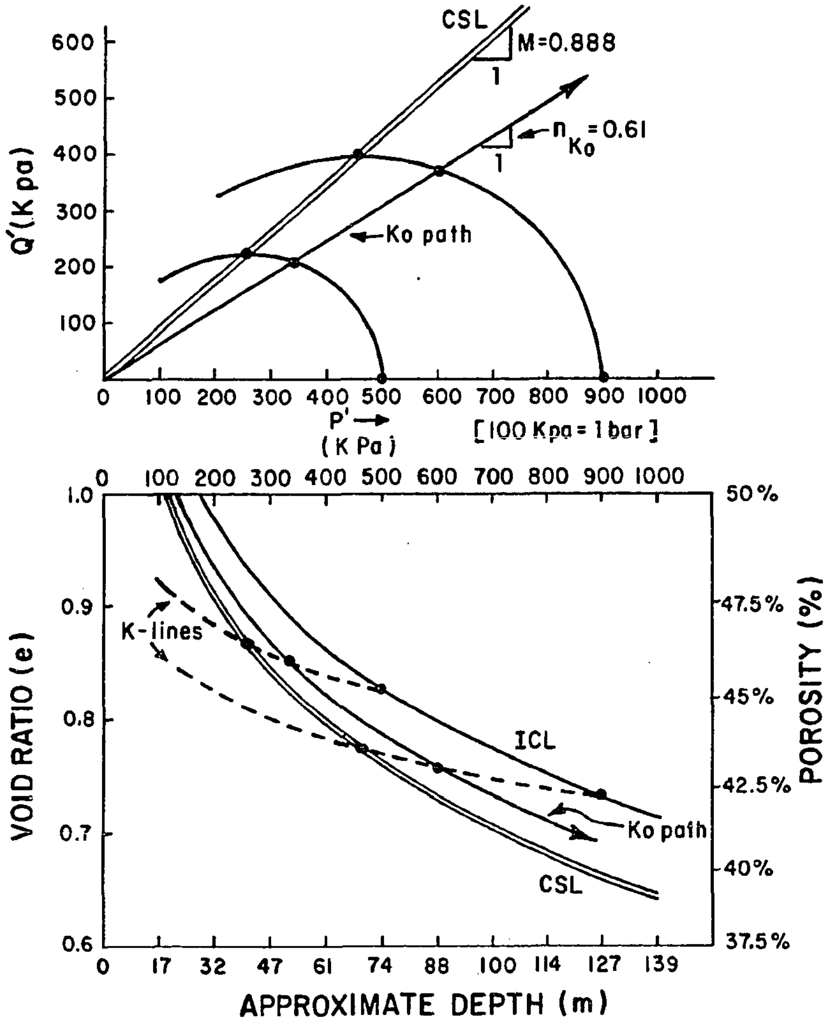

Figure 31. Rest-state consolidation as predicted by the modified Cam-Clay model. The K_o stress path is shown in the P'-Q' diagram and the resulting consolidation path lies between the isotropic consolidation line (ICL) and the critical state line (CSL) in the e-P' diagram. Values used for the model are representative of a marine clay reported in Schofield and Wroth (1968).

(Table 3), it is quite clear, and also reasonable, that the K_o stress path always lies between the critical state line and the P' axis (i.e., $0 < N_{Ko} < M$). Another feature of drained K_o consolidation is that the consolidation path in an e-P' diagram lies between the isotropic consolidation line and the critical state line, and does not intersect either of these lines (Figure 31). The K_o consolidation curve follows the same e-Ln(P') relationship as do the isotropic consolidation and the critical state lines (cf. equations 3 and 12):

$$e = e_{Ko} - \lambda \mathrm{Ln}(P') \qquad (23)$$

where e_{Ko} is the void ratio at P'= 1 kPa. Field and laboratory studies indicate that the functional form of this K_o curve is correct to moderate effective pressures, on the order of 10 to 100 MPa, which corresponds to depths of about 1 to 3 km (Skempton, 1970; Lambe and Whitman, 1979, p. 157, 320).

These relationships show that K_o consolidation is essentially a strain-hardening plastic deformation, which never reaches failure. Poorly drained conditions can inhibit the consolidation process and promote the development of excess pore pressure; however, consolidation will still follow the same K_o path, since the position of the path is dictated by the boundary conditions imposed on the consolidating sediment ($d\epsilon_H=0$) (Roscoe and Burland, 1968, p. 563).

The important point is that irrespective of drainage conditions, the stress path during K_o consolidation should be directed outward from the current yield surface and should lie to the right of the critical state line in the P'-Q' diagram. Therefore, the state path for flat-lying submarine sediments should always lie on the strain-hardening side of the critical state line (internally generated fluid overpressures or incipient lithification can alter this situation; this point is discussed below). The next section considers what happens when these sediments move into the subduction zone setting.

UNDERTHRUSTING AND PASSIVE FAILURE

Analysis of the process of K_o consolidation indicates that sediments on the downgoing plate should be in a state looser-than-critical prior to subduction. This situation suggests that as these sediments move into the subduction zone, they should continue to deform by strain-hardening or by stable failure. A plane-strain version of the modified Cam Clay model is briefly introduced below in order to examine this possibility more completely.

Deformation in a subduction zone setting can be approximated by the plane-strain condition, because total horizontal strain is approximately zero parallel to the strike of the zone. A plane-strain version of the model (Roscoe and Burland, 1968, p. 570-604) is shown in Figure 32. The t' and s' axes are analogous to the Q' and P' axes used above, where t' represents the maximum shear stress and s' repsents the mean normal stress:

$$t' = (\sigma'_V - \sigma'_H)/2 \qquad (24)$$

$$s' = (\sigma'_V + \sigma'_H)/2 \qquad (25)$$

where σ'_V and σ'_H are the principal stresses in the plane strain section. Since the principal stress directions can rotate during deformation, σ'_V and σ'_H refer to the principal stresses in the direction closest to vertical and horizontal, respectively (see inset in Figure 32). The regions above and below the s'-axis are mirror images of each other; each one contains a critical state line and a yield surface. The two critical state lines divide the diagram into strain-hardening and strain-softening regions. Since the intermediate principal strain is zero (ϵ_H=0) during K_o consolidation, it can be represented in a t'-s' diagram (Roscoe and Burland, 1968, p. 603), as shown in Figure 32. The K_o stress path is located in the upper half of the t'-s' diagram where t'>0, since σ'_H>σ'_V (equation 21) during K_o consolidation. Stress paths that extend into the negative t' region have σ'_H> σ'_V, and are associated with horizontal shortening

Figure 32. Plane-strain version of the modified Cam Clay model (after Figure 32 in Roscoe and Burland, 1968). This diagram schematically illustrates several possible stress paths for sediments in the subduction zone setting. Note that the principle stress directions rotated during deformation, as shown in the inset. During rest-state consolidation, $\sigma'_V > \sigma'_H$; whereas during passive state deformation, $\sigma'_H > \sigma'_V$.

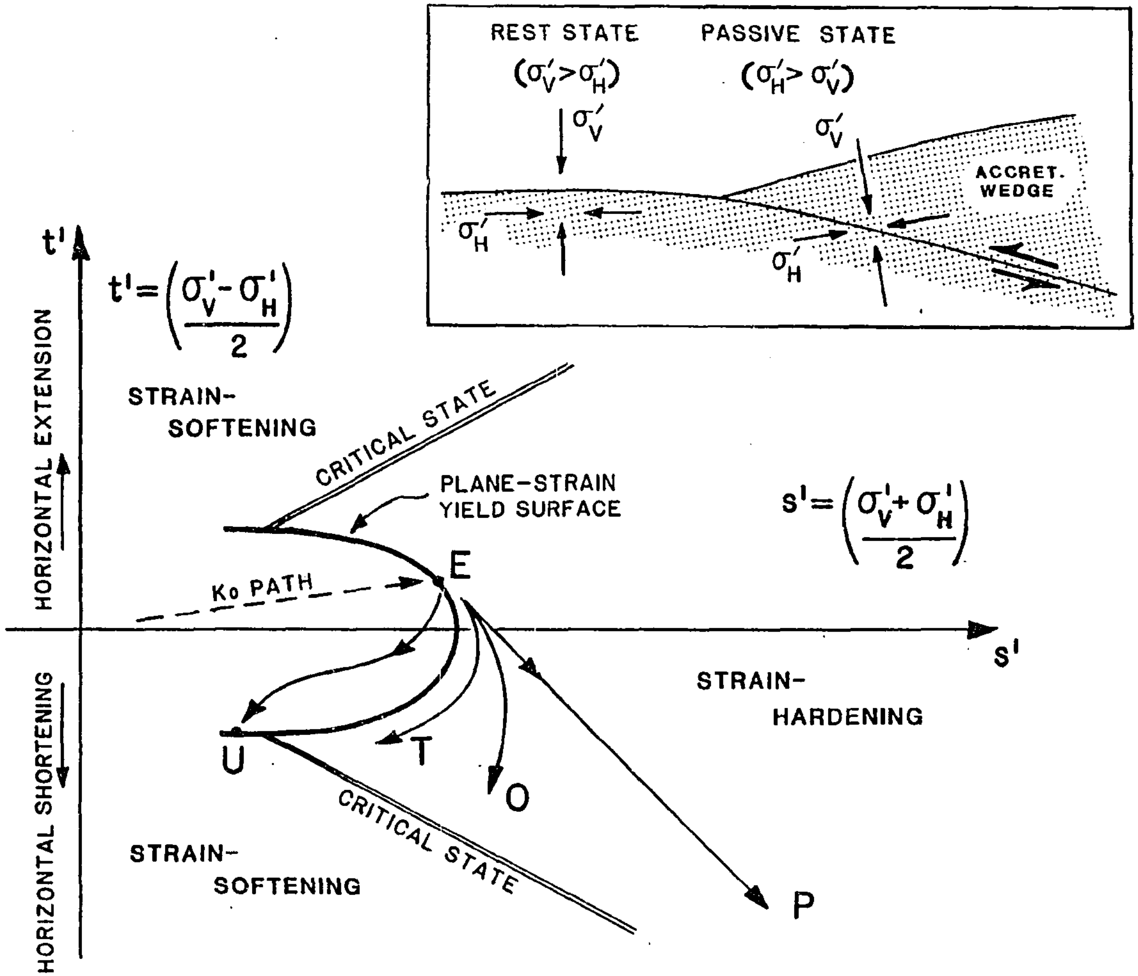
REST STATE
$(\sigma_V' > \sigma_H')$
PASSIVE STATE
$(\sigma_H' > \sigma_V')$
σ_V'
σ_H'
ACCRET. WEDGE
t'
$t' = \left(\frac{\sigma_V' - \sigma_H'}{2}\right)$
HORIZONTAL EXTENSION
HORIZONTAL SHORTENING
STRAIN-SOFTENING
CRITICAL STATE
PLANE-STRAIN YIELD SURFACE
$s' = \left(\frac{\sigma_V' + \sigma_H'}{2}\right)$
Ko PATH
E
s'
STRAIN-HARDENING
U
T
O
P
CRITICAL STATE
STRAIN-SOFTENING

and thrust faulting. In soil mechanics, this state-of-stress is called the passive state and can result in passive failure (i.e., thrust faulting) (Lambe and Whitman, 1979, p. 163).

During plane-strain deformation, s' is proportional to and is greater than P', but generally not by more than 10% (given reasonable values for M in equation 73 of Roscoe and Burland, 1968). Therefore, a change in pore pressure affects s' in the same way that it affects P'. For instance, an increase in pore pressure causes an equivalent decrease in s'; t' remains unaffected. As a result, drained and undrained stress paths in the plane-strain t'-s' diagram are similar to those in the triaxial P'-Q' diagram (for examples of real plane-strain tests see Roscoe and Burland, 1968), and result in the same general types of deformational behavior as described above (Table 4). Therefore, the plane-strain version of the model allows us to extrapolate the triaxial deformational behavior of a sediment to the plane-strain conditions prevalent at subduction zones.

The t'-s' diagram (Figure 32) schematically illustrates several stress paths that might be representative of the subduction zone setting. The diagram is intentionally vague, because a numerical solution to this problem would require information that is not currently available, such as physical properties of the sediments and the boundary conditions of the deforming zone. However, the general relationships displayed in this diagram support the suggestion made above -- that strain-hardening and stable failure characterize sediment deformation in aseismic subduction zones. Initially, sediments on the downgoing plate follow the K_o stress path. As they approach the trench slope, horizontal stress increases causing the stress path to move downward into the lower region of the t'-s' diagram, where $\sigma'_H > \sigma'_V$. If deformation occurs under totally undrained conditions, which is unlikely, these sediments would follow an undrained stress path, such as E-T. Drained deformation might result in stress paths, such as E-O or E-P. The important point is that as long as the total stresses continue to increase, which should be the case in the subduction zone setting, the effective stress path will always be directed outward from the current yield surface. Therefore, the deformational behavior of these sediments should be either strain-hardening or stable failure.

This conclusion is not as hard and fast as it may seem, because in a real geologic setting there are probably several processes that can cause a sediment to behave as if it were overconsolidated. The two most important of these processes are: (1) chemical generation of excess fluid pressure, and (2) lithification and cementation. The first process can occur by a variety of mechanisms, which include devolatilization reactions during diagenesis (Rieke and Chilingarian, 1974), or methanogenesis in organic muds (Hedberg, 1974). If fluid pressure is generated faster than it can be dissipated, which does occur in some geologic situations (i.e., methane in mud volcanoes [Hedberg, 1974]), the resulting reduction in effective pressure could leave the sediment in an overconsolidated state, perhaps as shown by the stress path E-U in Figure 32.

The second process, lithification and cementation, directly affects the material properties of the sediment and also causes a reduction in void ratio. While the effect of this process is not well studied, it is clear that lithification and cementation can cause a sediment to behave in an overconsolidated fashion (Mitchell, 1976). Even a small reduction in void ratio due to a pore-filling cement can transform a sediment into a denser-than-critical state. For example, consider the e-P' diagram in Figure 32. A 1-2% reduction in porosity could displace a sediment from the K_0 consolidation line, to the dense side of the critical state line. This example illustrates how sensitive the plastic behavior of a sediment is to small changes in material properties. Unfortunately, these processes--internally generated pore pressure, and lithification and cementation--are difficult to document in a subduction zone setting. There is some evidence, discussed below, that incipient lithification is occurring within 3 km of the front of the Barbados Ridge complex. If these processes are important, then a Type 3 structural style should be prevalent at aseismic subduction zones. If not, then a Type 2 structural style is predicted.

DISCUSSION FOR PART II

The cases described above illustrate some of the general aspects of sediment deformation, and how they might affect the structural style of sediments in a subduction-zone setting. One of the main conclusions is that the consolidation state of the sediment probably exerts the most important influence on the behavior and structural style of plastically deforming sediments. Furthermore, it is concluded that the general structural style is not significantly affected by the presence of load-induced excess pore pressure or by the expected variation in subduction-zone loading conditions. Sediments that enter the subduction-zone setting in a normally consolidated state should deform by strain-hardening and stable failure, and when subjected to large shear strains, should develop a Type 2 structural style. Whereas, sediments that are initially overconsolidated should deform by strain-softening and by rupture failure, and should develop a Type 3 structural style. Normally consolidated sediment can be transformed into an overconsolidated state by geologic processes such as: (1) internally generated pore pressure or (2) cementation and lithification. These processes should promote the development of a Type 3 structural style.

These predictions are best tested by drilling at modern convergent margins. Unfortunately, DSDP drilling has generally not been successful in reaching the depths necessary to sample accretionary structures. A notable exception is Leg 75A at the Barbados Ridge complex which has documented both Type 2 and Type 3 structural styles. These results are discussed below.

STRUCTURAL STYLE AT THE BARBADOS RIDGE COMPLEX

The cross-section in Figure 33 (adapted from Cowan, et al., in press; and Moore, Biju-Duval, et al., 1982) summarizes the major results of the drilling transect at the Barbados Ridge complex. Based

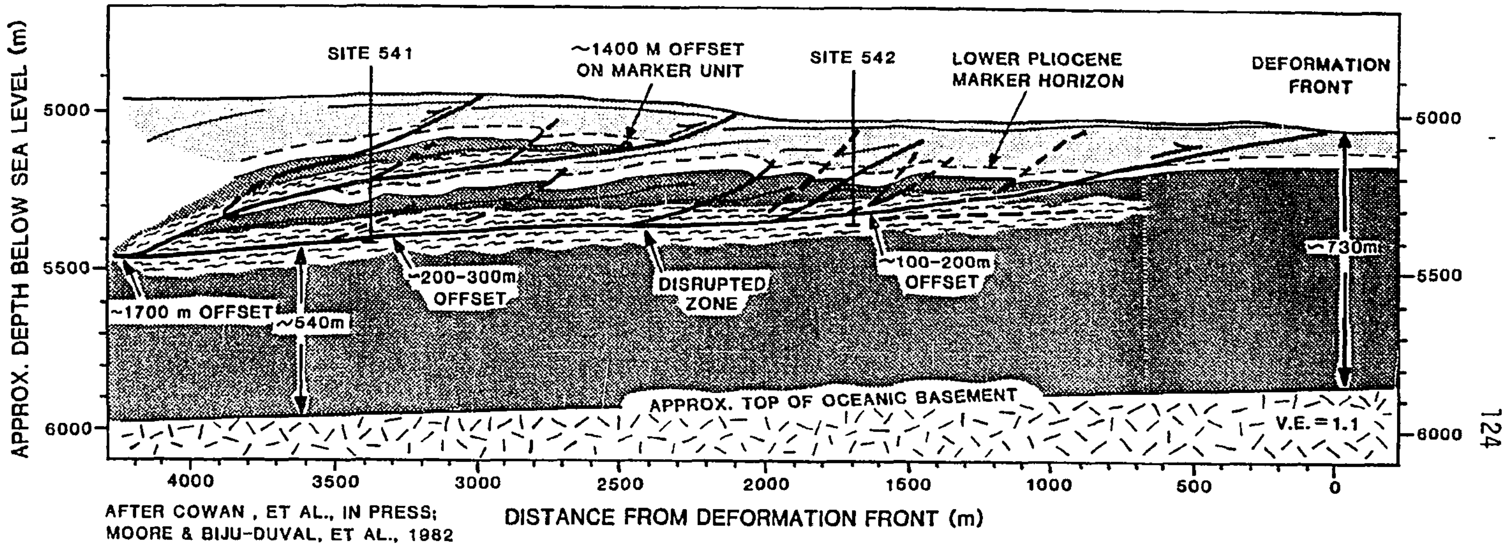

Figure 33. Cross section of lower trench slope at DSDP sites 541 and 542 in the Barbados Ridge Complex (after Figure 1 in Cowan, et al., in press; and also Moore, Biju-Duval, et al., 1982). Drilling at site 541 identified a major thrust fault that offsets the Lower Pliocene horizon and has about 1400 m of dip-slip displacement. Disrupted sediments, which are designated by a wavy pattern, are located in the hanging wall of this thrust and were probably deformed within the decollement zone, which was intersected at the base of sites 541 and 542.

on stratigraphic repetition, at least six thrust faults have been identified. Drilling also encountered two disrupted zones (indicated by the wavy pattern in Figure 33), which are characterized by a semi-penetrative fabric that ranges from closely spaced, slickensided slip surfaces, to a scaly foliation (Cowan, et al., in press). Sediments outside of these zones are generally undeformed, and have gentle to horizontal dips. The disrupted zone sampled at the base of sites 541 and 542 is presumably associated with a major decollement recognized in seismic profiles (Moore, Biju-Duval, et al., 1982), and also appears to be a region of high pore pressure, as determined when the hole at the base of site 542 was accidentally packed off (Moore, Biju-Duval, et al., 1982). The second disrupted zone is about 60 m thick and is located above a major thrust fault, midway down the hole at site 541. The important feature of this disrupted zone is that it is entirely confined to sediments in the hanging wall of the thrust fault. The fault itself occurs as a discrete surface, and therefore marks a major break in stratigraphy and structural fabric. Based on offsets of a Lower Pliocene marker horizon (Figure 33), this thrust fault has a dip-slip displacement of about 1400 m, which is much greater than the displacements associated with the decollement zone at sites 541 and 542 (approximate displacements are shown in Figure 33).

These relations suggest that the disrupted zone above the major thrust at site 541 was formed within the decollement zone, and then was ramped upward along a discrete fault, as shown in Figure 34. In this interpretation, the decollement zone at sites 541 and 542 is viewed as a zone of distributed shear, characterized by a Type 2 structural style. The scaly fabric developed within the disrupted decollement zone is evidence that much of the deformation in this zone occurs after the sediments have reached stable failure. At this stage, a discrete fault has apparently not formed yet. The next stage involves localization and formation of a discrete thrust fault. Since this thrust fault originates within the disrupted decollement zone,

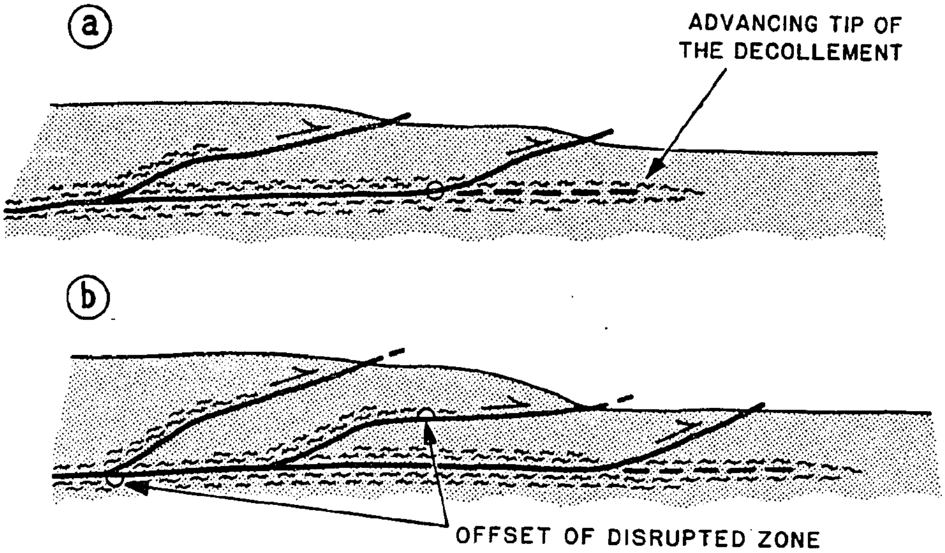

Figure 34. Cross-sections illustrating an interpretation for the sequential development of structures at the Barbados drilling transect (compare with Figure 34). According to this interpretation, the frontal portion of the decollement zone propagates forward through a thick, distributed shear zone, characterized by a Type 2 structural style (indicated by the wavy pattern in Figure 35). A discrete thrust fault eventually forms within this disrupted decollement zone, which causes the hanging wall portion of the zone to be ramped upward; whereas, the footwall portion is underthrust to deeper levels (Figure 35b).

the hanging wall portion of the zone is carried forward to higher levels, while the footwall portion is underthrust to deeper levels (Figure 34).

The question that remains unaddressed is: Why does the deformation become localized? Preliminary analyses indicate that the clay mineralogy at site 541 is significantly different from stratigraphically equivalent sediments at site 542 and a more seaward site 543 (J. Schoonmaker, pers. comm., 1984). These data suggest, but do not prove, the possibility of incipient lithification as the process responsible for localization. For instance, a small reduction in void ratio caused by a pore-filling clay cement could transform these sediments into overconsolidated muds. Textural studies of less deformed mud from the area surrounding the thrust fault should be able to test this possibility.

These drilling results have two important implications: (1) The presence of thick zones of scaly mud indicates that the Type 2 structural style is actually developed in a modern subduction zone. (2) The recognition of discrete thrust faults suggests that these structures are developed in concert with the Type 2 structures, and that the overall structural style actually may be more of a composite of Type 2 and Type 3 styles. Apparently these discrete faults can develop within several kilometers of the leading edge of the subduction zone, and can thereafter accommodate significant amounts of displacement across the zone.

IMPLICATIONS FOR DEEPER LEVEL STRUCTURES

If much of the deformation within a subduction zone is accommodated by discrete faults, which is a possibility considered in this paper, then the geometry and structure of on-land thrust systems should serve as a guide to deeper level structures within the accretionary wedge. Seismic profiles across several modern accretionary wedges indicate that a substantial portion of the sedimentary sequence on the downgoing plate is not accreted at the front of the wedge, but is carried beneath the wedge some uncertain distance (Westbrook, et al., 1982; Moore, Biju-Duval, et al., 1982; Aoki, et al., 1982). For instance, at the Barbados Ridge complex, only 50% of the incoming section is accreted at the lower trench slope (Figure 34) with the remaining 50% carried at least 75 km rearward beneath the accretionary wedge (Westbrook, et al., 1982). A number of authors (Scholl, et al., 1980; Von Huene and Uyeda, 1981; Moore; et al.; 1982; Karig, 1983) suggest that at least some of these subducted sediments are accreted to the base of the wedge by a poorly understood process called underplating or subcretion.

The main point I want to make here is that underplating also occurs in on-land thrust belts and is associated with the development of duplex structures (Boyer and Elliott, 1982; Butler, 1982). A duplex consists of an imbricated package of thrust slices, which is underlain by an active floor thrust, or decollement, and is overlain by an inactive roof thrust (see Figure 35 which is adapted from Figure 19 in Boyer and Elliott, 1982). Each imbricate slice is derived by failure of the decollement ramp beneath the duplex. Slices of the footwall beneath these ramps are accreted to the base of the growing duplex; older slices are folded and displaced upward from the active decollement.

Figure 36 schematically illustrates a duplex interpretation for underplating beneath an accretionary wedge. Karig (1983) notes that subduction-related displacement within modern accretionary wedges is largely confined to the base of the wedge, because the upper slope and shelf region are commonly blanketed with a relatively undisrupted sediment cover or slope apron (Figure 19). The duplex model is in accord with this observation, since subduction displacement occurs solely along the basal decollement, and imbrication and accretion are confined to this basal zone. Deformation is probably confined to this zone because of large excess pore pressures (cf. Gretener, 1972). Sediments on the downgoing plate are subjected to a continually increasing load because of the wedge-shaped profile of the overriding accretionary wedge. As a slice is accreted from the footwall of the decollement, it is no longer subjected to this increasing load.

Figure 35. An idealized example of the progressive growth of a duplex (after Figure 19 in Boyer and Elliott, 1982). The hanging wall is held fixed in order to provide a more familiar, subduction-zone viewpoint where the downgoing plate is underthrust beneath the accretionary wedge. Each sequential ramp is labelled R_i; L_o is the original length of the imbricated horizon and L' is its deformed length. S represents the amount of total thrust displacement. The imbricated horizon has a thickness of t and the height of the resulting duplex is H'. Note that the footwall ramp moves forward with respect to the hanging wall, while the footwall itself is underthrust rearward. In this case, the footwall and the footwall ramp move at the same rates (S=L') but in opposite directions.

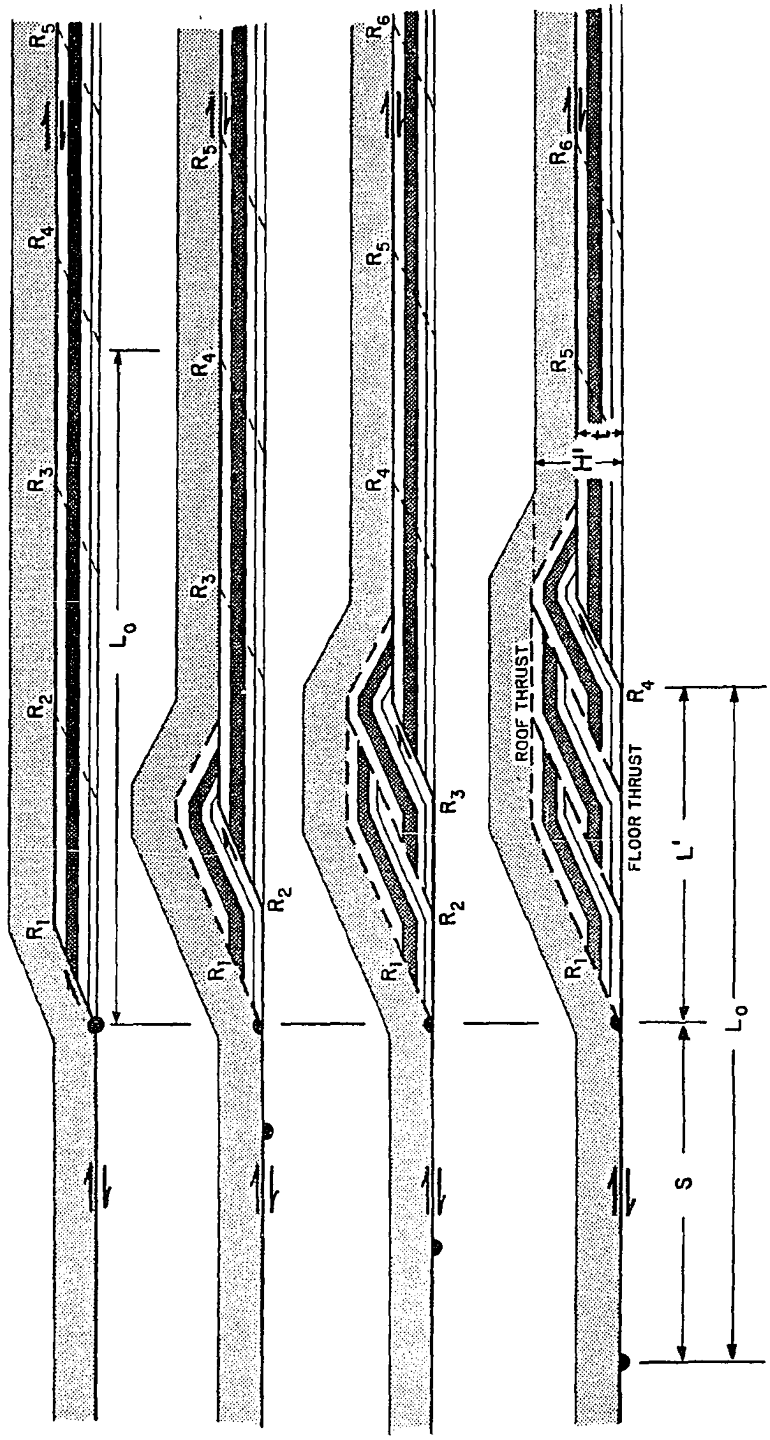

R1
R2
R3
R4
R5
R6
Lo
ROOF THRUST
FLOOR THRUST
L'
H'
t
S

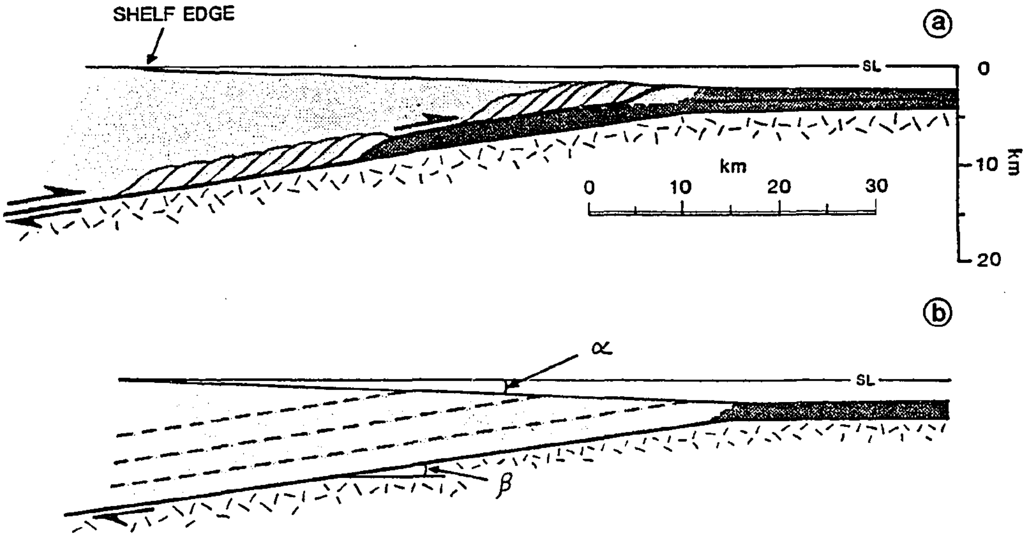

Figure 36. A duplex model for underplating in an accretionary wedge. As shown in Figure 37a, accretion occurs by offscraping at the front of the wedge, and also by duplex-related imbrication beneath the wedge. Imbrication associated with the forward movement of a decollement ramp results in the accretion of a relatively uniform layer of material to the base of the wedge. An idealized example of this is shown in Figure 37b, where the layers are indicated by dashed lines. This process allows the wedge to maintain a constant wedge taper, which according to Davis, et al.,(1983) is an attribute of a steady-state accretionary wedge. The taper of the wedge is defined by the forward-dipping surface slope (α) and the rearward-dipping decollement (β).

Excess pore pressure within the slice can begin to decrease, so that the duplex remains somewhat stronger than the underthrusted sedimentary section. As a result, continued imbrication should be restricted to the overpressured sediments beneath the decollement.

Another aspect of the duplex model is that the tapered profile of the wedge--defined by the forward-dipping surface slope (α) and the rearward-dipping decollement (β)--remains fairly constant as it grows. Imbrication and accretion cause the front of the duplex to move forward with time. This process, together with imbrication at the front of the wedge, allows material to be uniformly delivered to the base of the wedge. The net effect is that the duplex model as shown in Figure 36a can closely approximate the idealized geometry shown in Figure 36b without requiring significant internal deformation within the wedge. According to the thrust wedge model of Davis, et al. (1983), this constant wedge taper, which they call a critical taper angle, is an attribute of a steady-state accretionary wedge.

In actuality, the subduction zone decollement might have several ramps and associated duplexes. Other, more complex variations on this theme might include: (1) the initiation of a new duplex by formation of a ramp in the decollement, or (2) the deactivation of a duplex due to the gradual replacement of a decollement ramp with a flat fault. Despite these variations, two important aspects of the model remain: (1) subduction-related deformation is largely concentrated to the base of the wedge, and (2) the structural style of the entire wedge--not just the frontal part--is characterized by imbricate thrust slices.

SUMMARY AND CONCLUDING REMARKS FOR PART II

This paper considers some of the general aspects of sediment deformation with a special emphasis on those factors that might affect the structural style of sediment in a subduction-zone setting. In particular, this analysis examines the deformational stability of an idealized elastic-plastic sediment (represented by the modified Cam Clay model) when subjected to homogeneous deformation. Since sediments within a subduction shear zone are subjected to very large shear strains (Figure 20), much of the deformation must occur after failure. As a result, the structural style of subduction zone sediments should be most significantly influenced by the mode of failure of sediments, i.e., stable failure or rupture failure.

In the analysis above, there appear to be three factors that affect the behavior of homogeneously deforming sediments (Table 4): the consolidation state, the drainage conditions and the stress path. Of these factors, the consolidation state is the primary factor controlling the mode of failure; as a result, it also has a strong influence on the structural style of deformation at the subduction zone. The effect of the consolidation state is summarized below.
(1) Normally consolidated sediments (looser-than-critical) fail by stable failure with no significant loss-of-strength. Because continued deformation occurs in a neutrally stable fashion, there is no strong tendency for deformation to become localized. To my knowledge there are no published accounts of the structural style associated with deformation after stable failure. I suspect, however, that with large shear strains, real clays probably develop wide scaly zones, characterized by closely spaced slip surfaces (Type 2 in Figure 21). The reason is that, given the neutrally stable condition that prevails after stable failure, further deformation is more easily perturbed by local variations in material properties; thus, slip surfaces are likely to form. However, since these newly formed slip surfaces are

not significantly weaker than the surrounding sediment, there is no strong tendency for large strains to become concentrated at a specific slip surface. This situation should favor the development of many small slip surfaces, each accommodating a small amount of deformation. This interpretation is consistent with the results of DSDP Leg 75A at the Barbados drilling transect where wide scaly zones are apparently developed prior to the formation of a discrete thrust fault (Figure 34).

(2) Highly overconsolidated sediments (denser-than-critical) exhibit a pronounced loss-of-strength after peak strength, and are characterized by rupture failure. The unstable, strain-softening behavior of these sediments results in a marked tendency for deformation to become localized into narrow zones which evolve into discrete fault surfaces. Given that these fault surfaces are weaker than the surrounding unfailed sediment, they should accommodate further deformation until they are rotated into an unfavorable orientation for slip. Highly overconsolidated sediments in a subduction shear zone, such as depicted in Figure 20, are therefore expected to develop a Type 3 structural style (Figure 21) characterized by widely spaced faults which have accommodated the bulk of the deformation. Furthermore, a larger loss-of-strength at failure should result in a more widely spaced system of faults.

Another important conclusion is that this fundamental deformational behavior--strain-hardening and stable failure vs. strain-softening and rupture failure--appears to be unaffected by the development of load-induced excess pore-pressure (see Figure 30). Poor drainage conditions and the associated development of load-induced excess pore pressure does affect the subsidiary aspects of sediment deformational behavior. For instance, when compared with drained deformation, partially drained and totally undrained deformation is characterized by: (1) a reduction in the amount of ductile strain before failure, and (2) a decrease in shear strength at failure.

Another important conclusion is that the loading conditions at a subduction-zone setting apparently cannot transform a normally consolidated sediment into a highly overconsolidated state. For instance, if sediments on the down-going plate are normally consolidated (i.e., looser-than-critical) prior to subduction, then the expected mode of deformation should be that of strain-hardening and stable failure (schematically illustrated by the stress paths E-T and E-O in Figure 32). As a result, the development of discrete faults is not expected in normally consolidated sediments. This conclusion is at odds with the fact that discrete faults are observed in the frontal region of modern accretionary complexes where sediments are young and presumably normally consolidated (e.g., see Aoki, et al., 1982; Moore, Biju-Duval, et al., 1982).

As a result, the sediment plasticity model does not clearly indicate what causes faults to form within subduction-zone sediments. Two geological processes, however, are proposed as possible candidates: (1) the internal generation of excess pore fluid pressure due to devolatization reactions, and (2) lithification and cementation. Both of these processed can transform a normally consolidated sediment into a more overconsolidated state, and therefore account for the formation of discrete faults. The first process actually "unloads" the sediment by causing a reduction in the effective pressure. As schematically illustrated in Figure 32 (stress path E-U), this process can cause the stress path to move inside the current yield surface, thereby resulting in an overconsolidated state. Subsequent plastic deformation would involve strain softening or rupture failure. It is important to distinguish this process from that occurring during undrained deformation of normally consolidated sediments (e.g., see Figure 28). In this case, the undrained stress path will also curve to the left, but it will always be directed outward from the current yield surface, as long as the applied load continues to increase.

High excess pore pressures have been detected (Moore, Biju-Duval, et al., 1982) and inferred (Davis, et al., 1983; Von Huene and Lee, 1982) at several modern accretionary wedges, but the origin of these high pore-pressures-- whether load-induced or internally generated--is not known. If devolatization reactions do generate a significant amount of excess pore-pressure in subduction zone settings, then this process may be responsible for localization of discrete faults.

The other process--lithification and cementation--results in a reduction of pore volume and an increase in the strength of the granular aggregate. In a review of the stress-stain behavior of cemented sediments, Mitchell (1976) indicates that these sediments exhibit a significant loss-of-strength at failure, which is a feature that also characterized highly overconsolidated sediments. Evidently, the cementation process changes the material properties of the sediment so that its deformational behavior is no longer represented by the "invariant" material constants used in the model. Nonetheless, the loss-of-strength after peak strength suggests that cemented sediments probably fail by rupture failure. This conclusion is not unexpected since the lithification process gradually transforms a sediment into a lithified rock, which at low temperature will also fail by rupture failure. Cementation and lithification can certainly be expected to affect sediments at a subduction-zone setting; however, the complexities of the process make it difficult to predict rates and modes of occurrence. Furthermore, to my knowledge, the study of lithificational processes at subduction zone settings has received very little attention (a notable exception is the work of J. Schoonmaker [pers. comm., 1984] on the mineralogy of clays from the Barbados drilling transect). These processes deserves closer scrutiny, given its effect on deformational behavior and structural styles at subduction zone settings.

BIBLIOGRAPHY

Abbey, S., 1977. Studies in "Standard Samples" for use in the general analysis of silicate rocks and minerals, part 5; 1977 edition of "usable" values. Geological Survey of Canada Paper 77-34.

Allen, J.R.L., 1982. Sedimentary structures, their character and physical basis, volume 2. Elsevier Science Publication Company, New York, 663p.

Andresen, A., and Bjerrum, L., 1967. Slides in subaqueous slopes. In Marine Geotechnique. Edited by A.F. Richards. University of Illinois Press, Urbana, p.221-239.

Aoki, Y.,Tamano, T., and Kata, S., 1983. Detailed structure of the Nankai trough from migrated seismic sections. In Studies in continental margin geology. American Association of Petroleum Geologists, Memoir 34, pp.309-322.

Atkinson, J.H., and Bransby, P.l., 1978. The mechanics of soils: an introduction to critical state soil mechanics. McGraw-Hill, London, 375p.

Bachman, S.B.,1978. A Cretaceous and early Tertiary subduction complex, Mendocino, northern California. In Mesozoic Paleogeography of the western United States. Edited by D.G. Howell and K.A. McDougall. Society of Economic Paleontologists and Mineralogists, Pacific Section, pp. 117-132.

Beck, R.H., 1972. The oceans, the new frontier in exploration. Australian Petroleum Exploration Association Journal **12**, pp.1-21.

Bishop, A.W., and Henkel, D.J., 1962. The measurement of soil properties in the triaxial test. Edward Arnold Ltd., London, 228p.

Boyer, S.E., and Elliot, D., 1982. Thrust systems. American Association of Petroleum Geologists Bulletin, **66**, pp.1196-1230.

Brandon, M.T., 1980. Structural geology of middle Cretaceous thrust faulting on southern San Juan Island, Washington. M.S. thesis, University of Washington, Seattle, WA, 130p.

Brandon, M.T., 1982. Mid-Cretaceous high-pressure regional metamorphic event in the San Juan Islands, Washington; Evidence for rapid structural burial and uplift. Geological Society of America Abstracts with Programs, **14**, pp.152.

Brandon, M.T., and Cowan, D.S., 1983. Mesozoic terrane convergence and dispersion within the Fraser block, Pacific Northwest. Geological Society of America, Abstracts with Programs, **15**, pp.295.

Brandon, M.T., Cowan, D.S., Muller, J.E., and Vance, J.A., 1983. In Pre-Tertiary geology of San Juan Islands, Washington, and southeast Vancouver Island, British Columbia. Fieldtrip Guidebook Trip 5 Annual Meeting, Geological Association of Canada, Victoria, British Columbia, pp.4-29.

Brown, E.H., Bradshaw, J.Y., and Mustoe, G.E., 1979. Plagiogranite and Keratophyre in ophiolite on Fidalgo Island, Washington. Geological Society of America Bulletin, Part I, **90**, pp.493-507.

Brun, T.R., 1983. Models for the origin of the Yakutat block, an accreting terrane in the northern Gulf of Alaska. Geology, **11**, pp.718-21.

Brune, J.N., 1968. Seismic moment, seismicity and rates of slip along major fault zones. Journal of Geophysical Research, **73**, pp.777-784.

Busch, W.H., and Keller, G.H., 1981. The physical properties of Peru-Chile continental margin sediments--the influence of coastal upwelling on sediment properties. Journal of Sedimentary Petrology, **51**, pp.705-719.

Butler, R.W.H., 1982. The terminology of structures in thrust belts. Journal of Structural Geology, **4**, pp.239-245.

Butler, R.W.H., 1983. Hanging wall strain: a fuction of duplex shape and footwall topography. Tectonphysics, **88**, pp.235-246.

Byrne, T., in press. Structural geology of melange terranes in the Ghost Rocks Formation, Kodiak Islands, Alaska. In preparation. Edited by L.A. Raymond. Geological Society of America Special Paper.

Byrne,T., 1982. Structural evolution of coherent terranes in the Ghost Rocks Formation, Kodiak Island, Alaska. In Trench-forearc geology: sedimentation and tectonics on modern and ancient active plate margins. Edited by J.K. Leggett. Geological Society of London. Special Publication 10, pp.229-242.

Carson, D.J.T. 1973. The plutonic rocks of Vancouver Island, British Columbia: their petrography, chemistry, age, and emplacement. Geological Survey of Canada, Paper 72-44.

Carter, J.P., 1982. Predictions of the non-homogeneous behavior of clay in the triaxial test. Geotechnique **32**, pp.55-58.

Carter, J.P., Brooker, J.R., and Wroth, C.P., 1982. A critical state soil model for cyclic loading. In Soil mechanics--transient and cyclic loads. Edited by G.N. Pande and O.C. Zienkiewicz. John Wiley and Sons, New York, pp.219-252.

Casagrande, A., 1936. Characteristics of cohesionless soils affecting the stability of slopes and earth fills. Journal of Boston Society of Civil Engineers, pp.257-276.

Castro, G., 1975. Liquefaction and cyclic mobility of saturated sands. Journal of the Geotechnical Engineering Division, American Society of Civil Engineering, **101**, pp.551-569.

Castro, G., and Poulos, S.J., 1977. Factors affecting liquefaction and cyclic mobility. Journal of the Geotechnical Engineering Division, American Society of Civil Engineering, **103**, pp.501-516.

Cloos, M., 1982. Flow melanges: numerical modeling and geologic constraints on their origin in the Franciscan subduction complex, California. Geological Society of America Bulletin **93**, pp.330-345.

Coleman, R.G. 1977. Ophiolites. Springer-Verlag, Berlin, pp.1-229.

Coulbourn, W.T., 1982. Introduction, summary and explanatory notes, the Middle America trench transect, Deep Sea Drilling Project Leg 67. In Initial Reports of the Deep Sea Drilling Project, Edited by J. Aubouin, R. VonHuene, et. al. U.S. Government Printing Office, Washington **67**, pp.5-25.

Cowan, D.S.,1982a. Geologic evidence for post-40 m.y. B.P. large-scale northwestward displacement of part of southeastern Alaska. Geology, **10**, pp.309-313.

Cowan, D.S.,1982b. Deformation of partly dewatered and consolidated Franciscan sediments near Piedras Blancas Point, California. In Trench-forearc geology: sedimentation and tectonics on modern and ancient active plate margins. Edited by J.K. Leggett. Geological Society of London, Special Publication number 10, pp.439-457.

Cowan, D.S., in press. Structural styles in Mesozoic and Cenozoic melanges in the western Cordillera of North America. Geological Society of America Bulletin.

Cowan, D.S., Moore, J.C., Roeske, S.M., and Lundberg, N., in press. Structural features at the deformation front of the Barbados Ridge Complex, DSDP leg 78A. In Initial Reports of the Deep Sea Drilling Project. U.S. Government Printing Office, Washington, **78**.

Cowan, D.S., and Brandon, M.T., 1981. Contrasting facies in Upper Mesozoic strata of Pacific Northwest (abstract). American Association of Petroleum Geologists Bulletin **65**, pp.913-914.

Davis, D., Suppe, J., and Dahlen, F.A., 1983. Mechanics of fold-and-thrust belts and accretionary wedges. Journal of Geophysical Research, **88**, pp.1153-1172.

Dickinson, W.R., 1976. Sedimentary basins developed during evolution of Mesozoic-Cenozoic arc-trench system in western North America. Canadian Journal of Earth Science, **13**, pp.1268-1287.

Drucker, D.C., 1966. Concept of path independence and material stability for soils. In Proccedings of the International Symposium of Rheology and Soil Mechanics in Grenoble, 1964. Springer-Verlag, New York, pp.23-46.

Dymond, J., 1981. Geochemistry of Nazca plate surface sediments: An evaluation of hydrothermal, biogenic, detrital and hydrogenous sources. Geological Society of America Memoir 154, pp.133-173.

Egan, J.A., and Sangrey, D.A., 1978. Critical state model for cyclic load pore pressure. In Earthquake engineering and soil dynamics, volume 1. Proceedings of the American Society of Civil Engineering, Geotechnical Engineering Division, Special Conference,**1**, pp. 410-424.

Fairchild, L.H., and Cowan, D.S., 1982. Structure, petrology and tectonic history of the Leech River Complex, northwest of Victoria, Vancouver Island. Canadian Journal of Earth Science, **19**, pp.1816-1835.

Field, M.E., and Edwards, B.D., 1980. Slopes of the southern California continental borderland: a regime of mass transport. In Quaternary depositional enviornments of the Pacific Coast. Edited by M.E. Field, A.H. Bouma, I.P. Colburn, R.G. Douglas, and J.C. Ingle. Society of Economic Paleontologists and Mineralogists Pacific Section, pp.169-184.

Field, M.E., Gardner, J.V., Jenning, A.E., Edwards, B.D., 1982. Earthquake-induced sediment failures on a 0.25° slope, Klamath River Delta, California. Geology, **10**, pp.542-546

Fukushima, S., and Tatsuoka, F., 1982. Deformation and strength of sand in tortional simple shear. In Proccedings of the IUTAM conference on deformation and failure of granular materials. Delft, 31 Aug-3 Sept, 1982, pp. 371-379.

Garcia, M.O., 1978. Criteria for the identification of ancient volcanic arcs. Earth Science Reviews, **14**, pp.147-165.

Glassley, W.E., Whetten, J.T., Cowan, D.S., and Vance, J.A., 1976. Significance of coexisting lawsonite, prehnite, and aragonite, in the San Juan Islands, Washington. Geology, **4**, pp.301-302.

Gorsline, D.S., and Emery K.O., 1959. Turbidity-current deposits in San Pedro and Santa Monica Basins off southern California. Geological Society of America Bulletin, **70**, pp.279-290.

Gretner, P.E., 1972. Thoughts on overthrust faulting in a layered sequence. Bulletin Canadian Petroleum Geology, **20**, pp.583-607.

Guth, P.L., Hodge, K.V., and Willemin, J.H., 1982. Limitations on the role of pore pressure in gravity gliding. Geological Society of America Bulletin, **19**, pp.606-612.

Hamilton E.L., 1976. Variations of density in deep-sea sediments. Journal of Sedimentary Petrology, **47**, pp.280-300.

Hansen, E., 1971. Strain Facies. Springer-Verlag, New York, 207p.

Harland, W.B., Cox, A.V., Llewellyn, P.G., Pickerton, C.A.G., Smith, A.G., and Walters, R., 1982. A Geologic Time Scale. Cambridge University Press, Cambridge. 131p.

Hawkins, J.W., 1980. Petrology of back-arc basins and island arcs: their possible role in the origin of ophiolites. In Ophiolites. Proceedings from the International Ophiolite Symposium, Cyprus Geological Survey Department.

Heath, G.R., and Dymond, J., 1977. Genesis and diagenesis of metalliferous sediments from the East Pacific Rise, Bauer Deep and Central Basin, northwest Nazca plate. Geological Society of America Bulletin, **88**, pp.723-733.

Hedberg, H.D., 1974. Relation of methane generation to undercompacted shales, shale diapirs and mud volcanoes. American Association of Petroleum Geologists Bulletin, **58**, 661-673.

Hekinian, R.,1982. Petrology of the Ocean Floor. Elsevier Science Publication Company, New York, 393p.

Helwig, J., 1970. Slump folds and early structures, northeastern Newfoundland Appalachians. Journal of Geology, **78** pp.172-187.

Hoedemaeker, Ph.J., 1973. Olistostromes and other delapsional deposits, and their occurrence in the region of Movatalla (province Murica, Spain). Scripta Geologica, **19**, 207p.

Hsu, K.J., 1967. Origin of large overturned slabs of Apennines, Italy. American Association of Petroleum Geologists Bulletin, **51**, pp.65-72.

Hsu, K.J., 1968. Principles of melanges and their bearing on the Franciscan-Knoxville paradox. Geological Society of America Bulletin, **79**, pp.1063-1074.

Irving, E. and Yole, R.W., 1972. Paleomagnetism and the kinematic history of mafic and ultramafic rocks in fold mountain belts. In The ancient oceanic lithosphere. Edited by E. Irving. Department of Energy, Mines,and Resources, Earth Physics Branch Publications, Ottawa, **42**, pp.87-95.

Isachsen, C.E., 1984. Geochronology and geochemistry of West Coast Crystalline Complex and related rocks. (Abstract). Programme and Abstracts, Meeting of the Geological Association of Canada, Victoria Section (April, 1984), pp.11.

Jablonski, D., and Bottjer, D.J., 1983. Soft-bottom epifaunal suspension-feeding assemblages in the Late Cretaceous--Implications for the evolution of Benthic paleocommunities. In Biotic interaction in recent and fossil benthic communities. Edited by M.J.S. Tevesz and P.L. McCall. Plenum Publishing Company, New York

Jain, S.K., 1980. Fundamental aspects of the normality rule and their role in deriving constitutive laws of soils. Engineering Publications, Blackburg, Virginia, 168p.

Jaky, J., 1944. The coefficient of earth pressure at rest (in Hungarian). Journal of the Society of Hungarian Architects and Engineers, pp.355-358.

Jenkyns, H.C. and Winterer, E.L., 1982. Paleoceanography of Mesozoic ribbon radiolarites. Earth and Planetary Sciences Letters, **6**, pp.351-375.

Johnson, H.D., 1978. Shallow siliclastic seas. In Sedimentary enviornments and facies. Edited by H.G. Reading. Elsevier Science Publications Company, New York, pp.207-258.

Jones, D.L., Silberling, N.J., and Hillhouse, J., 1977. Wrangellia--a displaced terrane in northwestern North America. Canadian Journal of Earth Science, **14**, pp.2565-2577.

Kanamori, H., 1977. Seismic and aseismic slip along subduction zones and their tectonic implications. In Island arcs, deep sea trenches, and back-arc basins. Edited by M.Talwani and W.C. Pitman III. American Geophysical Union, pp.163-174.

Karig, D.E., 1971. Origin and development of marginal basins in the Western Pacific. Journal of Geophysical Research, **76**, pp.2542-2561.

Karig, D.E., 1974. Evolution of arc systems in the western Pacific. Annual Reviews of Earth and Planetary Sciences, **2**, pp.51-75.

Karig, D.E., 1983. Deformation in the forearc: implication for mountain belts. In Mountain building processes. Edited by K.J. Hsu. Academic Press, New York, pp. 59-71.

Karig, D.E., and Moore, G.F., 1975. Tectonically controlled sedimentation in marginal basins. Earth and Planetary Science Letters, **26**, pp.233-238.

Karig, D.E., Moore, G.F., Curray, J.R., and Lawerence, M.B., 1980. Morphology and shallow structure of the lower trench slope off Nias Island, Sunda Arc. In Tectonic and geologic evolution of southwest Asian seas and islands. Edited by D.E. Hayes. American Geophysical Union, Geophysical Monograph 23, pp.179-208.

Karig, D.E., Kagami, H., and DSDP Leg 87 Scientific Party, 1983. Varied responses to subduction in Nankai Trough and Japan Trench forearcs. Nature, **304**, pp.148-151.

Karl, S.M., 1982. Geochemical and depositional environments of Upper Mesozoic radiolarian cherts from the northeastern Pacific Rim and from Pacific DSDP cores. Ph.D. dissertation, Stanford University, Palo Alto, CA, 245p.

Kauffman, E.G., Hattin, D.E., and Powell, J.D., 1977. Stratigraphic, paleontologic and paleoenvironmental analyses of the Upper Cretaceous rocks of Cimarron County, northwestern Oklahoma. Geological Society of America Memoir 149, 150p.

Kelleher, J., Savino, J., Rowlett, H., and McCann, W., 1974. Why and where great thrust earthquakes occur along island arcs. Journal of Geophysical Research, **79**, pp.4889-4999.

Keller, G.H., Lambert, D.N., and Bennett, R.H., 1979. Geotechical properties of continental slope deposits--Cape Hatteras to Hydrographer Canyon. In Geology of continental slopes. Edited by L.J. Doyle and O.H. Pilkey Jr. Society of Economic Paleontologists and Mineralogists, Special Publication 27, pp.131-151.

Ko, Hon-Yim, and Sture, Stein, 1981. State of the art: data reduction and application for analytical modeling. In Laboratory shear strength of soils, ASTM STP 740. Edited by R.N. Yong, and F.C. Townsend. American Society for Testing and Materials, pp.329-386

Kraft, L.M., Campbell, K.J., and Ploessel, M.R., 1979. Some geotechnical engineering problems of upper slope sites in the northern Gulf of Mexico. In Geology of continental slopes. Edited by L.J. Doyle and O.H. Pilkey Jr.. Society of Economic Paleontologists and Mineralogists, Special Publication 27, pp.25-42.

Lade, P.V., 1982. Localization effects in triaxial tests on sand. In Proceedings of the IUTAM Conference on Deformation and Failure of Granular Materials, Delft, 31 Aug-3 Sept 1982, pp.461-471.

Lambe, T.W., and Whitman, R.V., 1979. Soil mechanics, SI version. John Wiley and Sons, New York, 553p.

Leggett, J.K., McKerrow, W.S., and Casey, D.M., 1982. The anatomy of a Lower Paleozoic accretionary forearc: the Southern Uplands of Scotland. In Trench-forearc geology: sedimentation and tectonics on modern and ancient active plate margins. Edited by J.K. Leggett. Geological Society of London Special Publication 10, pp.495-520.

Liou, J.G., 1976. P-T stabilities of laumontite, wairakite, lawsonite, and related mineral in the system CA $Al_2Si_2O_8$-SiO_2-H_2O. Journal of Petrology, **12**, pp.379-411.

Lockner, D. and Byerlee, J.D., 1977. Hydrofracture in Weber sandstone at high confining pressure and differential stress. Journal of Geophysical Research, **82**, pp.2018-2026.

Lowe, D.R., 1975. Water escape structures in coarse-grained sediments. Sedimentology, **22**, pp. 157-204.

Lowe, D.R., 1976. Subaqueous liquefied and fluidized sediment flows and their deposits. Sedimentology, **23**, pp.285-308.

MacLeod, N.S., Tiffin, D.L., Snavely, P.D. Jr., and Currie, R.G., 1977. Geologic interpretations of magnetic and gravity anomolies in the Strait of Juan de Fuca, U.S.-Canada. Canadian Journal of Earth Science, **14**, pp.223-238.

Mayne, P.W., and Kulhawy, F.H., 1982. K_o in soil. Journal of the Geotechnical Engineering Division, Proceedings of the American Society of Civil Engineering, **108**, pp.851-872

Mitchell, J.K., 1976. Fundamentals of soil behavior. John Wiley and Sons, New York, 422p.

Moore, G.F., and Karig, D.E., 1980. Structural geology of Nias Island, Indonesia: implication for subduction zone tectonics. American Journal of Science, **280**, pp.193-223.

Moore, J.C.,and Karig, D.E., 1976. Sedimentology, structural geology and tectonics of the Shikoku subduction zone, southwestern Japan. Geological Society of America Bulletin, **87**, pp.1259-1268.

Moore, J.C., and Wheeler, R.L., 1978, Structural fabric of a melange, Kodiak Islands. American Journal of Science, **278**, pp.739-765.

Moore, J.C., and Allwardt, A., 1980. Progressive deformation of a Tertiary trench slope, Kodiak Islands, Alaska. Journal of Geophysical Research, **85**, pp.4741-4756.

Moore, J.C.,Biju-Duval, B., et al., 1982. Offscraping and underthrusting of sediment at the deformation front of the Barbados Ridge: Deep Sea Drilling Project Leg 78A. Geological Society of America Bulletin, **93**, pp.1065-1077.

Moore, J.C., Watkins, J.S., Shipley, T.H., McMillen, K.J., Bachman, S.B., and Lundberg, N., 1982. Geology and tectonic evolution of a juvenile accretionary terrane along a truncated convergent margin: synthesis of results from Leg 66 of the Deep Sea Drilling Project, southern Mexico. Geological Society of America Bulletin, **93**, pp.846-861.

Moore, J.C., Byrne, T., Plumley, P.W., Reid, M., Gibbons, H., and Coe, R.S., 1983. Paleogene evolution of the Kodiak Islands, Alaska: consequences of ridge-trench interaction in a more southerly latitude. Tectonics, **2**, pp.265-293.

Muller, J.E., 1973. Geology of Pacific Rim National Park. Geological Survey of Canada, Paper 73-1A, pp. 29-37.

Muller, J.E., 1976. Cape Flattery map-area (92C), British Columbia. Geological Survey of Canada, Paper 76-1A, pp.107-112.

Muller, J.E., 1977a. Evolution of the Pacific margin, Vancouver Island, and adjacent regions. Canadian Journal of Earth Science, 14, pp.2062-2085.

Muller, J.E., 1977b. Geology of Vancouver Island. Geological Survey of Canada, Open File Map 463.

Muller, J.E., 1980. Geology, Victoria map area. Geological Survey of Canada, Open File Map 701.

Muller, J.E., Northcote, K.E., and Carlisle, D., 1974. Geology and mineral deposits of Alert-Cape Scott map-area, Vancouver Island, British Columbia. Geological Survey of Canada, Paper 74-8, 77p.

Muller, J.E., Cameron, B.E.B., and Northcote, K.E., 1981. Geology and mineral deposits of Nootka Sound Map-area Vancouver Island, British Columbia. Geological Survey of Canada, Paper 80-16, 53p.

Mutti, E., and Ricci-Lucchi, R., 1978. Turbidites of the northern Apennines: introduction to facies analysis. Translated by T.H. Nilsen International Geologic Review, **78**, pp.125-166 .

Naylor, M.A., 1982. The Casanova Complex of the northern Apennines: a melange formed on a distal passive continental margin. Journal of Structural Geology. **4**, pp.1-18.

Page, B.M., and Suppe, J., 1981. The Pliocene Lichi melange of Taiwan: its plate tectonic and olistromal origin. American Journal of Science, **281**, pp.193-227.

Page, R.J., 1974. Sedimentology and tectonic history of the Esowista and Ucluth Peninsulas, west coast, Vancouver Island, British Columbia. Ph.D. dissertation, University of Washington, Seattle, WA, 72p.

Palmer, A.C., and Rice, J.R., 1973. The growth of slip surfaces in the progressive failure of over-consolidated clay. Proceedings of the Royal Society of London, **A 332**, pp.527-548.

Pearce, J.A., and Cann J.R., 1973. Tectonic setting of basic volcanic rocks determined using trace element analyses. Earth and Planetary Science Letters, **19**, pp.290-300.

Pennington, W.D., 1983. Role of shallow phase changes in the subduction of oceanic crust. Science, **220**, pp.1045-1047.

Price, R.A., 1981. The Cordillera foreland thrust and fold belt in the southern Canadian Rocky Mountains. In Thrust and Nappe Tectonics. Edited by W.R. McClay and N.J. Price. Geological Society of London, Special Publication 9, pp.427-448.

Prior, D.B., and Coleman, J.M., 1982. Active slides and flows in underconsolidated marine sediments on the slopes of the Mississippi delta. In Marine slides and other mass movements. Edited by S. Saxon and J.K. Nieuwenhuis, Plenum Publications, New York, pp. 21-49.

Ramsey, J.G., 1967. Folding and Fracturing of Rocks. McGraw-Hill, New York, 568p.

Rice, J.R., 1975. On the stability of dilatant hardening for saturated rock masses. Journal of Geophysical Research, **80**, pp.1531-1536.

Richardson, A.M., and Whitman, R.v., 1963. Effect of strain-rate upon undrained shear resistance of a saturated remoulded fat clay. Geotechnique, **13**, pp.310-324.

Rieke, H.H. III, and Chilingarian, G.V., 1974. Compaction of argillaceous sediments. Elsevier Science Publication Company, New York, 424p.

Roddick, J.A., Muller, J.E., and Okulitch, A.V., 1979. Geologic map of Fraser River area, British Columbia-Washington. Geological Survey of Canada, Fraser River Sheet 92.

Roscoe, K.H., 1970. The influence of strains in soil mechanics. Tenth Rankine Lecture. Geotechnique, 20, pp.129-170.

Roscoe, K.H., 1971. Some soil mechanics concepts and the possibility of their wider application. In Structure, solid mechanics and engineering design, Volume 2. Edited by M. Te'eni. Wiley-Interscience, London pp.923-949.

Roscoe, K.H., Schofield, A.N., and Wroth, C.P., 1958. On the yielding of soils. Geotechnique, 8, pp.22-53.

Roscoe, K.H., Bassett, R.H., and Cole, E.R.L., 1967. Principle axes observed during simple shear of a sand. Proceedings on Shear Strength Properties of Natural Soils and Rocks, Oslo, 1, pp. 231-237.

Roscoe, K.H., and Burland, J.B., 1968. On the generalized stress-strain behavior of wet clay. In Engineering plasticity. Edited by J. Heyman, and F.A. Leckie. Cambridge University Press, London, pp.535-609.

Rudnicki, J.W., and Rice, J.R., 1975. Conditions for the localization of deformation in pressure-sensitive dilatant materials. Journal of the Mechanics and Physics of Solids, 23, pp.371-394.

Rupke, N.A., 1978. Deep clastic seas. In Sedimentary enviornments and facies. Edited by H.G. Reading. Elsevier Science Publication Company, New York, pp.372-415.

Rusmore, M.E., 1982. Structure and petrology of pre-Tertiary rocks near Port Renfrew, Vancouver Island, British Columbia. M.S. thesis, University of Washington, Seattle, WA, 124p.

Sangrey, D.A., Castro, G., Ponlos, S.J., and France, J.W., 1978. Cyclic loading of sands, silts and clays. In Earthquake engineering and soil dynamics, volume II. Proceedings of the American Society of Civil Engineers, Geotechnical Division, Special Conference, pp.836-851.

Schofield, A.N., and Wroth, C.P., 1968. Critical State Soil Mechanics. McGraw-Hill Publishing Company, New York, 310p.

Schwarz, H.U., 1982. Subaqueous slope failure-experiments and modern occurrences. In Contributions to sedimentology, volume 11. Elsevier Science Publication Company, New York, 116p.

Seed, H.B., 1968. Landslides during earthquakes due to soil liquefaction. Journal of the Soil Mechanics and Foundation Division, American Society of Civil Engineering , **94**, pp.1055-1122.

Seed, H.B., 1976. Evaluation of soil liquefaction effects on level ground during earthquakes. In Liquefaction problems in geotechnical engineering. American Society of Civil Engineering, Annual Convention and Exposition, Philadelphia, Preprint 2752, pp.1-104.

Seed, H.B., and Idriss, I.M., 1971. Simplified procedure for evaluating soil liquefaction potential. Journal of Soil Mechanics and Foundations Division, American Society of Civil Engineering, **97**, pp.1249-1273.

Seely, D.R., Vail, P.R., and Walton, G.G., 1974. Trench slope model In Geology of continental margins. Edited by C.A. Burk and C.L. Drake. Springer-Verlag, New York, pp.249-260.

Shouldice, D.H., 1971. Geology of the western Canadian continental shelf. Bulletin of Canadian Petroleum Geology, **19**, pp.405-436.

Silver, E.A., and Beutner, E.C., 1980. Penrose conference:melanges. Geology, **8**, pp.32-34.

Skempton, A.W., 1964. Long-term stability of clay slopes. Geotechnique, **14**, pp.77-101.

Skempton, A.W., 1970. The consolidation of clays by gravititional compaction. Quarterly Journal Geological Society of London, **125**, pp.373-411.

Smith, R.B., 1977. Formation of folds, boudinage, and mullions in non-newtonian materials. Geological Society of America Bulletin, **88**, pp.312-320.

Stein, S., Engeln, J.F., Wein, D.A., Fujita, K., and Speed, R.C., 1982. Subduction seismicity and tectonics in the Lesser Antilles Arc. Journal of Geophysical Research, **87**, pp.8642-8664.

Stevenson, A.J., Scholl, D.W., and Vallier, T.L., 1983. Tectonic and geologic implications of the Zodiac fan, Aleutian Abyssal Plain, northeast Pacific. Geological Society of America Bulletin, **94**, pp.259-273.

Stone, D.B., and Packer, D.R., 1979. Paleomagnetic data from the Alaska Peninsula. Geological Society of America, **90**, pp.545-560.

Sutherland Brown, A., 1968. Geology of the Queen Charlotte Islands, British Columbia. British Columbia Department of Mines and Petroleum Resources, Bulletin, **54**, 226p.

Thiede, J., and Dinkelman, M.G., 1977. Occurrence of **Inoceramus** remains in Late Mesozoic pelagic and hemipelagic sediments. In Initial reports of the deep sea drilling project, volume 39. Edited by P.R. Supko and K. Perch-Nielsen., et al.. Washington (U.S. Government Printing Office), pp.899-910.

Thompson, M., and Walsh, J.N., 1983. A handbook of inductively coupled plasma spectrometry. Blackie and Sons, Limited, London, 9p.

Torrance, J.K., 1983. Toward a general model of quick clay development. Sedimentology, **30**, pp.547-555.

Vance, J.A., 1968. Metamorphic aragonite in the prehnite-pumpellyite facies, northwest Washington. American Journal of Science, **266**, pp.299-315.

Vance, J.A., 1977. The stratigraphy and structure of Orcas Island, San Juan Islands. In Geology and water resources of the San Juan Islands. Edited by E.H. Brown, and R.C. Ellis. Washington Department Ecology Water Supply Bulletin, **46**, pp.3-16.

Vance, J.A., Dungan, M.A., Blanchard, D.P., and Rhodes, J.M., 1980. Tectonic setting and trace element geochemistry of Mesozoic ophiolitic rocks in western Washington. American Journal of Science, **280-A**, pp.359-388.

Von Huene, R., and Uyeda, S., 1981. A summary of results from the IPOD transects across the Japan, Mariana, and Middle-America convergent margins. Oceanologica Acta, Proceedings 26th International Geological Congress of Continental Margins Symposium, pp.223-239.

Von Huene, R., and Lee, H., 1983. The possible significance of pore fluid pressure in subduction zones. In Studies in continental margin geology. Edited by J.S. Watkins, and C.L. Drake. American Association of Petroleum Geologists Memoir 34, pp.781-791.

Walker, R.G., and Mutti, E., 1973. Turbidite facies and facies associations. In Turbidites and deep-water sedimentation. Edited by G.V. Middleton and A.H. Bouma. Society of Economic Paleontologists and Mineralogists, Pacific Section, pp.119-157.

Westbrook, G.K., Smith, M.J., Peacock, J.H., and Poulter, M.J., 1982. Extensive underthrusting of undeformed sediment beneath the accretionary complex of the Lesser Antilles subduction zone. Nature, **300**, pp.625-628

White, S.H., and Knipe R.J., 1978. Microstructures and cleavage development in selected slabes. Contributions to Mineralogy and Petrology, **66**, pp.165-174.

Wood, D.M., 1982. Laboratory investigations of the behavior of soils under cyclic loading: a review. In Soil mechanics--transient and cyclic loads. Edited by G.N. Pande and O.C. Zienkiewicz. John Wiley and Sons, New York, pp.513-582.

Woodcock, N.H., 1979. The use of slump structures as paleoslope orientation estimators. Sedimentology, **26**, pp.83-89.

Wroth, C.P., and Houlsby, G.T., 1981. A critical state model for predicting the behavior of clays. In Limit equilibrium, plasticity and generalized stress-strain in geotechnical engineering. Edited by R.K. Yong, and H.Y. Ko. American Society of Civil Engineering, pp.592-627.

Vesic, A.S., and Clough, G.W., 1968. Behavior of granular material under high stresses. Proceedings of the American Society of Civil Engineering, **94** SM3, pp.661-688.

APPENDIX A
FOSSILS FROM THE PACIFIC RIM COMPLEX

FOSSILS FROM THE UCLUTH VOLCANICS

Sample : 811016-1A and 811013-6 of Brandon (= GSC Locality C-102729 and C-102727 respectively)

Location Collected from limestone in the Ucluth Volcanics on the northwest side of the Ucluth Peninsula (the western conodont locality in Figure 3; 48°57'42"N, 125°36'03"W). The sample comes from a calcrudite consisting of clast-supported cobbles of gray limestone in a darker limestone matrix. Crinoid fragments are present in the cobbles and may also be in the matrix. The calcrudite is clearly interbedded with volcanic breccia and tuff.

Age M. Orchard (pers. comm., 1983) of the Canadian Geological Survey recovered conodonts from these samples which belong to biozones correlative to the Dawsoni-Magnus ammonoid zones representing the uppermost lower Norian -lowermost middle Norian.

Sample : 82922-5A of Brandon (= GSC Loc. C-102721)

Location Collected from a gray limestone bed in Ucluth Volcanics, located on the west side of Ucluth Peninsula (the eastern conodont locality in Figure 3; 48°57'03"N, 125°35'14"W). Limestone contains layers of black cherty sediment and green tuff; small ammonoids, and fragments of gastropods and of crinoids are also present. This limestone is clearly interbedded with the volcanic rocks and is also intruded by a small diorite dike.

Age The macrofossils were unidentifiable. M. Orchard (pers. comm., 1983) was able to recover conodonts from the samples which he identified as Karnian, probably upper Karnian.

FOSSILS FROM PILLOW LAVA AND CHERT UNITS

Sample : 82814-2A of Brandon

Location Collected from ribbon chert interbedded with pillow lava and tuff breccia, located at the north end of the beach at Ahous Bay, on the west side of Vargas Island (location marked in Figure 7).
Age Radiolaria were identified by E. A. Pessagno, Jr. (writ. comm., 1983) of the University of Texas at Dallas. His report is as follows:

Zone 01, upper half of Subzone 01B. Lower Jurassic: upper Toarcian

Zartus jurassicus Pessagno and Blome
Zartus dickinsoni Pessagno and Blome
Canoptum sp. (abundant)
Canoptum sp. aff. **C. anulatum** Pessagno and Poisson
Lupherium sp. cf. **L. officerense** Pessagno and Whalen
Napora sp.
Paronaella sp.
etc.

Sample : 72-27G of Muller (see Muller, et al., 1981)

Location Muller, et al. (1981) describe this locality as consisting of maroon-colored radiolarian chert, located on a point of land due west of the Food Islets on the southeast side of Ucluelet Inlet (corrected location = 48°55'07"N, 125°28'52"W). No mention is made of the surrounding rock types, but pillow basalt and mudstone-rich melange are known to crop out in this area.
Age Six samples were collected at this locality, designated VAI-1A through VAI-1F by Pessagno who processed and identified the radiolaria. His age identification with a composite list for all 6 samples is as follows (Muller, writ. comm., 1983):
Subzone 2A, probably lower part; Upper Jurassic: upper Kimmeridgian/lower Tithonian (confirmed by Pessagno, oral comm., 1983)

Eucrytidium (?) ptyctum Riedel and Sanfilippo
Praceonocaryomma mamillaria (Rust)
Praeconocaryomma magnimamma (Rust)
Hsuium maxwelli Pessagno
Hsuium cuestaensis Pessagno
Hsuium obispoensis Pessagno
Pantanellium riedeli Pessagno
Archaeodictyomitra rigida Pessagno
Parvacingula turrita (Rust)
Paronaella sp.

Spongocapsula palmerae Pessagno
Parvacingula sp.
Emiluvia sp.
Emiluvia salensis Pessagno
Cracella sanfilippoae Pessagno

Sample : 75-25A of Muller (unpublished data)
(=VAI-2A through VAI-2C of Pessagno)

Location Radiolarian chert collected on point of land at the southwest corner of Indian Reservation number 5, northwest of the Beg Islands, at the southeast side of Ucluelet Inlet (Muller, written communication, 1983). I have not located this specific outcrop although I know that pillow basalt and mudstone-rich melange are exposed in this area. Muller provided me with a general description from his field notes which mentions that mudstone and green tuff are closely associated with the chert but maybe in fault contact.
Age The following list and age identification are from Pessagno's unpublished report (Muller, writ. comm., 1983):

Zone 2 to Zone 4; upper Kimmeridgian/lower Tithonian to upper Tithonian (confirmed by Pessagno, oral communication, 1983).

VAI-2A and 2C
Poorly preserved; indeterminate
VAI-2B
Praeconocaryomma mamillaria (Rust)
Parvacingula sp.
Archaeodictyomitra rigida Pessagno

Sample : VAI-3 of Pessagno (Muller, unpublished data)

Location Collected by Muller and Pessagno from chert on the southwest side of Francis Island near the small battery-powered beacon (see Figure 3). This chert is closely associated with and is probably coeval with the pillow basalt exposed on this island.
Age The following list and age identification are from Pessagno's unpublished report (Muller, writ. comm., 1983):

Zone 1 to Zone 4: upper Kimmeridgian/lower Tithonian to upper Tithonian (confirmed by Pessagno, oral communication, 1983).

Hsuium maxwelli
Parvacingula turrita (Rust)
Parvacingula sp.
Emiluvia sp.

Archaeodictyomitra ridida Pessagno
Podobursa sp.
Pantanellium riedeli Pessagno
Spongocapsula palmerai Pessagno
Paranailla sp. (Fragment)
Parvacingula procera Pessagno?

FOSSILS FROM UNIT 1A

Sample : 82819-3A of Brandon

Location Collected from ribbon chert in Unit 1A at the south end of Wya point (location shown in Figure 3, second radiolarian locality from the north; also shown as the prominent lens of chert in Figure 9). Occurs as a well bedded, conformable lens of gray-green ribbon chert, about 30 cm thick, in a melange of disrupted black mudstone, chert and sandstone. The ribbon chert lens contains a thin sandstone interbed. It is clearly a native component of this melange.
Age The following report is from Pessagno (writ. comm., 1983):

Zone 5, Subzone 5C to Zone 6. Lower Cretaceous: upper Valanginian to upper Aptian.

Thanarla conica (Aliev)
Holocryptocanium sp. (abundant)
Archaeodictyomitra sp.

Sample : 82919-2A of Brandon

Location Collected from ribbon chert in Unit 1a at the central part of Wya Point (location shown in Figure 3, northern readiolarian locality). Occurs as a well bedded, conformable lens of ribbon chert, about 75 cm thick and 12 m long. Clearly interbedded with surrounding black mudstone of the melange.
Age The following report is from Pessagno (writ. comm., 1983):

Indeterminate. Abundance of **Holocryptocanium** suggests correlation to other samples cited above. (Lower Cretaceous(?)).

Holocryptocanium sp. (fragmental and abundant)

Sample : 82810-4A and -4B of Brandon

Location Collected from chert sequence on the south side of Blunden Island, west of Vargas Island (location marked in Figure 7). Sample -4B was collected about 1 meter above -4A in the same chert sequence. This ribbon chert is associated with disrupted mudstone and ribbon chert with minor volcanic blocks(?) and maybe equivalent to Unit 1A. Except for this outcrop, most of the Island is composed of massive sandstone belonging to Unit 2.
Age The following report is from Pessagno (writ. comm., 1983):

Zone 5, Subzone 5C to Zone 6. Lower Cretaceous: upper Valanginian to upper Aptian.

Thanarla conica (Aliev)
Holocryptocanium sp. (fragmental and abundant)
Cenosphaera sp.
Archaeodictyomitra sp.

FOSSILS FROM UNIT 1B

Sample : 821011-3A and -3B of Brandon

Location Collected from sandy ribbon chert sequence from Unit 1B, located south of Big Beach (the western radiolarian locality shown in Figure 13). The chert sequence depositional overlies black mudstone and is overlain by sandstone across a contact that is probably depositional. There is no local indication of stratigraphic tops; this sequence could very likely be overturned. The lowest meter of the chert sequence consists of sandy radiolarian ribbon chert.
Age Sample -3A was collected just above the basal contact; -3B was collected about 75 cm above the contact. The following report is from Pessagno (writ. comm., 1983):

Zone 5, subzone 5C. Lower Cretaceous: upper Valanginian to lower Hauterivian.

821011-3A

Thanarla conica (Aliev)
Archaeodictyomitra sp.
Ristola sp.
Holocryptocanium sp. (very abundant and fragmental)
Cenosphaera sp.

8281011-3B

Thanarla conica (Aliev)
Pseudodictyomitra sp.
Holocryptocanium sp. (abundant and fragmental)

Sample : 821011-1 of Brandon

Location Collected from ribbon chert in Unit 1B, south of Big Beach (the more eastern radiolaria locality shown in Figure 13). This locality is within 10 meters of 821011-3A and -3B, described above, and would be expected to be of the same age. The chert occurs as a small eroded block of sandy ribbon chert, about 30 m thick, surrounded by massive sandstone. One of the ribbon beds in the chert is actually a cherty sandstone.
Age The following report is from Pessagno (writ. comm., 1983):

Possibly Zone 4 to Zone 5, Subzone 5C. Upper Jurassic (upper Tithonian sensu Pessagno, Blome, and Longoria, in press) to Lower Cretaceous (upper Valanginian to lower Hauterivian).

Ristola sp. aff. **R. boesii** (Parona)
Acanthocircus dicranocanthos Squinabol?

Sample : 72-11A of Muller, et al. (1981) (=GSC Loc. C-89780)

Location Located at Big Beach on southwest coast of Ucluth Peninsula at end of foot trail on the beach (Figure 13) (corrected location = 48°56'00"N, 125°32'40"W).
Age In both locations **Buchia** shells occur in coquina-like beds of medium thickness within Unit 1B mudstone-rich melanges. Dr. J. A. Jeletzky identified these fossils as follows (from Muller, 1981,p 31-2):

"Mid-Valanginian stage, **Buchia pacifica** zone (Jeletzky, 1965, p.43-49). "The apparent absence of closed or gaping, complete (ie. double valved) shells could be interpreted as suggestive of re-deposition of fauna either by wave action or by turbidity currents" (Jeletzky's comments)".

Buchia pacifica Jeletzky 1965

Sample : 76-261 of Muller, et al. (1981) (=GSC locality C-89781)

Location Located on the north side of a bay, south of the Big Beach area on the southwest coast of the Ucluth Peninsula (0.75 km due south of Ucluelet, 48°56'00"N, 125°32'40"W).
Age Same as Sample 72-11A of Muller (1981) described above.

Sample : 821008-1 of Brandon (=GSC Locality C-102719)

Location Located close to the base of Unit 1B melange, north of Big Beach (the southeast **Buchia** locality shown in Figure 12) (48°56'11"N, 125°33'17"W). These **Buchia** also occur in a medium-bedded coquina, similar to Muller's **Buchia** localities described above (72-11A, 76-261).
Age Fossils were identified by Dr. J. A. Jeletzky (writ. comm., 1983) of the Geological Survey of Canada. The following is from his report (Km-7-1983-JAJ):

"Some part (more likely lower of **Buchia pacifica** Zone and of an early or (?)mid-Valanginian age in terms of the international standard stages (see Jeletzky, GSC Bull. 103, 1965, p.43-49, Figs. 1,2,4 and Jeletzky in Jeletzky and Tipper, GSC Paper 67-54, p.7-10, Table I for further details)."

Buchia pacifica Jeletzky, 1964 (prevalent)
Buchia tolmatschowi (Sokolov, 1908) (less common)
Buchia sp. indeterminant (Badly deformed representatives of two former species)

Sample : 821008-4 of Brandon (=GSC Locality C-102720)

Location Located at the base of Unit 1B mudstone-rich melange where it rests in depositional contact with the underlying Ucluth Volcanics ((the northwest **Buchia** locality shown in Figure 12) (48°56'11"N, 125°33'20"W). The **Buchia** do not occur in a coquina but are dispersed in a massive black mudstone containing minor concretions.
Age The following report is from Jeletzky (writ. comm., 1983 --report Km-7-1983-JAJ) who identified the fossils:

"Most likely the same as for the lot #C-102719. However, all the numerous Buchias of the lot #102720 are so badly deformed and sheared that the inferred prevalence of **B. pacifica** over **B. tomatschowi** may possibly be deceiving. Therefore, the lot #C-102720 could conceivably represent the upper part of the **Buchia tolmatschowi** Zone. In any case, the lot #C-102720 is correlative with the upper part of the One

Tree Formation of the Esperanza-Kyuquot area and is of an early to mid-Valanginian age in terms of the international standard stages (see Jeletzky, 1965, Bull. 103 for further details)."

Buchia pacifica Jeletzky, 1965 (apparently prevalent)
Buchia tolmatschowi (Sololov, 1908) (apparently less common).
Buchia cf. **uncitoides** (Pasvlow, 1970) sensu lato (apparently rare)

Sample : 82929-1 and 82927-4 of Brandon

Location Large bivalve shells (**Inoceramus**?) collected from Unit 1B at Big Beach. These samples come from two of the many localities shown in Figures 12 and 13. 82929-1 is located in the center of the map (Figure 13; near the attitude with a dip of 69°) and occurs in black mudstone interbedded with turbidite sandstone and conglomerate. 82927-4 is located at the north end of the map (Figure 13; near the attitude with a dip of 49°), and occurs in laminated mudstone.

At these localities and others in the area, the shells occur as thin calcite layers, everywhere oriented parallel to bedding, and locally with opposing valves of the shell still preserved. The shells are flat in cross-section, range from 25 to 150 cm long and 5 to 120 mm thick, and are composed of prismatic calcite grains oriented perpendicular to the shell edge. Weathered surfaces reveal a faint rhythmic banding superimposed on the prisms and oriented parallel to the length of the shell.

I sent these samples, with thin sections and field photographs, to Dr. E. G. Kauffman, an expert in Bivalve and Inoceramid paleontology at the University of Colorado. His report to me is as follows (Kauffman, pers. comm., 1983). He confirmed that they were indeed large bivalves. In thin section he observed organic material and growth bands preserved in the calcite. Kauffman showed the thin sections to Dr. R. Kligfield who has done extensive research on the development of veins in deformed rocks. Kligfield agreed that the shells represented organic structures and are not veins.

At this time Kauffman could not make a specific identification. He did say that based on similarities in size and morphology these bivavles probably occupied a similar paleoecological setting as did Cretaceous **Inoceramus.** He also mentioned that the individuals were adults, probably 10 to 30 years old. He agreed based on my photographs and descriptions that they were preserved in life position.

APPENDIX B
LIST OF SYMBOLS FOR PART II

d	= operator indicating differential increment
e	= void ratio
e_C	= void ratio of critical state line at $P'=1$ kPa
e_I	= void ratio of virgin isotropic consolidation line at $P'=1$ kPa
e_{Ko}	= void ratio of K_o consolidation line at $P'=1$ kPa
G	= elastic shear modulus
H'	= height of deformed duplex structure
K	= elastic swelling constant for K-line
K_o	= $\sigma_H'/\ \sigma_V'$ ratio during rest-state consolidation ($\varepsilon_H=0$)
L_o	= original length prior to deformation
L_f	= final length after deformation
L'	= deformed length of imbricated horizon
M	= slope of the critical state line in the P'-Q' diagram
n	= fractional porosity
N_{Ko}	= slope of P'-Q' stress path during Ko consolidation
P'	= effective pressure or effective mean stress
P_o'	= intersection of current yield surface with the P' axis
Q'	= $(\sigma_1'-\sigma_3')$; deviatoric stress during triaxial deformation
s'	= $(\sigma_V'-\sigma_H')/2$; mean normal stress during plane-strain deformation
S	= relative thrust displacement
t	= original thickness of imbricated horizon
t'	= $(\sigma_V'-\sigma_H')/2$; maximum shear stress during plane-strain deformation
U^*	= excess pore fluid pressure
U_p^*,U_q^*	= pressure-induced and deviatoric stress-induced components of excess pore pressure during undrained deformation
V	= volume

Δ = operator indicating finite increment

ε_s = $2(\varepsilon_1-\varepsilon_3)/3$; shear strain for triaxial deformation (positive during triaxial compression)

ε_v = volumetric strain (volume reduction is positive)

$\varepsilon_V,\varepsilon_H$ = vertical and horizontal strain components

$\varepsilon_1,\varepsilon_2,\varepsilon_3$ = principle strain components

= slope of critical state, isotropic and Ko consolidation lines in an e-Ln(P') diagram

$\emptyset$ = Mohr-Coulomb friction angle at the ultimate strength during triaxial compression

σ'_V, σ'_H = effective principle stresses for plane-strain deformation; σ'_V is the direction closest to vertical; σ'_H is the direction closest to horizontal

$\sigma'_1,\sigma'_2,\sigma'_3$ = effective principle stresses

Superscripts

' = indicates effective stress when used with stress variables (stress variables are effective unless otherwise noted)

p = indicates plastic strain component

e = indicates elastic strain component

t = indicates total strain component

VITA

Mark Thomas Brandon

Birthdate: 29 October 1953. Birthplace: Los Angeles, California

Parents: Earl Thomas Brandon and Shirley Jean Brandon

Graduated from Ravenswood High School, 1970

B.S., University of California, Santa Cruz, 1975

M.S., University of Washington, 1980